

# SYMMETRIES AND TRANSITIONS IN COLLECTIVE MOTION OF ACTIVE MATTER

BENJAMIN HALAGER ANDERSEN



This thesis has been submitted to the PhD School of The Faculty of Science, University of Copenhagen. In partial fulfillment of the requirements for the degree of

*Doctor of Philosophy*

Supervised by Amin Doostmohammadi

NIELS BOHR INSTITUTE  
UNIVERSITY OF COPENHAGEN

May 28, 2024





UNIVERSITY OF  
COPENHAGEN

TITLE: Symmetries and transitions in Collective  
Motion of Active Matter

AUTHOR: Benjamin Halager Andersen  
EMAIL: benjamin.andersen@nbi.ku.dk

SUPERVISOR: Assoc. Prof. Amin Doostmohammadi  
EMAIL: doostmohammadi@nbi.ku.dk

INSTITUTE: Niels Bohr Institute  
UNIVERSITY: University of Copenhagen

SUBMITTED: May 28, 2024  
DEFENDED: June 21, 2024

NAME \_\_\_\_\_

SIGNATURE \_\_\_\_\_

DATE \_\_\_\_\_



# Abstract

**Part I:** This research explores the dynamics of polar active particles under varying active stresses, revealing distinct flow fields and self-organizing patterns. A crossover from defect-free to defect-laden active turbulence with increasing stress is observed, leading to the restoration of  $SO(2)$  symmetry, indicated by the rapid decay of the two-point correlation function in the polar field. The mechanism of defect pair nucleation is examined, and conducting a stability analysis of the diffusive charge density provides additional insights into the onset of active turbulence laden with topological defects.

**Part II:** This work examines active turbulence, focusing on the dynamic behavior of topological defects in active nematic fluids. An information-theoretic divergence measure is utilized, which does not require any prior knowledge of the system, to quantify spatiotemporal order. By extracting defect positions and analyzing their dynamics, two key transitions are identified: the onset of defect nucleation and a subsequent hidden spatiotemporal transition marking fully-developed active turbulence, characterized by the optimal spatial and temporal organization of these defects.

**Part III:** This study unveils a universal feature in the flow patterns of collectively moving cells across diverse biological systems. Experimental evidence demonstrates robust conformal invariance in flows generated by dog kidney cells, human breast cancer cells, and two strains of pathogenic bacteria. Remarkably, these systems exhibit consistent adherence to the Schramm-Loewner Evolution (SLE) and percolation universality class. A continuum model of active matter reproduces the observed conformal invariance and SLE behavior. These findings suggest that living biological matter possesses universal translational, rotational, and scale symmetries, independent of the microscopic properties. The study highlights the conservation of flow patterns among diverse cellular systems, offering unexpected opportunities to test theories for conformally invariant structures in biological contexts.



# Resumé

**Part I:** Denne forskning udforsker dynamikken af polære aktive partikler under varierende aktiv mekanisk belastning, hvilket afslører særskilte strømningsfelter og selvorganiserende mønstre. En overgang fra defekt-fri til defekt-mættet aktiv turbulens ved stigende mekanisk belastning er observeret, hvilket fører til genoprettelsen af  $SO(2)$ -symmetrien, hvilket er indikeret ved den hurtige aftagen af to-punkts korrelationsfunktionen i det polære felt. Mekanismen for defekt par nukleation undersøges, og gennemførelse af en stabilitetsanalyse af den diffusive ladningstæthed giver yderligere indblik i ophavet til aktiv turbulens mættet med topologiske defekter.

**Part II:** Dette arbejde undersøger aktiv turbulens med fokus på den dynamiske adfærd af topologiske defekter i aktive nematiske væsker. Et informationsteoretisk divergensmål anvendes, som ikke kræver nogen forudgående viden om systemet, til at kvantificere spatiotemporal orden. Ved at udtrække defektpositioner og analysere deres dynamik identificeres to centrale overgange: begyndelsen af defekt nukleering og en efterfølgende skjult spatiotemporal overgang, der markerer fuldt udviklet aktiv turbulens, karakteriseret ved den optimale rumlige og tidsmæssige organisering af disse defekter.

**Part III:** Dette studie afdækker en universel egenskab ved strømningsmønstrene for kollektivt bevægende celler på tværs af forskellige biologiske systemer. Eksperimentelle vidnesbyrd viser robust konform invarians i strømninger genereret af hundenyreceller, menneskelige brystkræftceller og to stammer af patogene bakterier. Bemærkelsesværdigt nok udviser disse systemer en konsekvent overholdelse af Schramm-Loewner Evolution (SLE) og perkolation universalitet klassen. En kontinuumsmodel for aktivt stof gengiver den observeret konform invarians og SLE-adfærd. Disse resultater tyder på, at levende biologisk stof besidder universelle translations-, rotations- og skalasymmetrier, uafhængigt af de mikroskopiske egenskaber. Studiet fremhæver bevarelsen af strømningsmønstre blandt forskellige cellulære systemer, hvilket giver uventede muligheder for at teste teorier for konformt invariante strukturer i biologiske sammenhænge.





# Acknowledgements

I would like to express my sincere gratitude to Amin Doostmohammadi, my supervisor, for his unwavering support, invaluable guidance, and endless patience throughout this journey. His expertise, encouragement, and insightful feedback have been instrumental in shaping this thesis.

I am grateful to the Niels Bohr International Academy and the Biocomplexity group for providing the resources, facilities, and conducive environment necessary for carrying out this research.

I extend my heartfelt appreciation to my colleagues and friends for their encouragement, support, and understanding during the ups and downs of the doctoral journey. Their camaraderie and shared experiences have made this challenging endeavor much more manageable.

Special thanks are due to my family for their unwavering love, encouragement, and belief in my abilities. Their patience, understanding, and sacrifices have been the cornerstone of my success.

Lastly, I would like to express my gratitude to all my collaborators, co-authors, and organizations who generously contributed their time, expertise, and resources to this research project.

This thesis would not have been possible without the support and encouragement of all those mentioned above. Thank you from the bottom of my heart.



# Publications

Authored publications contributing to this thesis, in order of appearance.

1. Benjamin H. Andersen, Julian Renaud, Jonas Rønning, Luiza Angheluta, and Amin Doostmohammadi. *Symmetry-restoring crossover from defect-free to defect-laden turbulence in polar active matter*. Phys. Rev. Fluids **8**, 063101 (2023).
2. Robin V. Bølsterli<sup>†</sup>, Benjamin H. Andersen<sup>†</sup>, and Amin Doostmohammadi. *Fully developed active turbulence: Emergence of hidden spatiotemporal transition in active nematic fluids*, arXiv (2024).
3. Benjamin H. Andersen<sup>‡</sup>, Francisco M. R. Safara<sup>‡</sup>, Valeriia Grudtsyna, Oliver J. Meacock, Simon G. Andersen, William M. Durham, Nuno A. M. Araujo, and Amin Doostmohammadi. *Evidence of robust, universal conformal invariance in biological matter*, arXiv (2024).

---

<sup>†</sup>These authors contributed equally to this work.

<sup>‡</sup>These authors contributed equally to this work.



# Contents

|          |   |           |
|----------|---|-----------|
| <b>1</b> | <b>Introduction and objectives</b>  | <b>1</b>  |
| <b>2</b> | <b>Symmetry-restoring crossover in polar active fluids</b>  | <b>3</b>  |
| 2.1      | Continuum model for active polar fluids . . . . .   | 3         |
| 2.2      | Results . . . . .   | 6         |
| 2.3      | Conclusion . . . . .  | 14        |
|          | Bibliography . . . . .  | 15        |
|          | Manuscript: Symmetry-restoring crossover from defect-free to defect-laden turbulence in polar active matter . . . . .           | 17        |
| <b>3</b> | <b>Spatiotemporal transition in active nematic fluids</b>   | <b>33</b> |
| 3.1      | Nematohydrodynamic model . . . . .  | 33        |
| 3.2      | Spatiotemporal defect disorder . . . . .  | 35        |
| 3.3      | Results . . . . .   | 38        |
| 3.4      | Conclusion . . . . .  | 41        |
|          | Bibliography . . . . .  | 43        |
|          | Manuscript: Fully developed active turbulence: Emergence of hidden spatiotemporal transition in active nematic fluids . . . . . | 46        |
| <b>4</b> | <b>Conformal invariance in biological matter</b>  | <b>53</b> |
| 4.1      | Methods . . . . .   | 54        |
| 4.2      | Cluster geometry and scale invariance . . . . .   | 55        |
| 4.3      | Vorticity contours and conformal invariance . . . . .   | 57        |
| 4.4      | Conclusion . . . . .  | 62        |
|          | Bibliography . . . . .  | 64        |
|          | Manuscript: Evidence of robust, universal conformal invariance in living biological matter . . . . .                            | 66        |
|          | <b>Appendices</b>   | <b>79</b> |
| <b>A</b> | <b>The Dirac <math>\delta</math>-distribution of a composite argument</b>   | <b>81</b> |



# Chapter 1

## Introduction and objectives

This thesis is organized into three discrete sections, not due to their complete independence, but rather to enhance clarity by presenting each part as a self-contained narrative. Adopting a synopsis style, the thesis offers a moderate level of detail on the subjects addressed, while acknowledging that more comprehensive explanations are accessible in the accompanying published manuscripts. Notably, many of the figures and method descriptions presented in this thesis are reproductions from these manuscripts, conveniently included at the end of each respective chapter.

Although separate, the three projects revolve around a common theme: transitions and symmetries in active systems. These projects include both continuum simulations and experimental data involving monolayers of eukaryotic and prokaryotic cells.

**Part I** concerns research done on a continuum description of a two-dimensional active polar fluid in the context of flow characteristics and topological defect dynamics – singular points in the polarity field where order breaks down. Many living organisms, on length scales ranging from bacterial suspensions up to animal herds, exhibit polar order at the level of individual agents. This local polarity facilitates spatial symmetry breaking on global scales, in addition to sustaining a form of chaotic flows at low Reynolds numbers known as active turbulence. Making the study of active polar matter crucial for understanding the underlying principles of life-like processes and the development of novel materials.

**Part II** concerns research done on a continuum description of a two-dimensional active nematic fluid, another type of active fluid characterized by the presence of half-integer topological defects and the sustained active turbulent state. The motion of these topological defects is intricately connected with the formation of flow patterns, including the arrangement of vortices and jets. The objective of this research is to expand upon an information-theoretic approach to infer insights

regarding the spatiotemporal ordering of these topological defects.

**Part III** explores the conformal symmetries and universalities exhibited by spontaneously generated vortical flow structures at large scales within high-resolution measurements of monolayers composed of four distinct cellular genotypes, spanning both prokaryotes and eukaryotes. For prokaryotes, the investigation includes both the wild type *Pseudomonas aeruginosa* pathogen alongside its hyperpilated deletion mutant  $\Delta pilH$ . In the realm of eukaryotes, the study encompasses the extensively researched Madin-Darby Canine Kidney (MDCK) cells, as well as the formidable human breast cancer cell line MCF-7. The analysis grounded in the theory of Schramm-Loewner evolution (SLE) processes and involves the identification of zero-vorticity isolines as putative SLE processes.



# Chapter 2

## Symmetry-restoring crossover in polar active fluids

Active polar fluids are fascinating because they comprise self-propelled particles that exhibit complex collective behaviors, significantly different from those seen in passive systems. These behaviors include spontaneous flow generation [1, 2], with associated nonequilibrium steady states [3, 4], and turbulence at low Reynolds numbers, driven by the continuous input of energy at the scale of individual constituents. This study is solely grounded in [5] and its novelty lies in its exploration of the crossover from defect-free to defect-laden turbulence in polar active fluids, an area that has been relatively underexplored. Previous research has primarily focused on active nematics [6–8], which lack polarity and self-propulsion, leaving a gap in understanding the role of topological defects in polar active systems. By combining numerical simulations with theoretical analysis, this study provides new insights into the criteria for the emergence of defect-laden turbulence and its impact on global symmetry and spatiotemporal organization, thereby contributing to the broader field of active matter physics.

### 2.1 Continuum model for active polar fluids

A two-dimensional incompressible active polar fluid is examined, characterized by a local orientational order represented by a two-component order parameter  $p_i$  aligned with the direction of self-propulsion. It is noteworthy that we do not treat the polarity as a fixed unit vector with a constant magnitude. Instead, the magnitude of polarity is considered a significant dynamic variable within this formulation. The fluid's velocity and density are denoted by  $u_i$  and  $\rho$ , respectively. Hydrodynamic equations on a coarse-grained level can be derived through phe-

nomenological reasoning [9–11] and are expressed as follows:

$$\rho(\partial_t + u_j \partial_j)u_i = \partial_j \Pi_{ij}, \quad (2.1)$$

$$(\partial_t + u_k \partial_k)p_i - (\lambda E_{ij} + \Omega_{ij}) = \frac{1}{\gamma} h_i. \quad (2.2)$$

along with the incompressibility condition  $\partial_i u_i = 0$ . The strain rate tensor  $E_{ij} = (\partial_i u_j + \partial_j u_i)/2$  and the vorticity tensor  $\Omega_{ij} = (\partial_i u_j - \partial_j u_i)/2$  represent the symmetric and antisymmetric parts, respectively, of the velocity gradient tensor. The stress tensor  $\Pi_{ij}$  in the momentum balance equation (2.1) comprises three parts; viscous stress  $\Pi_{ij}^{\text{viscous}} = 2\mu E_{ij}$ , passive stress

$$\Pi_{ij}^{\text{passive}} = -P\delta_{ij} + \left( \frac{\lambda+1}{2} \delta_{ik} \delta_{jl} - \frac{\lambda}{2} \delta_{ij} \delta_{kl} + \frac{\lambda-1}{2} \delta_{il} \delta_{jk} \right) p_k h_l, \quad (2.3)$$

and active stress  $\Pi_{ij}^{\text{active}} = -\zeta (p_i p_j - \frac{1}{2} p^2 \delta_{ij})$ . The first term in the passive stress (2.3) is the familiar hydrodynamic pressure and the second term accounts for anisotropic elastic stresses. The alignment parameter  $\lambda$  determines whether strain or vorticity dominates the polar constituents collective response to shear flow. The molecular field  $h_i = -\delta F / \delta p_i$  ensures diffuse relaxation of the polar order to the minimum of the free energy

$$F = \int \left\{ \mathcal{A} \left( -\frac{p^2}{2} + \frac{p^4}{4} \right) + \frac{K}{2} (\partial_i p_j)^2 \right\} d^2 \mathbf{x} \quad (2.4)$$

on a timescale set by the rotational diffusive constant  $\gamma$ . The free energy consists of a local energy density, governed by an energy scale  $\mathcal{A}$ , which regulates the isotropic-polar transition favoring the emergence of finite polarity at  $p = 1$ , and a nonlocal energy contribution with an elastic constant  $K$  that penalizes deformations in the polarity field.

### 2.1.1 Simulations and parameters

The governing equations (2.1-2) are numerically integrated using a hybrid lattice-Boltzmann method. This approach combines the finite-difference method for the evolution of the polarity vector (2.2) and the lattice-Boltzmann method for solving the incompressible Navier-Stokes equations (2.1). Simulations were initialized with quiescent velocity field and slightly perturbed polar alignments close to the uniformly oriented state with polarity aligned along the  $x$ -axis. The system is evolved on a periodic quadratic domain of linear dimension  $L = 1024$  until a statistical steady state is reached. The lattice spacing and time step are set to unity, and density  $\rho = 40$  and viscosity  $\mu = 3.6$  are chosen to ensure a negligible Reynolds

number ( $\text{Re} \ll 1$ ) in the simulations. The remaining four dimensionless variables characterizing the system are the dimensionless ratio of the viscosities  $\mu/\gamma = 3.6$ , the flow alignment parameter  $\lambda = 0.1$ , the dimensionless active stress  $\bar{\zeta} = \zeta/\mathcal{A}$ , and the ratio of micro to macro length scales  $l_p/L = 0.0002$ , ensuring that the coherence length  $l_p = \sqrt{K/\mathcal{A}}$  is significantly smaller than the domain size  $L$ . These values are fixed unless otherwise stated.

### 2.1.2 Defect charge density

Topological defects are singular points in the polarity field  $p_i$  where the order breaks down and around which the orientation field winds by an integer multiple of  $2\pi$  [9, 12, 13]. Only energetically stable defects of charge  $\pm 1$  are examined hereafter. Defects of higher charge, although topologically stable in two-dimensions, are energetically unstable and tend to dissociate into elementary defects, as their intrinsic energy increases with the square of the charge [14]. The Halperin-Mazenko method [15–17] begins by recognizing that defect dynamics are identified with the movement of zeros in the polarity field, with the topological charge distribution represented according to:

$$\rho(t, \mathbf{x}) = \sum_k q_k \delta(\mathbf{x} - \mathbf{x}_k(t)), \quad (2.5)$$

where  $\mathbf{x}_k$  and  $q_k$  denotes the position and charge of the respective defect. Suppose, the defect charge distribution is described in terms of the zeros of the polarity field rather than the positions of defects  $x_k$ . The result of which being:

$$\rho(t, \mathbf{x}) = (\delta \circ \mathbf{p})(t, \mathbf{x}) D(t, \mathbf{x}), \quad (2.6)$$

where the defect charge density  $D = \det(\nabla \mathbf{p})$  is the Jacobian determinant associated with transformation from the physical space to the order-parameter space (appendix A). The consequences being that  $D$  is a smooth scalar field, vanishing everywhere except at the singular points of the transformation – localized regions centered the core of topological defects where the order breaks down. The dynamical implications of this transformation are simple. The defect charge density obey the continuity equation (A.14)

$$\partial_t D = \partial_i J_i, \quad (2.7)$$

with current density given by (A.15)

$$J_i = \epsilon_{ij} \epsilon_{mnp} \partial_t p_m \partial_j p_n. \quad (2.8)$$

Merely reflecting the fact that topological charges are conserved necessitates that the topological charge density (2.6) adheres to a continuity equation.

## 2.2 Results

The polar order parameter belongs to the  $SO(2)$  group of symmetries and carries full integer defects. It is globally characterized by the unsigned topological defect density  $\rho_d$ . As shown in figure 2.1C, increasing activity beyond a certain threshold leads to a continuous rise in defect density in both extensile ( $\zeta > 0$ ) and contractile ( $\zeta < 0$ ) systems. Verification was conducted to ensure that these activity thresholds are independent of system size  $L$ , with simulations across various domain sizes ( $512 \times 512$ ,  $1024 \times 1024$ , and  $4096 \times 4096$ ) demonstrating the same quantitative relationship between defect density and activity.

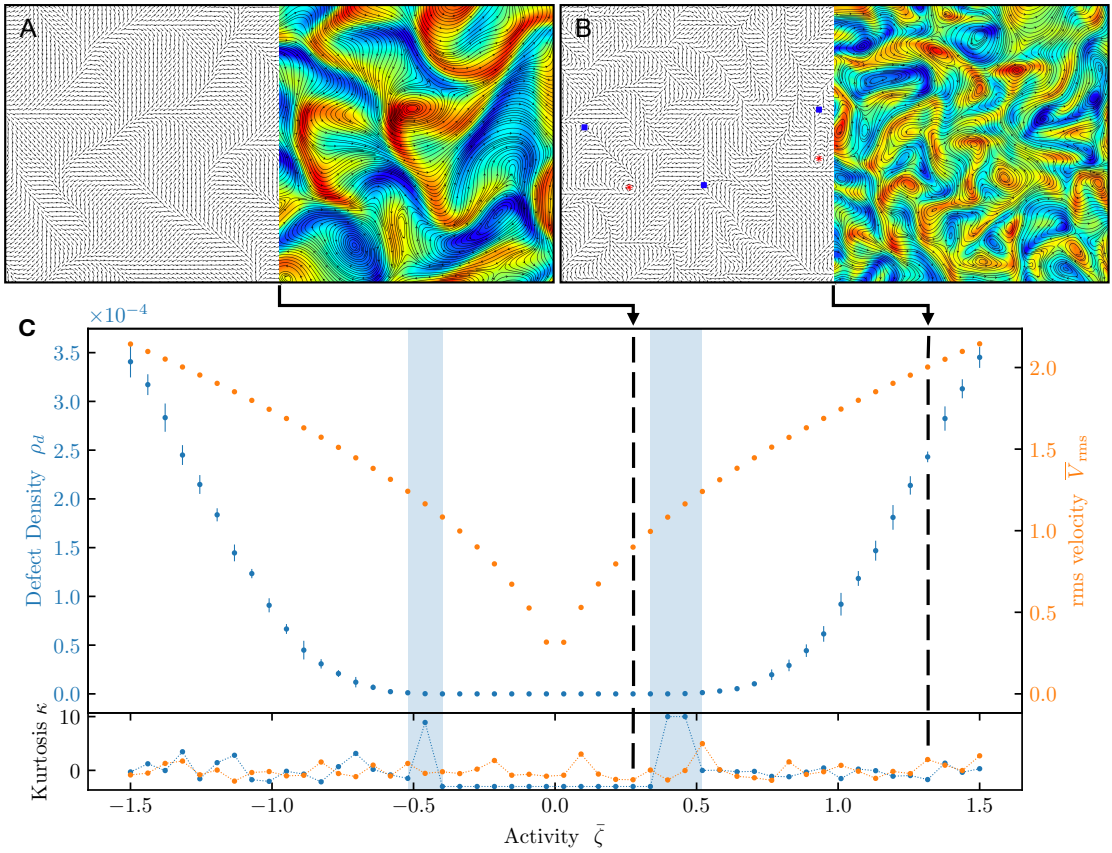


Figure 2.1: (A-B) Snapshots depicting the polarity field (left panel) and its associated vorticity field (right panel), alongside streamlines, captured within a cropped portion of the complete domain. Topological defects are denoted by red stars (+1 defect) and blue squares (-1 defect). (C) Variation of defect density and rms velocity with activity levels. Highlighted in blue are regions signifying peaks in the excess kurtosis (bottom panel), indicating the activity threshold.

The flow field is globally characterized by the root-mean-square (rms) velocity  $\overline{V}_{\text{rms}} = V_{\text{rms}}/V_p$ , measured relative to the passive relaxation velocity of the polar particles  $V_p = \sqrt{\mathcal{A}K/\mu}$ . Interestingly, rms velocity measurements show that active stresses disturb the polarity field and generate spontaneous flows within the system, even below the activity threshold for defect nucleation, for any nonzero activity. At higher activities, these flows become laden with full-integer topological defects. Thus, there is a well-defined activity threshold marking the crossover from defect-free to defect-laden active turbulence. This transition is evident from the averaged defect density and rms velocity, showing that topological defects form and persist only beyond a finite threshold, with different excess kurtosis values indicating the nature of the crossover.

At elevated activity levels, the excess kurtosis in defect density tends to diminish, suggesting a near-equilibrium state where defect population follow a Gaussian distribution. Conversely, under low activity levels, defects are absent, and conventionally, the excess kurtosis is assigned a value of  $-3$ . The transition between these states is marked by rare occurrences of defect formation and annihilation, evident from peaks in the surplus kurtosis, highlighted in blue in figure 2.1C. Interestingly, no such peaks are observed for the surplus kurtosis of the rms velocity, indicating the absence of an equivalent crossover regime.

This observation aligns with qualitative findings from examining the velocity field below the threshold for defect nucleation in the system. Here, chaotic flows prevail, characterized by the presence of flow vortices and jets traversing the system (Fig. 2.1A). Remarkably, despite the chaotic nature of these flows, no topological defects are discernible in the polarity field. As activity levels increase, qualitatively similar chaotic flows persist, albeit with a reduction in the characteristic length scale, as dictated by the active length scale  $L_{\text{act}} = \sqrt{K/|\zeta|}$ . However, a significant transformation occurs: the chaotic flows become populated with full-integer topological defects, notably unbound vortex and antivortex pairs, prominently visible in the polarity field (Fig. 2.1B).

### 2.2.1 Recovery of SO(2) symmetry

Examining the global polarization (Fig. 2.2 orange markers), defined here as the spatiotemporal average of the polarity field

$$\Psi = \int \frac{dt}{T} \int \frac{d^2\mathbf{x}}{L^2} \mathbf{P}(t, \mathbf{x}), \quad (2.9)$$

to probe the crossover between the two active turbulence regimes. As the active stress increases from zero, the active turbulence state immediately displays broken SO(2) symmetry, as evidenced by a nonzero value of  $|\Psi|$  in the absence of topological defects. The global polarization decreases in magnitude with increasing

activity, and notably, it drops to zero beyond a critical activity level necessary for the nucleation of topological defects. This behavior indicates the recovery of  $SO(2)$  symmetry in the defect-laden turbulent state.

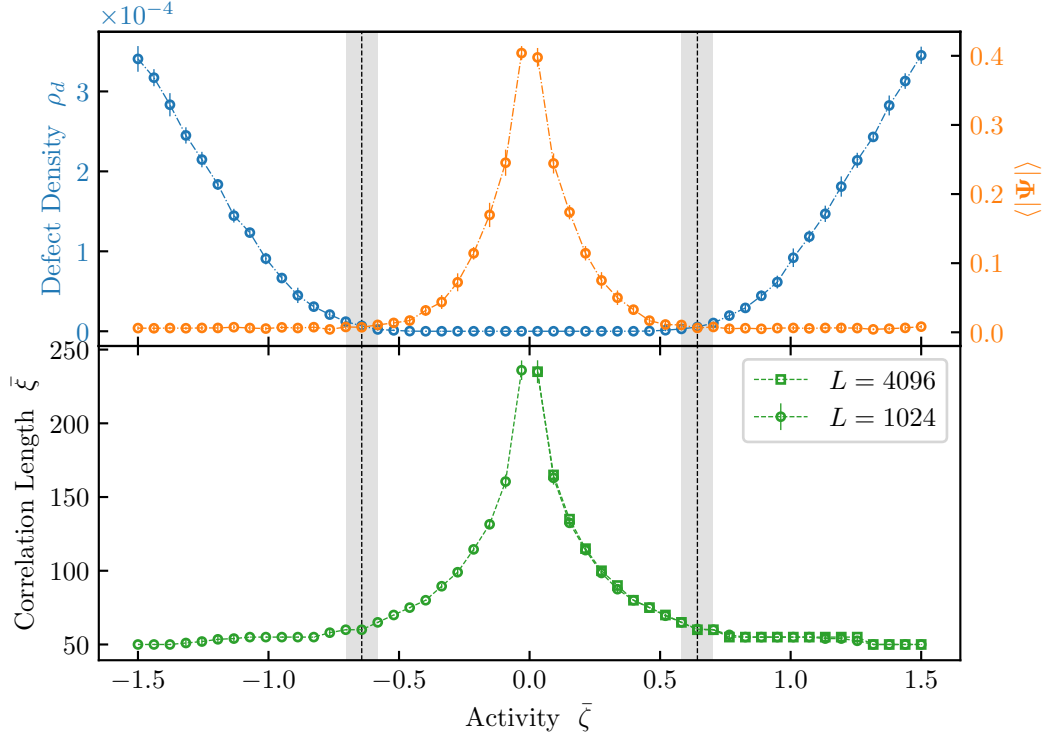


Figure 2.2: Top panel displays defect density (blue markers) and magnitude of the polarization  $\Psi$  (orange markers), averaged over independent system realizations. Bottom panel shows the correlation length (measured in units of the coherence length  $l_p$ ) derived from the equal-time, spatial pair-correlation function for fluctuations in the polarity field (Fig. 2.3).

To further characterize the crossover, the equal-time spatial pair-correlation function for the polarity field  $\Gamma(\mathbf{r}) = \langle \delta p_i(\mathbf{x}) \delta p_i(\mathbf{x} + \mathbf{r}) \rangle$  is measured (Fig. 2.3). Here,  $\delta p_i(\mathbf{x}) = p_i(\mathbf{x}) - \langle p_i(\mathbf{x}) \rangle$  represents the deviation from the local mean value. Averaging is performed over ten independent realizations, with distinct initial conditions and over time, once the system has reached a statistical steady state. The correlation length  $\xi$  is derived by fitting an exponential to the pair-correlation function. Normalized with respect to the coherence length  $l_p$ , the correlation length  $\bar{\xi} = \xi/l_p$  decreases with increasing activity (Fig. 2.2). Correlation measurements were verified to be independent of domain size for large systems up to  $4096 \times 4096$ . The behavior of the correlation length parallels that observed in frustrated two-dimensional Heisenberg magnets, showing a crossover from a defect-dominated

regime at high temperatures to a spin-wave regime at low temperatures. These findings indicate that the transition from defect-free to defect-laden active turbulence significantly affects both global symmetry and local polarity correlations in active matter systems. Lastly, it is important to note that no differences are observed between longitudinal and transverse correlations in the polarity field. The correlation length does not diverge with system size within the ordered state. This behavior is likely due to the nonequilibrium nature of the system and the breaking of detailed balance [18] through activity-induced flows that interact with the dynamics of the order parameter.

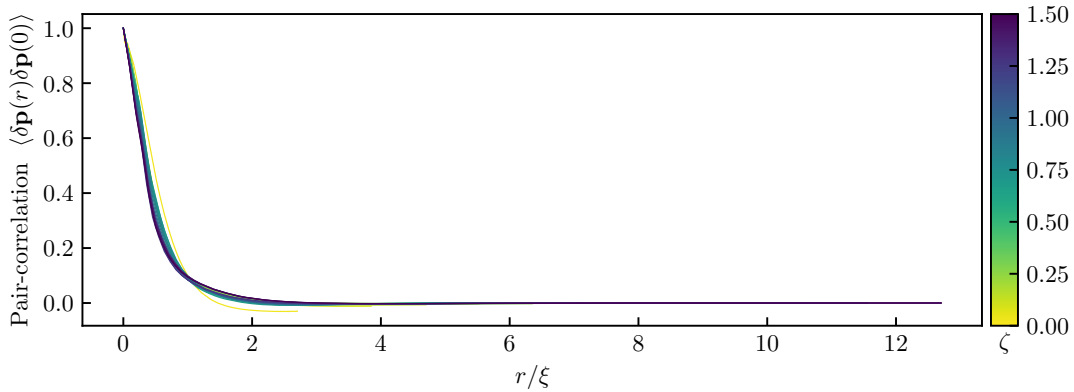


Figure 2.3: The equal-time, spatial pair-correlation function for fluctuations in the polarity field  $\Gamma(\mathbf{r}) = \langle \delta p_i(\mathbf{x}) \delta p_i(\mathbf{x} + \mathbf{r}) \rangle$  as function of the radial distance scaled by correlation length.

### 2.2.2 Defect pair nucleation mechanism

In figure 2.4, snapshots capture the polarity field moments before, during, and after a single pair of defects forms under both contractile (Fig. 2.4C) and extensile (Fig. 2.4D) stresses. The onset of nucleation coincides with a surge in bulk free-energy (Fig. 2.4A-B), indicating polarity flipping within kink walls overcoming energy barriers. Once formed, the defect pair's presence reduces bulk free-energy. The normalized diffuse charge density helps pinpoint and track topological defects. Negatively charged antivortices exhibit similar structures in both systems, while positively charged defects take on distinct forms, as predicted analytically. This insight into defect nucleation mechanisms informs our understanding of the activity threshold, highlighting the interplay between bulk and elastic energies and activity-induced flows.

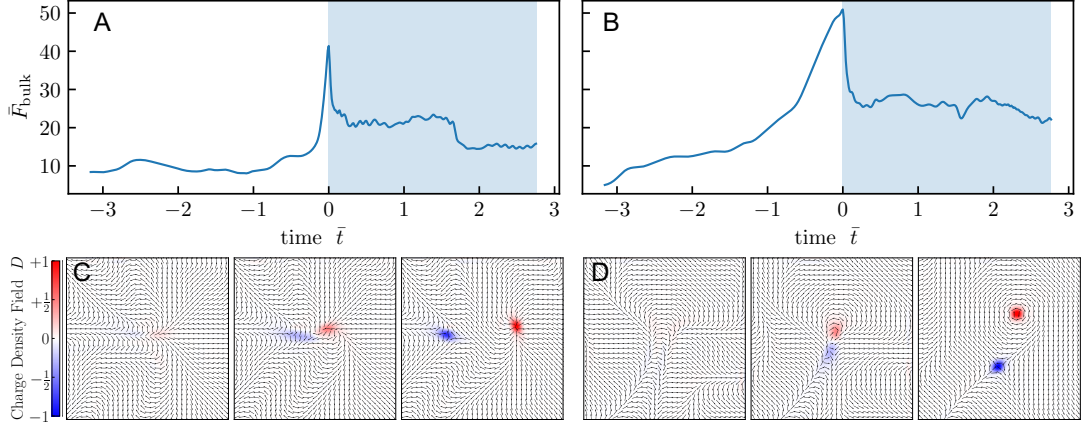


Figure 2.4: (A-B) The temporal evolution of the average bulk free-energy  $\bar{F}_{\text{bulk}} = (F_{\text{bulk}} + \mathcal{A}/4) / \mathcal{A}L_{\text{act}}$  measured in units of  $\mathcal{A}L_{\text{act}}$  relative to the background field  $-\mathcal{A}/4$ . (C-D) Simulation snapshots illustrating the polarity field and diffuse charge density before, during, and after the nucleation of a single pair of oppositely charged topological defects. Panels (A) and (C) depict a contractile ( $\zeta < 0$ ) system, while panels (B) and (D) represent a extensile ( $\zeta > 0$ ) system.

### 2.2.3 Onset of defect-laden active turbulence

To gain further insights into the onset of defect pair nucleation, a stability analysis of the topological charge density field is performed. To achieve this,

- (i) fluid inertia is neglected, as it is insignificant in the viscous limit that becomes relevant on the length scales of bacterial suspension.
- (ii) backflow generated by elastic stress is neglected, as it is orders of magnitude smaller than the flow due to active stress in our simulations.
- (iii) any pressure gradient is also neglected.

As a result, the governing equation for the flow field (2.1) simplifies to an approximate local relation that balances the viscous stress with the active stress

$$2\mu E_{ij} \approx \zeta \left( p_i p_j - \frac{1}{2} p^2 \delta_{ij} \right). \quad (2.10)$$

Due to viscosity and incompressibility constraints, the effects of advection and rotation of the polar field caused by flow velocity and vorticity are nonlocal. Consequently, these effects cannot be reduced to linear operators acting on solely on the defect charge density  $D$ . Therefore, when considering only the contribution



from shear flow alignment and the molecular field, the governing equation for the polar field (2.2) becomes

$$\partial_t p_i - \lambda E_{ij} = \frac{1}{\gamma} [\mathcal{A} (1 - p^2) p_i + K \Delta p_i]. \quad (2.11)$$

In light of these approximations, the continuity equation for the topological charge density (2.7) is given by reaction-diffusion equation:

$$\partial_t D \approx \frac{K}{\gamma} \Delta D + \left( \frac{2\mathcal{A}}{\gamma} (1 - 2p^2) + \frac{\zeta \lambda}{\mu} p^2 \right) D, \quad (2.12)$$

where the ratio of the elastic constant  $K$  to its relaxation timescale  $\gamma$  determines an effective diffusivity coefficient and thereby setting the scale of the diffusive core. The crossover activity threshold is estimated from a linear stability analysis of (2.12) about the ordered state, by considering perturbations of the form  $p = 1 + \delta p$  and  $D = \delta D$ . This leads to balancing the two contributions to the reaction term, revealing that defect charge density remains stable for

$$\zeta \lesssim \frac{2\mu}{\gamma \lambda} \mathcal{A}, \quad (2.13)$$

assuming that the flow alignment parameter  $\lambda$  is positive. Interestingly, this suggests that the topological charge density becomes unstable to defect nucleation only for extensile systems ( $\zeta > 0$ ). However, by neglecting the effects of advection and rotation of the polar field in (2.11), the contributions of flow velocity and vorticity as destabilizing forces that induce instabilities in the defect charge density field are also neglected. Nonetheless, the contribution of vorticity to the evolution of  $D$  is symmetric with respect to the sign of active stress  $\zeta$ . Consequently, any instability induced by vorticity would occur at a critical activity for both extensile and contractile systems, also exhibiting symmetry with respect to the sign of  $\zeta$ .

The estimated threshold activity (2.13) is solely derived from the effects of flow alignment, with all other destabilizing forces neglected. Therefore, the threshold activity observed in simulations is not expected to be in quantitative agreement with the estimated prediction (2.13). Nonetheless, the stability analysis above provides valuable insights and predicts qualitative properties of the threshold activity:

- (i) It depends on the energy scale  $\mathcal{A}$  controlling polar order, in the vicinity of the threshold activity.
- (ii) It is asymmetric with respect to the sign of the active stress, in the presence of flow alignment.

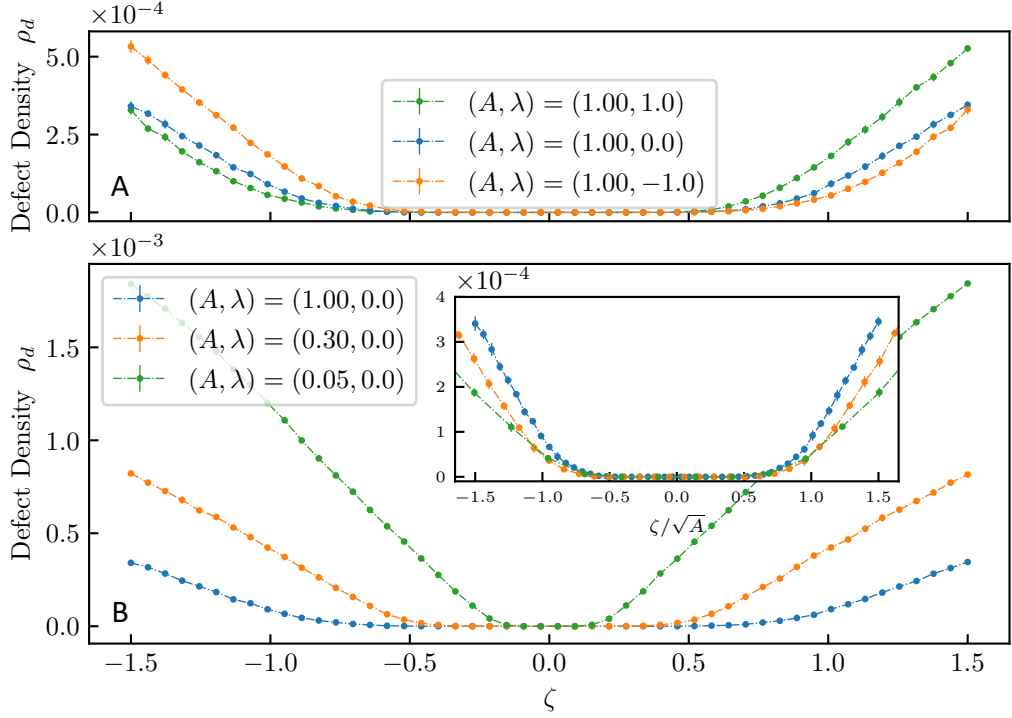


Figure 2.5: The steady-state defects density  $\rho_d$  dependence on (A) the flow-aligning parameters  $\lambda$  and (B) the bulk free-energy strength  $\mathcal{A}$ . The inset in panel (B) reveals that normalizing the active stress by  $\sqrt{\mathcal{A}}$  leads to a data collapse in the vicinity crossover point.

Figure 2.5A illustrates how defect density  $\rho_d$  changes with activity for three flow-aligning parameter values. When  $\lambda = 0$ , the activity threshold for defect formation is symmetric regardless of activity sign. Positive (negative) values shift the curve, reducing the threshold for extensile (contractile) activities compared to their counterparts, leading to more asymmetric defect density profiles. Consistent with the prediction. Figure 2.5B shows that reducing the energy scale  $\mathcal{A}$  in the bulk free-energy lowers the activity threshold for defect nucleation. This aligns with the mechanism for defect pair nucleation, where decreasing  $\mathcal{A}$  reduces the energy barrier for polarity flipping within kink walls (Fig. 2.4C-D), thus reducing the activity threshold, as predicted.

### 2.2.4 Universal scaling in defect-free and defect-laden active turbulence

The polarity power spectrum  $\hat{E}_p(k) = \frac{1}{2}\langle\hat{p}_i(k)\hat{p}_i(-k)\rangle$ , for a range of extensile activities spanning across both defect-free and defect-laden active turbulent states, is depicted in figure 2.6A as function wave vector magnitude averaged over azimuthal direction. When nondimensionalizing Fourier space by the active length scale  $L_{\text{act}} = \sqrt{K/|\zeta|}$  the power spectra  $\hat{E}_p(k)$  collapses onto each other and show exponential decay at length scales smaller than the active length scale. The kinetic energy  $\hat{E}_v(k) = \frac{1}{2}\langle\hat{v}_i(k)\hat{v}_i(-k)\rangle$  and enstrophy  $\hat{E}_w(k) = \frac{1}{2}\langle\hat{w}_i(k)\hat{w}_i(-k)\rangle$  spectra both exhibit power-law behavior at large length scale relative to the active length scale, as evident from figure 2.6C-D. This is significant, as it demonstrates that in polar active matter, both defect-free and defect-laden turbulence exhibit universal scaling laws despite their different symmetries (Fig. 2.2 top panel) and correlation lengths (Fig. 2.2 bottom panel).

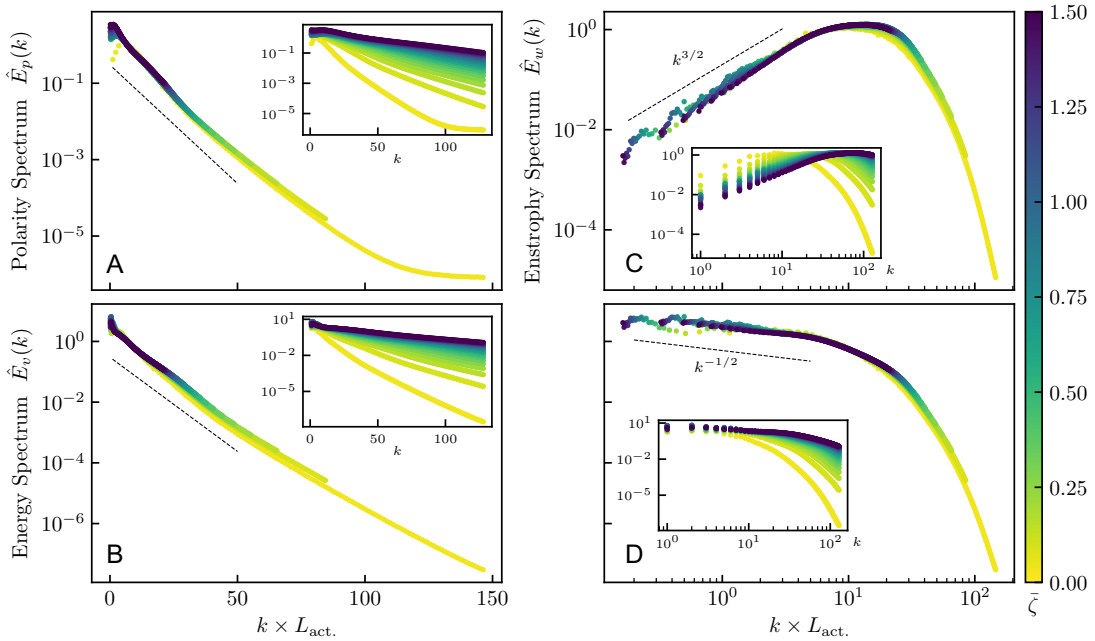


Figure 2.6: Power spectra for polarity (A), enstrophy (C), and kinetic energy on semi- (B) and double-logarithmic plot (D). All spectra are normalized with its corresponding maximum value.

## 2.3 Conclusion

In conclusion, the study elucidates the intricate dynamics of polar active particles, highlighting the pivotal role of active stresses in governing their collective behavior. Increasing active stress in polar active fluids induces a crossover from a defect-free state to a defect-laden active turbulence state. This crossover is marked by the nucleation of topological defects in the polar order parameter beyond a threshold activity, which effectively screens the global polar order and restores the  $SO(2)$  symmetry in the system. Despite the different topological characteristics of the two turbulence regimes, universal scaling is observed in the power spectra of polar order, flow velocity, and vorticity across both defect-free and defect-laden turbulent states.

## Bibliography

- [1] R Voituriez, Jean-François Joanny, and Jacques Prost. Spontaneous flow transition in active polar gels. *Europhy. Lett. (EPL)*, 70(3):404, 2005.
- [2] Luca Giomi, M Cristina Marchetti, and Tanniemola B Liverpool. Complex spontaneous flows and concentration banding in active polar films. *Physical review letters*, 101(19):198101, 2008.
- [3] Elsen Tjhung, Michael E Cates, and Davide Marenduzzo. Nonequilibrium steady states in polar active fluids. *Soft Matter*, 7(16):7453–7464, 2011.
- [4] Luca Giomi and M Cristina Marchetti. Polar patterns in active fluids. *Soft Matter*, 8(1):129–139, 2012.
- [5] Benjamin H Andersen, Julian Renaud, Jonas Rønning, Luiza Angheluta, and Amin Doostmohammadi. Symmetry-restoring crossover from defect-free to defect-laden turbulence in polar active matter. *Physical Review Fluids*, 8(6):063101, 2023.
- [6] Amin Doostmohammadi, Tyler N Shendruk, Kristian Thijssen, and Julia M Yeomans. Onset of meso-scale turbulence in active nematics. *Nature communications*, 8(1):1–7, 2017.
- [7] Suraj Shankar, Anton Souslov, Mark J Bowick, M Cristina Marchetti, and Vincenzo Vitelli. Topological active matter. *Nature Reviews Physics*, 4(6):380–398, 2022.
- [8] Farzan Vafa, Mark J Bowick, M Cristina Marchetti, and Boris I Shraiman. Multi-defect dynamics in active nematics. *arXiv:2007.02947*, 2020.
- [9] M. C. Marchetti, J. F. Joanny, S. Ramaswamy, T. B. Liverpool, J. Prost, Madan Rao, and R. Aditi Simha. Hydrodynamics of soft active matter. *Rev. Mod. Phys.*, 85:1143–1189, 2013.
- [10] Rayan Chatterjee, Navdeep Rana, R Aditi Simha, Prasad Perlekar, and Sri-ram Ramaswamy. Inertia drives a flocking phase transition in viscous active fluids. *Physical Review X*, 11(3):031063, 2021.
- [11] Aboutaleb Amiri, Romain Mueller, and Amin Doostmohammadi. Unifying polar and nematic active matter: emergence and co-existence of half-integer and full-integer topological defects. *Journal of Physics A: Mathematical and Theoretical*, 55(9):094002, feb 2022.

- [12] Amin Doostmohammadi, Jordi Ignés-Mullol, Julia M Yeomans, and Francesc Sagués. Active nematics. *Nat. Commun.*, 9(1):1–13, 2018.
- [13] Aleksandra Ardaševa and Amin Doostmohammadi. Topological defects in biological matter. *Nature Reviews Physics*, 4(6):354–356, 2022.
- [14] J M Kosterlitz and D J Thouless. Ordering, metastability and phase transitions in two-dimensional systems. *Journal of Physics C: Solid State Physics*, 6(7):1181, apr 1973.
- [15] BI Halperin. published in physics of defects, proceedings of les houches, session xxxv 1980 nato asi, editors balian, kléman and poirier, 1981.
- [16] Gene F Mazenko. Vortex velocities in the o (n) symmetric time-dependent ginzburg-landau model. *Physical review letters*, 78(3):401, 1997.
- [17] Vidar Skogvoll, Jonas Rønning, Marco Salvalaglio, and Luiza Angheluta. A unified field theory of topological defects and non-linear local excitations. *arXiv preprint arXiv:2302.03035*, 2023.
- [18] Hal Tasaki. Hohenberg-mermin-wagner-type theorems for equilibrium models of flocking. *Physical Review Letters*, 125(22):220601, 2020.

## Manuscript

TITLE: Symmetry-restoring crossover from defect-free to defect-laden turbulence in polar active matter

AUTHORS: Benjamin H. Andersen<sup>1</sup>, Julian Renaud<sup>2</sup>, Jonas Rønning<sup>3</sup>, Luiza Angheluta<sup>3</sup>, and Amin Doostmohammadi<sup>1</sup>

<sup>1</sup>Niels Bohr Institute, University of Copenhagen, Blegdamsvej 17, Copenhagen, Denmark.

<sup>2</sup>École Normale Supérieure, PSL Research University, 45 Rue d'Ulm, 75005 Paris, France.






<sup>3</sup>Njord Centre, Department of Physics, University of Oslo, P.O. Box 1048, 0316 Oslo, Norway.

MY CONTRIBUTION: Conducted simulations, created figures, and contributed to the writing of the manuscript.

PUBLICATION STATUS: Published in *Physical Review Fluids* (2023).

HYPERLINK: <https://doi.org/10.1103/PhysRevFluids.8.063101>

## Symmetry-restoring crossover from defect-free to defect-laden turbulence in polar active matter

Benjamin H. Andersen <sup>1</sup>, Julian Renaud <sup>2</sup>, Jonas Rønning <sup>3</sup>, Luiza Angheluta <sup>3,\*</sup>  
and Amin Doostmohammadi <sup>1,†</sup>

<sup>1</sup>Niels Bohr Institute, University of Copenhagen, Blegdamsvej 17, Copenhagen, Denmark

<sup>2</sup>École Normale Supérieure, PSL Research University, 45 Rue d'Ulm, 75005 Paris, France

<sup>3</sup>Njord Centre, Department of Physics, University of Oslo, P.O. Box 1048, 0316 Oslo, Norway



(Received 20 September 2022; accepted 24 May 2023; published 14 June 2023)

Coherent flows of self-propelled particles are characterized by vortices and jets that sustain chaotic flows, referred to as active turbulence. Here, we reveal a crossover between defect-free active turbulence and active turbulence laden with topological defects. Interestingly, we show that concurrent to the crossover from defect-free to defect-laden active turbulence is the restoration of the previously broken  $SO(2)$  symmetry signaled by the fast decay of the two-point correlations. By stability analyses of the topological charge density field, we provide theoretical insights on the criterion for the crossover to the defect-laden active turbulent state. Despite the distinct symmetry features between these two active turbulence regimes, the flow fluctuations exhibit universal statistical scaling behaviors at large scales, while the spectrum of polarity fluctuations decays exponentially at small length scales compared to the active energy injection length. These findings reveal a dynamical crossover between distinct spatiotemporal organization patterns in polar active matter.

DOI: [10.1103/PhysRevFluids.8.063101](https://doi.org/10.1103/PhysRevFluids.8.063101)

### I. INTRODUCTION

Recent developments in active matter have shed light on a form of chaotic flows sustained by living microswimmers at low Reynolds numbers, often known as *active turbulence* [1]. A distinctive feature of active turbulence, compared to classic inertial turbulence, is the continuous injection of energy at the scale of individual constituents of the active material. Striking examples are dense bacterial suspensions [2,3], cellular monolayers [4,5], and assemblies of subcellular filaments [6,7], which are all composed of active elements—i.e., individual bacterium, single cell, or motor proteins walking on single filaments—each capable of converting chemical energy to mechanical work [8–10]. Although, most of the work so far has been limited to visual resemblance with inertial turbulence, recent works suggest the existence of universal scaling features in active turbulence [7,11] and even show [12] that crossover to a confined active turbulence belongs to the same directed percolation universality class as in the inertial turbulence [13].

Nevertheless, a majority of studies of active turbulence so far, including the works suggesting universal scaling laws and universality classes of turbulence transition, have focused on a subclass of active materials known as *active nematics* [14–19], which models flows generated by dense assemblies of elongated particles [10]. Within the active nematic framework, the particles are essentially characterized as shakers [20]: they have neither any polarity nor ability to propel themselves and

\*luiza.angheluta@fys.uio.no

†doostmohammadi@nbi.ku.dk



instead generate head-tail symmetric (nematic) active stresses in the fluid. The active stresses in turn drive hydrodynamic instabilities in the flow and the orientation field of particles, resulting in a chaotic flow state that is interleaved with topological defects—singular points in the orientation field where the order breaks down [8,10,21].

Previous studies of polar active matter have characterized spontaneous flows [22,23] and associated nonequilibrium steady states [24,25]. On the other hand, studies of self-propulsion effects on active turbulence have mostly neglected orientational couplings. Instead, the focus has been put on generalized Navier-Stokes equations, where activity is introduced through the addition of phenomenological higher-order terms in the momentum equation, corresponding to a second-order negative viscosity and a fourth-order hyperviscosity, to give characteristic vortex length to active turbulence [2,26–28]. As such, characteristics of active turbulence in models of polar active fluids in the presence of topological defects have only been marginally explored in the context of polar active emulsions [29] and polar flocks with inertia [30]. Additionally, notwithstanding the interesting recent characterization of the annihilation of topological charges in colloidal flocks [31] and despite the emerging roles of topological defects in various biological fluids [32–35], the majority of research so far has focused on nematic topological defects [10,34,36] and studies of active turbulence in polar fluids in the presence of polar topological defects are lacking.

Here we use numerical simulations of continuum polar active matter together with analytical arguments to shed light on the turbulence characteristics of active fluids laden with topological defects, accounting for both hydrodynamic effects and polar ordering. We first show how increasing active stresses results in a regime shift from defect-free active turbulence to active topological turbulence, where chaotic flows are interleaved with chaotic arrangements of full-integer topological defects. We provide theoretical arguments to predict the activity threshold for the crossover to active topological turbulence, based on the stability analyses of the topological charge density field. We further show that ordering and symmetry characteristics are different within these two dynamical regimes: while  $SO(2)$  symmetry is broken within the defect-free active turbulence, the defect-laden turbulence restores the global  $SO(2)$  symmetry. Additionally, we demonstrate the existence of universal scaling behavior in the power spectra of enstrophy and polarity. This is observed for all activities and within both *defect-free* and *defect-laden* active turbulence.

## II. METHODS

### A. Hydrodynamic model

We consider an incompressible polar active fluid in two spatial dimensions, with the local orientational order described by a two-component order parameter  $\mathbf{p}$  pointing in the direction of self-propulsion. Let then  $\mathbf{u}$  and  $\rho$  be the velocity and density of the polar fluid, respectively. Coarse-grained hydrodynamic equations can be derived by phenomenological considerations [8,30,37] and take the form

$$\frac{D u_i}{D t} = \frac{1}{\rho} \partial_j \sigma_{ij}, \quad (1a)$$

$$\frac{D p_i}{D t} - (\lambda E_{ij} + \Omega_{ij}) p_j = \frac{1}{\gamma} h_i, \quad (1b)$$

along with the incompressibility condition  $\partial_i u_i = 0$ . Here  $\frac{D}{D t} = \partial_t + u_j \partial_j$  is the usual advective derivative. The strain rate tensor  $E_{ij} = (\partial_i u_j + \partial_j u_i)/2$  and the vorticity tensor  $\Omega_{ij} = (\partial_i u_j - \partial_j u_i)/2$  are respectively the symmetric and antisymmetric parts of the velocity gradient tensor. In the momentum balance Eq. (1a), the stress tensor  $\sigma_{ij}$  is broken into a sum of three parts: viscous stress  $\sigma_{ij}^{\text{vis.}} = 2\eta E_{ij}$ , passive stress  $\sigma_{ij}^{\text{pas.}} = -P\delta_{ij} + C_{ijkl} p_k h_l$ , and active stress  $\sigma_{ij}^{\text{act.}} = -\zeta(p_i p_j - \frac{p^2}{2} \delta_{ij})$  [38,39]. The first term in the passive stress is the usual hydrodynamic pressure. The second term accounts for elastic stresses through the anisotropic tensor  $C_{ijkl} = \frac{\lambda+1}{2} \delta_{ik} \delta_{jl} - \frac{\lambda}{2} \delta_{ij} \delta_{kl} + \frac{\lambda-1}{2} \delta_{il} \delta_{jk}$ , with  $\lambda$  being the flow alignment parameter and  $\mathbf{h} = -\delta\mathcal{F}/\delta\mathbf{p}$  [40,41] being the molecular field

defined here from the free energy

$$\mathcal{F} = \int d^2\mathbf{x} \left\{ A \left( -\frac{|\vec{p}|^2}{2} + \frac{|\vec{p}|^4}{4} \right) + \frac{K}{2} \partial_i p_j \partial_i p_j \right\}. \quad (2)$$

The free energy contains a local energy density with an energy scale  $A$  that controls the isotropic-polar transition favoring the emergence of finite polarity at  $|\mathbf{p}| = 1$ , and a nonlocal energy contribution with an elastic constant  $K$  that penalizes deformations in the polarity field [42]. It is important to note that we do not treat the polarity as a unit vector, with fixed magnitude. Instead, in this formulation the polarity modulus is an important dynamical variable.

### B. Numerical method and the simulation parameters

We simulate Eqs. (1a) and (1b) using a hybrid lattice-Boltzmann method, combining the finite-difference method for the evolution of the polarity vector, Eq. (1b), and the lattice-Boltzmann method for solving the incompressible Navier-Stokes equation, Eq. (1a), with  $\rho = 40$  and  $\eta = 3.6$  in lattice Boltzmann units, ensuring that the Reynolds number in the simulations is negligible ( $\text{Re} \ll 1$ ) [12,43]. The other relevant dimensionless numbers describing the system are (i) the dimensionless ratio of the viscosities  $\eta/\gamma$ , (ii) the ratio of micro to macro length scales  $(\sqrt{K/A})/L$ , (iii) the flow alignment parameter  $\lambda$ , and (iv) the dimensionless active stress  $\bar{\zeta} = \zeta/A$ . Unless otherwise stated, we fix the viscosity ratio to  $\eta/\gamma = 3.6$ , micro to macro length scale to  $(\sqrt{K/A})/L = 2 \times 10^{-4}$  (assuring that the coherence length  $l_p = \sqrt{K/A}$  is significantly smaller than the domain size  $L$ ), and the flow alignment parameter to  $\lambda = 0.1$ .

Simulations were initialized with quiescent velocity field and noisy polar alignments close to the uniformly oriented state  $\mathbf{p} = \hat{\mathbf{e}}_x$  under periodic boundary conditions, on quadratic domains of linear dimension  $L = 1024$ , unless otherwise is stated.

## III. RESULTS

### A. Activity-induced crossover to defect-laden turbulence

We begin by introducing global measures of the flow fluctuations and polar order parameter as functions of the activity parameter  $\bar{\zeta}$ . The flow is globally characterized by the dimensionless root-mean-squared (rms) velocity  $\bar{V}_{\text{rms}} = V_{\text{rms}}/V_p$  that is normalized by the characteristic velocity of passive relaxation of polarity  $V_p = \sqrt{AK}/\eta$ . The polar order parameter is associated with the SO(2) symmetry and carries full-integer topological defects. Its global measure is given by the average density of topological defects  $\rho_d = \langle N_d \rangle / L^2$ . The averaging is done both over space and time in the statistical steady-state regime. As evident from Fig. 1, increasing activity beyond a certain threshold results in a continuous increase in the defect density for both extensile ( $\zeta > 0$ ) and contractile ( $\zeta < 0$ ) systems. We have carefully checked that the activity thresholds do not depend on the system size  $L$ , by simulating different domain sizes of  $512 \times 512$ ,  $1024 \times 1024$ , and  $4096 \times 4096$  and finding precisely the same quantitative dependence of defect density on the activity (see Fig. 2; square and circle symbols). Interestingly, simultaneous measurement of the rms velocity  $\bar{V}_{\text{rms}}$  indicates that even below the critical activity for defect nucleation, active stresses disturb the polarity field such that spontaneous flows are generated within the system, for any nonzero activity [Fig. 1(c)]. A closer look at the velocity field of the system below the defect nucleation threshold shows that chaotic flows characterized by flow vortices and jets span the system [Fig. 1(a); only a fraction of the entire domain is shown], although no topological defects are present in the polarity field. Qualitatively similar chaotic flows manifest at higher activities with a smaller typical length scale  $L_{\text{act}}$ , defined below, though with the distinctive feature that the flows are now laden with the presence of full-integer topological defects (unbound vortex and antivortex pairs) in the polarity field [Fig. 1(b)]. Together, these results establish that there is a well-defined activity threshold for the crossover from defect-free and defect-laden active turbulence in polar active matter.

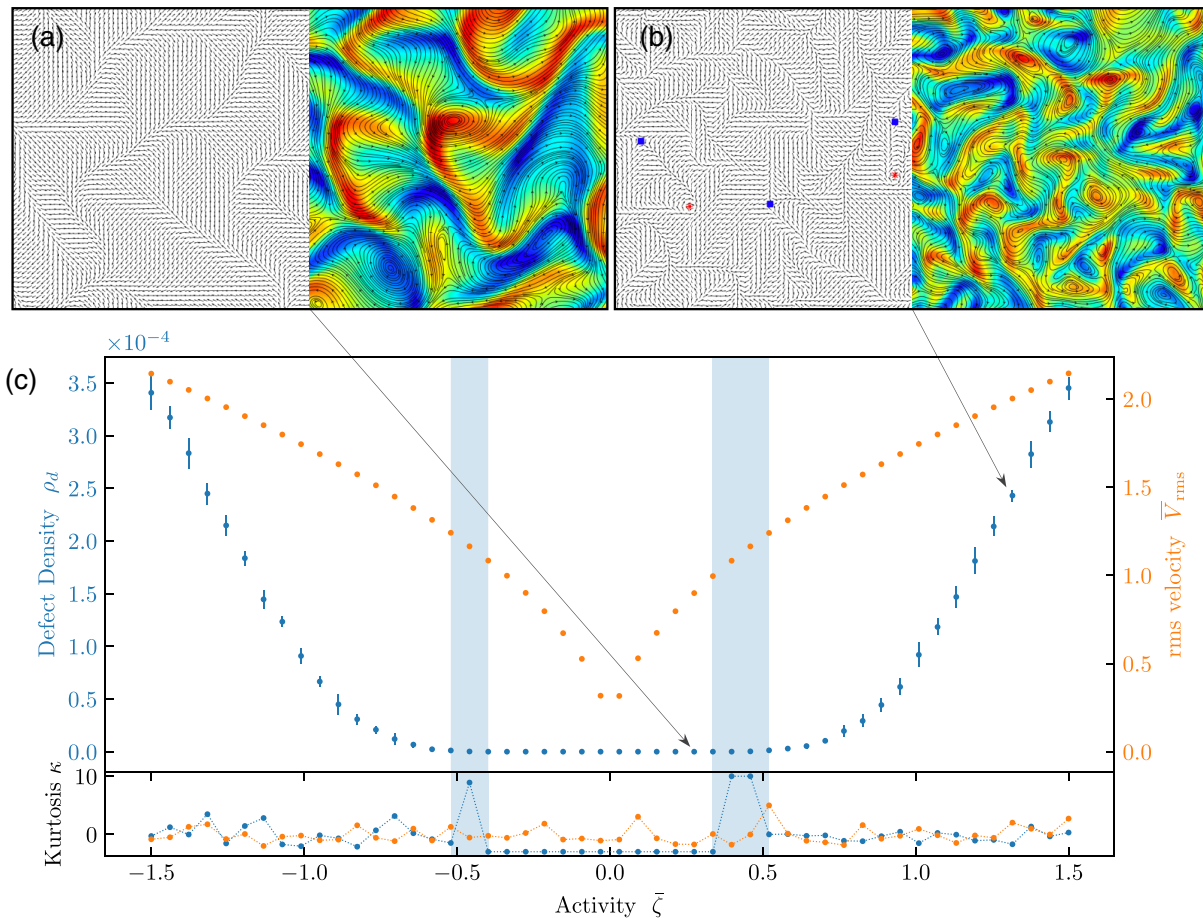


FIG. 1. Crossover from defect-free to defect-laden active turbulence upon increasing strength of active stresses. Shown here are the averaged defect density (blue dots) and the rms velocity (orange dots) in units of  $V_p = \sqrt{AK}/\eta$ , characterizing the passive relaxation velocity of the polar particles. Active turbulence arises as soon as the activity is nonzero, but topological defects form and persist in the polarity field only beyond a finite threshold in both contractile ( $\zeta < 0$ ) and extensile systems ( $\zeta > 0$ ). Results were averaged over time and for ten simulations from different initial conditions; the error bars stand for the corresponding standard deviation. The excess kurtosis  $\kappa_i$  values of both quantities are also represented at the bottom. For large activity levels,  $\kappa(\rho_d) \simeq 0$ , which indicates the population of defects is typically equilibriumlike and follows a normal distribution law. For small activity levels, there are no defects at all and  $\kappa$  is set by convention to  $-3$ . In between, the crossover is characterized by very rare formation and annihilation events, as evidenced by the peaks in  $\kappa$  (blue highlighted areas). There are no such peaks for the kurtosis of the rms velocity, which indicates there is no equivalent crossover regime. (a) and (b) illustrate the polarity field (left panels) and the corresponding velocity field (right panels) characterized by streamlines (solid black lines) colored by the normalized vorticity  $\omega/\omega_{\max}$ . Only a small subset of the full domain (1/16th zoomed-in region) is shown. Within the polarity field positive and negative integer topological defects are marked by red asters and blue squares, respectively.

### B. Global symmetry is restored in the defect-laden active turbulence

We next investigate whether the emergence of topological defects leads to alterations in the global ordering features of the polar active turbulence. To this end, we first introduce the global polarization  $\Psi$  as the spatiotemporal average value of the polarity field  $\mathbf{p}$ :

$$\Psi = \int \frac{dt}{T} \int \frac{d^2\mathbf{x}}{L^2} \mathbf{p}(t, \mathbf{x}). \quad (3)$$

The magnitude of this global polarization  $|\Psi|$  is a macroscopic order parameter for polar order akin to total magnetization in spin systems:  $|\Psi| = 0$  is associated with disordered states (i.e., continuous

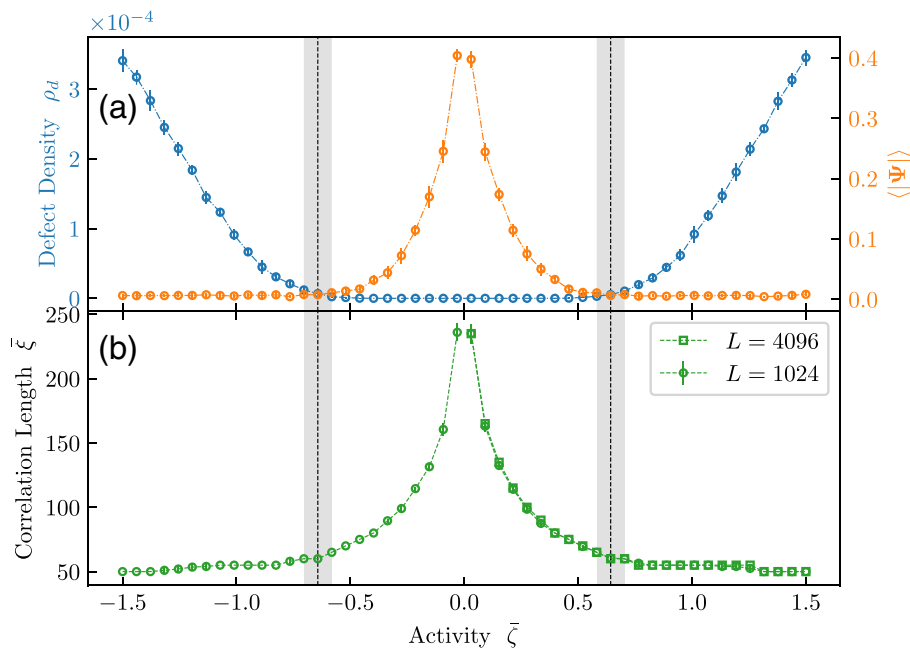


FIG. 2. Global symmetry restoration. (a) Averaged defect density  $\rho_d$ , blue solid line, and averaged magnitude of the global polarization  $\Psi$  [Eq. (3)], orange solid line. (b) The correlation length  $\bar{\xi}$  (in units of  $l_p = \sqrt{K/A}$ ) defined by fitting an exponential to the pair-correlation function  $\Gamma(r)$ . The square and circle symbols in panel (b) correspond to the simulations results for  $4096 \times 4096$  and  $1024 \times 1024$  domains, respectively, showing no detectable difference.

rotational symmetry) while  $|\Psi| > 0$  is associated with ordered states (discrete or broken rotational symmetry). We use this global measure to probe the crossover between the two active turbulence regimes as shown in Fig. 2(a) (orange solid line). Upon increasing the active stress from zero, the active turbulence state immediately manifests a broken  $SO(2)$  symmetry evident from a nonzero value of  $|\Psi|$  in the absence of topological defects. The global polarization decreases in magnitude with increasing activity and, remarkably, drops to zero beyond a critical activity for the nucleation of topological defects. This is indicative of the restoration of the  $SO(2)$  symmetry in the active defect-laden turbulence.

To further characterize the signature of this crossover, we also measure the equal-time, spatial pair-correlation function for the polarity field  $\Gamma(\mathbf{r}) = \langle \delta p_i(\mathbf{x}) \delta p_i(\mathbf{x} + \mathbf{r}) \rangle$ , where  $\delta p_i(\mathbf{r}) = p_i(\mathbf{r}) - \langle p_i(\mathbf{r}) \rangle$  is the deviation from the local mean value and the averaging is performed over ten different realizations, with distinct initial conditions and over time, once the system has reached a statistical steady state. Accordingly, the correlation length  $\xi$  is obtained by fitting an exponential to the pair-correlation function  $\Gamma(r)$ . Similar to the global polarization, the correlation length  $\bar{\xi} = \xi/l_p$ , normalized with respect to the coherence length  $l_p = \sqrt{K/A}$ , decreases with increasing activity (Fig. 2). The regime shift is marked by the crossover from the fast decay to the slow decay of the correlation length  $\bar{\xi}$ , which matched with the onset of defect nucleation and the vanishing of  $|\Psi| = 0$  as evidenced in Figs. 2(a) and 2(b). We have carefully checked that correlation measurements are independent of the domain sizes for very large systems up to  $4096 \times 4096$ . We note that the behavior of the correlation length shares interesting similarity to that in frustrated two-dimensional Heisenberg magnets, where a crossover between a topological defects dominated regime at high temperatures, and a spin-wave regime at low temperatures is observed [44]. Together, these measurements of the global polarization and the correlation length indicate that the crossover from defect-free to defect-laden active turbulence is marked by significant alterations in both the global symmetry of the collective organization and in the local correlations between the polarities of active constituents.

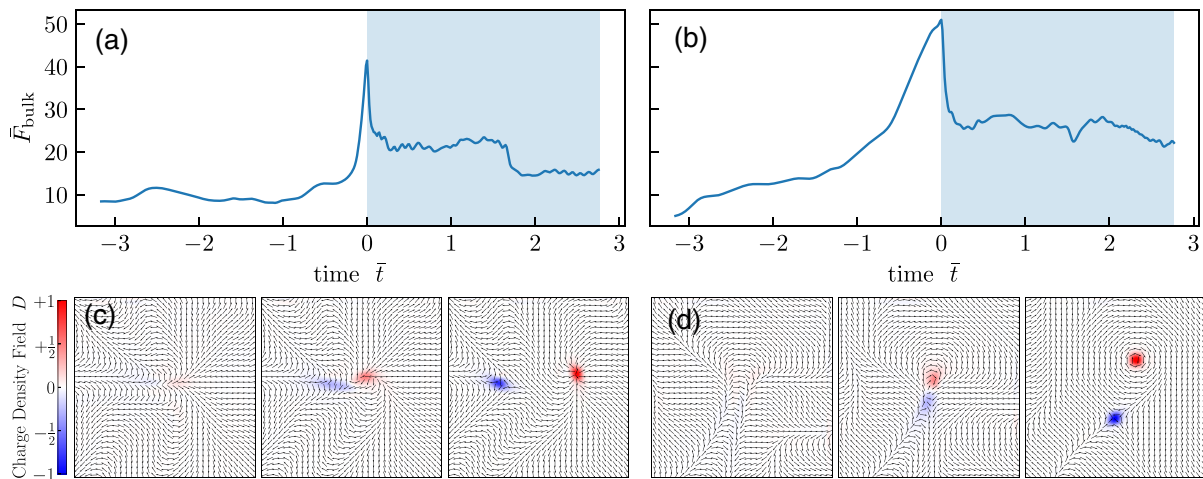


FIG. 3. Defect pair nucleation process. (a), (b) Temporal evolution of the average bulk free-energy  $\bar{F}_{\text{bulk}} = (F_{\text{bulk}} + A/4)/AL_{\text{act}}$ . (top panels) measured in units of  $AL_{\text{act}}$ , relative to the background field  $-A/4$ ; along with (c, d) simulation snapshots depicting the polarity field and diffuse charge density (heat plot) before, at, and after the nucleation of one pair of oppositely charged topological defects (bottom panels). Panels (a) and (c) are contractile, and panels (b) and (d) are extensile. The blue regions in panels (a) and (b) mark the period of existence of the defect pair considered. Time  $\bar{t}$  is measured in units of the passive relaxation time of polarity over the simulation domain  $t_p = \frac{\gamma L}{\sqrt{AK}}$  (see also Supplemental Movies [46]).

It is important to note that the observed restoration of the  $\text{SO}(2)$  symmetry is solely activity-driven and is in the noiseless limit of the equations of motion. Furthermore, the results presented in Fig. 2 demonstrate that, point-by-point, for any activity, (i) the correlation length, (ii) the polarization, and (iii) the defect density for domain sizes  $1024 \times 1024$  and  $4096 \times 4096$  fall exactly on top of each other. This strongly suggests a system-size independent behavior, at least for the numerically accessible system sizes. The question about the existence of a well-defined thermodynamic limit of this symmetry-breaking or symmetry-restoring transition remains open for future studies. Additionally, it is constructive to note that we do not observe any difference between longitudinal and transverse correlations in the polarity. The correlation length does not diverge with the system size within the ordered state, which we conjecture is due to the nonequilibrium nature of the system and the breaking of detailed balance [45] through activity-induced flows that couple to the dynamics of the order parameter.

### C. Mechanism of defect pair nucleation in active turbulence of polar particles

Having established the significant impact of the topological defects on the collective organization of polar active matter and its spontaneous flows, we next explore the mechanism of how topological defects are formed within the active turbulence state as the activity approaches the threshold value. Figure 3 illustrates zoomed-in snapshots of the polarity field at the onset of one defect pair nucleation. Three snapshots are shown at simulation times corresponding to the following: before, at, and after a single pair nucleation for both extensile and contractile active stresses. To identify and track topological defects, we make use of the diffuse charge density, defined in the next section as  $D = \frac{1}{2\pi} \epsilon_{ij} \epsilon_{kl} \partial_i p_k \partial_j p_l$ : it carries the  $\pm 1$  charge of the integer topological defect at the singularities in the polarity field and is zero elsewhere. Shortly before the onset of defect pair nucleation, the polarity field is characterized by locally ordered domains separated by lines of kink walls (Fig. 3 and Supplemental Movies [46]). At the onset of defect pair nucleation the polarity within one of the kink walls flips locally, leading to spontaneous emergence of a pair of full-integer defects (Fig. 3). After the nucleation event, the defect pair gets separated by an ordered region of polarity alignment (Fig. 3). While the negatively charged antivortices ( $-1$  topological defects) have similar structures

in both extensile and contractile systems, the positively charged +1 topological defects take the form of asters and vortices in contractile and extensile systems, respectively [Figs. 3(c) and 3(d)], in agreement with earlier analytical predictions on the stability of defect structures in polar active matter [47].

In order to gain more insight into the defect pair nucleation process, we measure the averaged bulk free-energy of the system from Eq. (2) during the time leading to a single defect pair nucleation event, as depicted in Figs. 3(a) and 3(b). For both extensile and contractile systems the onset of defect nucleation coincides with a burst in the bulk free-energy. This is consistent with the spontaneous flipping of the polarity within the kink walls that occurs when activity-induced fluctuations in the polarity overcome the energy barrier of local flipping, set by the bulk free-energy. Once the defect pair is formed, the bulk free-energy drops as the high energy stored in the kink walls is released. In the following section, we look more closely at this defect nucleation process and derive an analytical description of the activity threshold that is set by the competition between bulk and elastic energies of the system and by activity-induced flows.

#### D. Onset of active defect-laden turbulence

To gain more theoretical insights into the onset of defect pair nucleation, we perform a stability analysis of the topological charge density field. A stability analysis of the polarity field to probe the nucleation of topological defects is unfeasible since it is intrinsically nonlinear. However, we take advantage of the property of the topological charge density field being zero for low-energy excitations of the polarity field (aka kinks and domain walls) to study the onset of defect nucleation as an instability to a nonzero and localized charge density field. To this end, we employ the Halperin-Mazenko method [48–50] of topological defects as zeros in the polarity vector field  $\mathbf{p}$ , i.e., localized regions where  $\mathbf{p}$  vanishes in magnitude while its orientation is undefined (multivalued). The associated topological charge is a quanta of the phase jump measured around an arbitrary contour  $C_\alpha$  enclosing the defect

$$2\pi q_\alpha = \oint_{C_\alpha} d\mathbf{l} \cdot \nabla\theta, \quad (4)$$

where  $\theta = \arg(\mathbf{p})$ . By Stokes' theorem, we see that topological defects correspond to phase singularities where the phase ceases to be irrotational,

$$2\pi q_\alpha \int_{A_\alpha} d^2\mathbf{x} \delta(\mathbf{x} - \mathbf{x}_\alpha) = \int_{A_\alpha} d^2\mathbf{x} \nabla \times \nabla\theta. \quad (5)$$

As shown in Ref. [50], the topological content inside an area region  $A_\alpha$  can be also obtained from the corresponding integration in the order parameter space  $\mathbf{p} = (p_1, p_2)$ :

$$2\pi q_\alpha \int_{A_\alpha} d^2\mathbf{x} \delta(\mathbf{x} - \mathbf{x}_\alpha) = \int d^2\mathbf{p} \det(\nabla\mathbf{p}) \delta(\mathbf{p}). \quad (6)$$

We relate the topological defect density  $D$  with the Jacobi determinant of the transformation to the order parameter space, which is the same as the determinant of the distortion tensor  $\nabla\mathbf{p}$ , to define

$$D = \frac{1}{2} \epsilon_{ij} \epsilon_{kl} \partial_i p_k \partial_j p_l, \quad (7)$$

which is a smooth scalar field that vanishes where  $\mathbf{p}$  is smooth and becomes nonzero and localized at the core of topological defect, picking up the phase singularity. We have validated the defects detected by  $D$  field against our routine approach of using winding angles and have obtained identical results, in agreement with previous studies on active nematics, where the  $D$  field was defined as the diffuse charge density [51–53]. The  $D$  field has the physical interpretation of a nonsingular topological charge density field which follows the conservation law [50]

$$\partial_i D + \partial_j J_i = 0, \quad (8)$$

with the corresponding topological current density

$$J_i = -\epsilon_{ij\epsilon kl} \partial_t p_k \partial_j p_l, \quad (9)$$

which is fully determined by the evolution of the polarity  $\mathbf{p}$  and the flow field  $\mathbf{u}$  through the main equations, Eqs. (1b) and (1a).

We perform a stability analysis of Eq. (8) around the ground state of zero  $D$  associated with slowly varying polar order to estimate the critical activity for the onset of defect nucleation, identified as an instability where  $D$  becomes nonzero because polar order vanishes locally. In general, the evolution of  $D$ , resulting from inserting the evolution of  $\mathbf{p}$  from Eq. (1b) into Eq. (8), cannot be closed only in terms of the  $D$  field. However, in the limit of retaining only the shear flow alignment contribution and the molecular field, the evolution of  $\mathbf{p}$  from Eq. (8) can be reduced to

$$\partial_t D = \epsilon_{ij\epsilon kl} \left[ \lambda \partial_i (E_{kn} p_n) \partial_j p_l + \frac{1}{\gamma} \partial_i h_k \partial_j p_l \right]. \quad (10)$$

Now, by balancing viscous stress with the active stress in Eq. (1a), we relate the traceless strain rate  $E_{kn}$  directly to the nematic order parameter, namely,

$$E_{kn} = \frac{\zeta}{2\eta} \left( p_n p_k - \frac{p^2}{2} \delta_{nk} \right), \quad (11)$$

such that the flow alignment contribution dominated by orientational distortion has a closed form given by

$$\begin{aligned} \frac{\zeta \lambda}{4\eta} \epsilon_{ij\epsilon kl} \partial_i (p^2 p_k) \partial_j p_l &= \frac{\zeta \lambda}{4\eta} (p^2 \epsilon_{ij\epsilon kl} \partial_i p_k \partial_j p_l + 2\epsilon_{ij\epsilon kl} p_k p_m \partial_i p_m \partial_j p_l) \\ &= \frac{\zeta \lambda}{2\eta} p^2 D + \frac{\zeta \lambda}{2\eta} p^2 (\partial_1 p_1 \partial_2 p_2 - \partial_2 p_1 \partial_1 p_2) = \frac{\zeta \lambda}{\eta} p^2 D. \end{aligned} \quad (12)$$

The molecular field is due to the elastic distortions and the ordering potential

$$h_k = K \nabla^2 p_k + A(1 - p^2) p_k,$$

and it leads to the contribution

$$\epsilon_{ij\epsilon kl} \partial_i h_k \partial_j p_l = K \nabla^2 D + 2A(1 - 2p^2) D.$$

Thus, within this limiting case, the evolution of the  $D$  field reduces to a diffusion-reaction equation:

$$\partial_t D \approx \frac{K}{\gamma} \nabla^2 D + \left( \frac{2A}{\gamma} (1 - 2p^2) + \frac{\zeta \lambda}{\eta} p^2 \right) D. \quad (13)$$

First, we notice that the polarity stiffness  $K$  enters as an effective diffusivity coefficient and sets the scale of the diffusive core. The kinetic rate coefficients arise from the stabilizing passive contribution through the energy scale parameter  $A$  of the local order potential and its relaxation timescale  $\gamma$ , as well as from the destabilizing contribution through the term that includes flow alignment  $\lambda$ , activity  $\zeta$ , and viscosity  $\eta$ . At first sight, Eq. (13) looks nonconservative due to the source/sink term. This is, however, not the case since this term is derived from a conservative current and is related to the fact that the  $D$  field itself is the divergence of a vector field,  $D = \partial_i (\epsilon_{ij\epsilon kl} p_k \partial_j p_l) / 2$ . We estimate the critical activity from the linear stability analysis of Eq. (13) about the ordered state  $p = 1 + \delta p$  and  $D = \delta D$ . By balancing out the two contributions to the reaction term we find that the equation becomes unstable at

$$\zeta_c \approx \frac{2\eta}{\gamma \lambda} A. \quad (14)$$

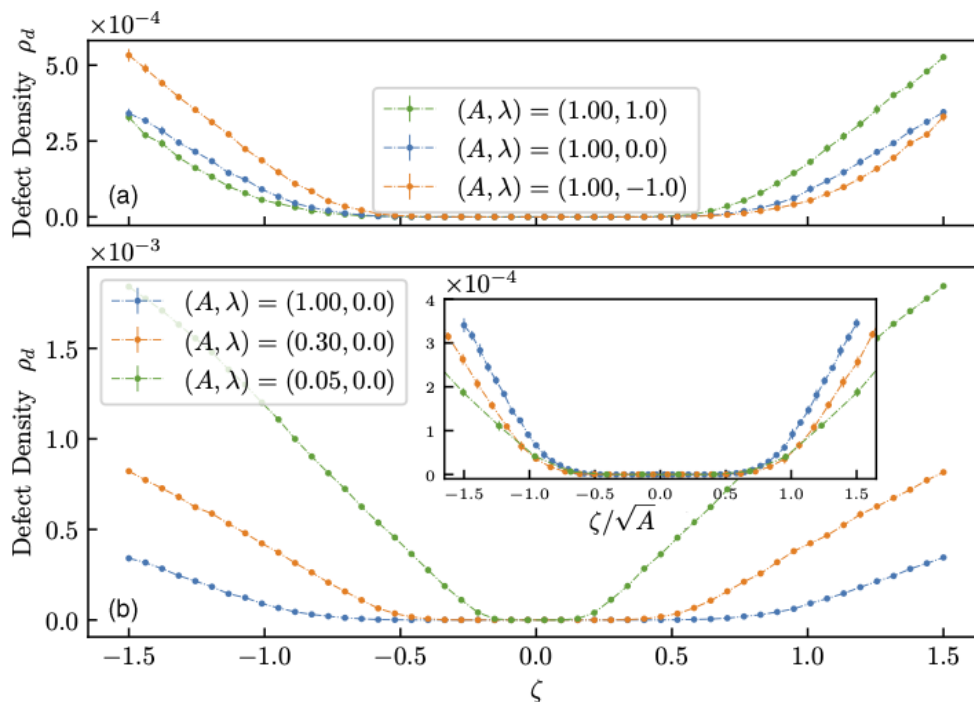


FIG. 4. Dependence of the steady-state density of defects on (a) the flow-aligning parameters  $\lambda$  and (b) the bulk free-energy strength  $A$ . Inset in panel (b) shows that normalizing the active stress by  $\sqrt{A}$  results in a data collapse near the crossover point.

Thus, in the limit where we neglect the convective and rotational terms to the evolution of the  $D$  field (i.e.,  $\mathbf{u} \cdot \nabla \mathbf{p}$  and  $[\boldsymbol{\Omega}, \mathbf{p}]$ ), the topological charge density becomes unstable to defect nucleation only for extensile systems where  $\zeta > 0$ . This instability is due to the flow alignment.

Advection and rotation of polarity  $\mathbf{p}$ , due to flow velocity and vorticity, could also trigger instabilities in the  $D$  field. Alas, their contributions are nonlocal through viscosity and incompressibility constraint and cannot be reduced to linear operators acting on  $D$ . However, it turns out that the contribution of vorticity to the  $D$  evolution is symmetric with respect to the sign of  $\zeta$ , and, from this, we can infer that an instability induced by vorticity would occur at a critical activity both for extensile and contractile systems, also symmetric with respect to the sign of  $\zeta$ .

It is important to note that in numerical simulations all these destabilizing forces orchestrate and compete with the relaxation to uniform order. Therefore, the value of the critical activity is different than the estimated one corresponding to an isolated triggering factor. However, this stability analysis is informative and predicts generic properties of  $\zeta_c$ : (i) it depends on the energy scale  $A$  controlling polar order, and (ii) the threshold activity has an asymmetry with respect to extensile and contractile active stresses in the presence of flow alignment.

To test the theoretical predictions on the activity threshold for defect nucleation, we next explore the dependence of defect density on the flow-aligning parameter  $\lambda$  and the energy scale  $A$  for the bulk free-energy. Figure 4(a) compares the variation of the defect density  $\rho_d$  with activity for three values of the flow-aligning parameter  $\lambda$ . Interestingly, and consistently with the theoretical prediction, for  $\lambda = 0$  the activity threshold for defect nucleation is symmetric with respect to the sign of the activity. Additionally, as predicted from the theory, a positive (negative) flow-aligning parameter shifts the defect density curve such that the activity threshold becomes smaller—in absolute value—for extensile (contractile) activities compared to their contractile (extensile) counterparts, leading to a more asymmetric profile of the defect density with respect to the sign of the activity. Moreover, as predicted from the theory, decreasing the energy scale in the bulk free-energy  $A$  lowers the activity threshold for defect nucleation [Fig. 4(b)]. This is also consistent with the mechanism identified for the nucleation of pairs of defects, relying on the spontaneous flipping of the polarity within the kink



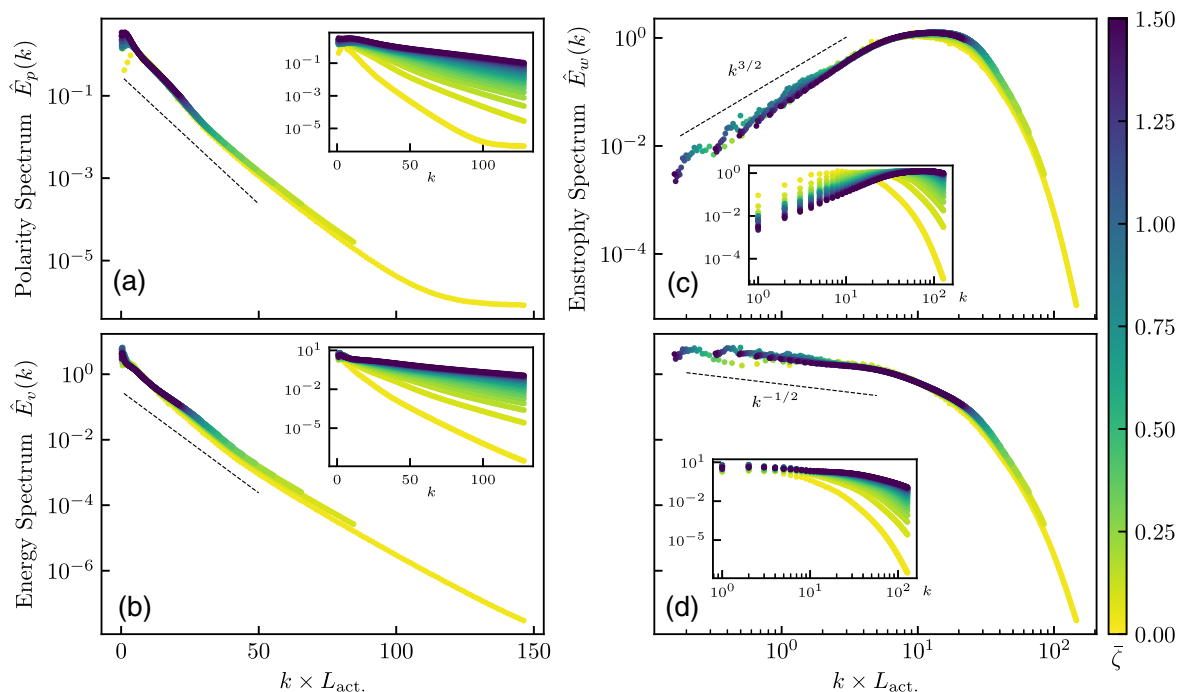


FIG. 5. Universal scaling in defect-free and defect-laden active turbulence. Power spectra normalized with its corresponding maximum value for (a) polarity  $\hat{E}_p(k)$  and (b) kinetic energy  $\hat{E}_v(k)$  on semilog plots, demarcating the exponential decay at small scales (large wave numbers), which implies the dynamics is dominated by viscous dissipation. (c), (d) Power spectra normalized with its corresponding maximum value for (c) the enstrophy  $\hat{E}_w(k)$  and (d) the kinetic energy again, on log-log plots, showing the power-law scaling at scales larger than the active length scale  $L_{\text{act.}}$ . Insets show the nonscaled power spectra and the colorbar indicates the dimensionless active stress strength  $\bar{\zeta}$ .

walls (Figs. 3(c) and 3(d) and Supplemental Movies [46]): since the parameter  $A$  sets the depth of a double-well potential in the bulk free-energy, decreasing its value amounts to lowering the energy barrier for flipping the polarity, and as such leads to a reduced activity threshold for defect pair nucleation.

### E. Universal scaling in defect-free and defect-laden active turbulence

Having established the mechanism of defect nucleation and the difference between defect-free and defect-laden active turbulence, we now investigate the common features between these two active turbulent states by characterizing the energetic features of the flow and order parameters (Fig. 5). To this end, we first measure the power spectrum of the polarity order parameter  $\hat{E}_p(k) = \frac{1}{2} \langle \hat{p}_i(k) \hat{p}_i(-k) \rangle$ , with  $k$  being the wave number averaged over azimuthal direction, for a range of activities spanning both defect-free and defect-laden turbulent states. Interestingly, when the wave number is nondimensionalized by the active length scale  $L_{\text{act.}} = \sqrt{K/|\zeta|}$ , which characterizes the scale of energy injection into the system by active stresses, the power spectrum  $\hat{E}_p$  for all activity values shows an exponential decay at *wave numbers larger than the inverse active length scale*, as evident from a semilog plot of the order parameter spectrum versus the normalized wave number [Fig. 5(a)]. The exponential cutoff scale still depends on activity and approaches a constant value at sufficiently high activity. This is related to the initial fast decay of the correlation function  $\Gamma(r)$ , with a correlation length that is activity dependent as discussed earlier. Notice that the exponential dependence of  $\hat{E}_p$  on  $k$  breaks down for small wave numbers. On the other hand, robust exponential tails at large wave numbers are characteristic for the spectral properties of the spontaneous flow, measured by the kinetic energy spectrum  $\hat{E}_v(k) = \frac{1}{2} \langle \hat{v}_i(k) \hat{v}_i(-k) \rangle$ , with

$\hat{v}_i$  being the Fourier transforms of flow velocity [Fig. 5(b)]. However, for *wave numbers below the inverse active length scale*, the kinetic energy spectrum  $\hat{E}_v(k)$  and the enstrophy spectrum  $\hat{E}_\omega(k) = \frac{1}{2} \langle \hat{\omega}(k) \hat{\omega}(-k) \rangle \sim k^2 \hat{E}_v(p)$  both exhibit power-law behavior [Figs. 5(c) and 5(d)]. This is important, because these activity levels span both the defect-free and the defect-laden active turbulence states, indicating that for a polar active matter, despite distinct symmetry features and correlation lengths, there exist universal scaling of flow and order parameter spectrum in the active turbulence state with and without topological defects. In particular, the enstrophy power spectrum that relates to the flow field shows a universal *power-law* scaling at length scales larger than the active length  $L_{\text{act.}}$ , while the polarity power spectrum that relates to the order parameter field shows a universal *exponential decay* at length scales smaller than the active length scale. These two distinct scaling relate defect-free and defect-laden turbulence in polar active matter. It is important to note that the scaling observed here is different from the power-law scaling suggested for active nematic turbulence without topological defects, where the orientational field is treated as a unit vector field with fixed modulus [11]. The heuristic argument of the scaling behavior reported in Ref. [11] is based on a spectral analysis of the equation for the vorticity source to argue for the power-law scaling of  $\hat{E}_p(k)$  and  $\hat{E}_v(k)$  at small  $k$ . The scaling argument hinges on two important assumptions: (i) the vorticity source is dominated by the active stress determined only by phase gradients; (ii) at small  $k$  (long wavelength) phase fluctuations become uncorrelated. Both of these assumptions fail to apply when the polarity magnitude is allowed to vary, since the vorticity fluctuations couple with fluctuations in both the magnitude and the phase of the polarity. Thus, the power spectrum of the vorticity source is not trivially related to the polarity power spectrum by extending the scaling analysis from Ref. [11]. Therefore, we do not expect to observe the same scaling behavior at long wavelength as in Ref. [11].

#### IV. DISCUSSION

The results presented herein reveal distinct flow fields and patterns of collective self-organization of polar active particles that are primarily controlled by active stresses. We show that increasing active stress in a polar active fluid leads to a dynamical crossover from a defect-free to a defect-laden active turbulence state. Above a critical activity threshold, the turbulent flow is seeded with topological defects nucleated in the polar order parameter. Importantly, we find that the proliferation of defects screens the global polar order. Thus, in the defect-laden turbulent states the SO(2) symmetry is restored, whereas the defect-free active turbulence is endowed with broken SO(2) symmetry.

Interestingly, we show that in spite of their distinct topological content, the two active turbulence regimes share similar statistical properties with robust exponential tails for power spectra of polar order, flow velocity, and vorticity on length scales smaller than the active length scale. On the other hand, over the length scales that are larger than the active length scale, enstrophy and energy spectra of flow fluctuations exhibit self-similarity with power-law scaling exponents. These statistical properties are also universal in the sense that they do not depend on the presence of topological defects, which may indicate that nontopological dissipative structures (e.g., kink walls) are the dominant driving force to fluctuations in order and flow of polar active fluids.

It is noteworthy that despite the ubiquitous presence of polarity in living and synthetic active materials [8,9], the majority of the current understanding of topological defects and flow features within the active turbulence is based on studies of active nematics. This is in part due to the growing number of biological systems that are identified with half-integer, nematic, topological defects [21,32,34] and discovery of potential biological functions for such defects [53–55]. It is important to note, however, that full-integer defects have also been identified as possible organization centers for mitotic spindles in microtubule-motor protein assemblies [56] and more recently as potential sites for mechanotransduction [35], and for cell differentiation in mouse myoblasts [33] and cartilage cells [57]. Our results provide a quantitative characterization of the dynamical crossovers, as well as the statistical imprints of flow and topological defects in polar active matter. Future work should focus on details of the dynamic distinctions in topological and flow features between the active

turbulence in polar and nematic active materials, as well as generalized frameworks of the coupling between polar and nematic symmetries that have already been suggested theoretically [37,58,59] and observed experimentally [56,57].

#### ACKNOWLEDGMENTS

A.D. acknowledges funding from the Novo Nordisk Foundation (Grant No. NNF18SA0035142 and NERD Grant No. NNF21OC0068687), Villum Fonden Grant No. 29476, and the European Union via the ERC-Starting Grant PhysCoMeT Grant No. 101041418. J.R. and L.A. acknowledge support from the Research Council of Norway through the Center of Excellence funding scheme, Project No. 262644 (PoreLab).

- 
- [1] R. Alert, J. Casademunt, and J.-F. Joanny, Active turbulence, *Annu. Rev. Condens. Matter Phys.* **13**, 143 (2022).
  - [2] H. Wensink, J. Dunkel, S. Heidenreich, K. Drescher, R. E. Goldstein, H. Löwen, and J. M. Yeomans, Meso-scale turbulence in living fluids, *Proc. Natl. Acad. Sci. USA* **109**, 14308 (2012).
  - [3] O. J. Meacock, A. Doostmohammadi, K. R. Foster, J. M. Yeomans, and W. M. Durham, Bacteria solve the problem of crowding by moving slowly, *Nat. Phys.* **17**, 205 (2021).
  - [4] C. Blanch-Mercader, V. Yashunsky, S. Garcia, G. Duclos, L. Giomi, and P. Silberzan, Turbulent Dynamics of Epithelial Cell Cultures, *Phys. Rev. Lett.* **120**, 208101 (2018).
  - [5] S.-Z. Lin, W.-Y. Zhang, D. Bi, B. Li, and X.-Q. Feng, Energetics of mesoscale cell turbulence in two-dimensional monolayers, *Commun. Phys.* **4**, 21 (2021).
  - [6] T. Sanchez, D. T. N. Chen, S. J. DeCamp, M. Heymann, and Z. Dogic, Spontaneous motion in hierarchically assembled active matter, *Nature (London)* **491**, 431 (2012).
  - [7] B. Martínez-Prat, R. Alert, F. Meng, J. Ignés-Mullol, J.-F. Joanny, J. Casademunt, R. Golestanian, and F. Sagués, Scaling Regimes of Active Turbulence with External Dissipation, *Phys. Rev. X* **11**, 031065 (2021).
  - [8] M. C. Marchetti, J. F. Joanny, S. Ramaswamy, T. B. Liverpool, J. Prost, M. Rao, and R. A. Simha, Hydrodynamics of soft active matter, *Rev. Mod. Phys.* **85**, 1143 (2013).
  - [9] C. Bechinger, R. Di Leonardo, H. Löwen, C. Reichhardt, G. Volpe, and G. Volpe, Active particles in complex and crowded environments, *Rev. Mod. Phys.* **88**, 045006 (2016).
  - [10] A. Doostmohammadi, J. Ignés-Mullol, J. M. Yeomans, and F. Sagués, Active nematics, *Nat. Commun.* **9**, 3246 (2018).
  - [11] R. Alert, J.-F. Joanny, and J. Casademunt, Universal scaling of active nematic turbulence, *Nat. Phys.* **16**, 682 (2020).
  - [12] A. Doostmohammadi, T. N. Shendruk, K. Thijssen, and J. M. Yeomans, Onset of meso-scale turbulence in active nematics, *Nat. Commun.* **8**, 15326 (2017).
  - [13] G. Lemoult, L. Shi, K. Avila, S. V. Jalikop, M. Avila, and B. Hof, Directed percolation phase transition to sustained turbulence in Couette flow, *Nat. Phys.* **12**, 254 (2016).
  - [14] S. Ngo, A. Peshkov, I. S. Aranson, E. Bertin, F. Ginelli, and H. Chaté, Large-Scale Chaos and Fluctuations in Active Nematics, *Phys. Rev. Lett.* **113**, 038302 (2014).
  - [15] J. Urzay, A. Doostmohammadi, and J. M. Yeomans, Multi-scale statistics of turbulence motorized by active matter, *J. Fluid Mech.* **822**, 762 (2017).
  - [16] Ž. Krajnik, Ž. Kos, and M. Ravnik, Spectral energy analysis of bulk three-dimensional active nematic turbulence, *Soft Matter* **16**, 9059 (2020).
  - [17] L. N. Carenza, L. Biferale, and G. Gonnella, Cascade or not cascade? energy transfer and elastic effects in active nematics, *Europhys. Lett.* **132**, 44003 (2020).
  - [18] R. C. V. Coelho, N. A. M. Araújo, and M. M. T. da Gama, Propagation of active nematic–isotropic interfaces on substrates, *Soft Matter* **16**, 4256 (2020).

- [19] S. Chandragiri, A. Doostmohammadi, J. M. Yeomans, and S. P. Thampi, Flow States and Transitions of an Active Nematic in a Three-Dimensional Channel, *Phys. Rev. Lett.* **125**, 148002 (2020).
- [20] S. Ramaswamy, The mechanics and statistics of active matter, *Annu. Rev. Condens. Matter Phys.* **1**, 323 (2010).
- [21] A. Ardaševa and A. Doostmohammadi, Topological defects in biological matter, *Nat. Rev. Phys.* **4**, 354 (2022).
- [22] R. Voituriez, J. F. Joanny, and J. Prost, Generic Phase Diagram of Active Polar Films, *Phys. Rev. Lett.* **96**, 028102 (2006).
- [23] L. Giomi, M. C. Marchetti, and T. B. Liverpool, Complex Spontaneous Flows and Concentration Banding in Active Polar Films, *Phys. Rev. Lett.* **101**, 198101 (2008).
- [24] E. Tjhung, M. E. Cates, and D. Marenduzzo, Nonequilibrium steady states in polar active fluids, *Soft Matter* **7**, 7453 (2011).
- [25] L. Giomi and M. C. Marchetti, Polar patterns in active fluids, *Soft Matter* **8**, 129 (2012).
- [26] V. Bratanov, F. Jenko, and E. Frey, New class of turbulence in active fluids, *Proc. Natl. Acad. Sci. USA* **112**, 15048 (2015).
- [27] M. Linkmann, G. Boffetta, M. C. Marchetti, and B. Eckhardt, Phase Transition to Large Scale Coherent Structures in Two-Dimensional Active Matter Turbulence, *Phys. Rev. Lett.* **122**, 214503 (2019).
- [28] M. Linkmann, M. C. Marchetti, G. Boffetta, and B. Eckhardt, Condensate formation and multiscale dynamics in two-dimensional active suspensions, *Phys. Rev. E* **101**, 022609 (2020).
- [29] L. N. Carenza, L. Biferale, and G. Gonnella, Multiscale control of active emulsion dynamics, *Phys. Rev. Fluids* **5**, 011302(R) (2020).
- [30] R. Chatterjee, N. Rana, R. A. Simha, P. Perlekar, and S. Ramaswamy, Inertia Drives a Flocking Phase Transition in Viscous Active Fluids, *Phys. Rev. X* **11**, 031063 (2021).
- [31] A. Chardac, L. A. Hoffmann, Y. Poupart, L. Giomi, and D. Bartolo, Topology-Driven Ordering of Flocking Matter, *Phys. Rev. X* **11**, 031069 (2021).
- [32] B. I. Halperin, Statistical mechanics of topological defects, in *Physics of Defects*, edited by R. Balian, M. Kleman, and J.-P. Poirier (North-Holland, Amsterdam, 1981), pp. 814–857.
- [33] P. Guillamat, C. Blanch-Mercader, G. Pernollet, K. Kruse, and A. Roux, Integer topological defects organize stresses driving tissue morphogenesis, *Nat. Mater.* **21**, 588 (2022).
- [34] S. Shankar, A. Souslov, M. J. Bowick, M. C. Marchetti, and V. Vitelli, Topological active matter, *Nat. Rev. Phys.* **4**, 380 (2022).
- [35] K. D. Endresen, M. Kim, M. Pittman, Y. Chen, and F. Serra, Topological defects of integer charge in cell monolayers, *Soft Matter* **17**, 5878 (2021).
- [36] F. Vafa, M. J. Bowick, M. C. Marchetti, and B. I. Shraiman, Multi-defect dynamics in active nematics, [arXiv:2007.02947](https://arxiv.org/abs/2007.02947).
- [37] A. Amiri, R. Mueller, and A. Doostmohammadi, Unifying polar and nematic active matter: Emergence and co-existence of half-integer and full-integer topological defects, *J. Phys. A: Math. Theor.* **55**, 094002 (2022).
- [38] J. Prost, F. Jülicher, and J.-F. Joanny, Active gel physics, *Nat. Phys.* **11**, 111 (2015).
- [39] F. Jülicher, S. W. Grill, and G. Salbreux, Hydrodynamic theory of active matter, *Rep. Prog. Phys.* **81**, 076601 (2018).
- [40] P. G. De Gennes and J. Prost, *The Physics of Liquid Crystals*, International Series of Monographs on Physics Volume 83 (Oxford University, Oxford, 1993).
- [41] S. Chandragiri, A. Doostmohammadi, J. M. Yeomans, and S. P. Thampi, Active transport in a channel: Stabilisation by flow or thermodynamics, *Soft Matter* **15**, 1597 (2019).
- [42] F. C. Frank, I. Liquid crystals. On the theory of liquid crystals, *Discuss. Faraday Soc.* **25**, 19 (1958).
- [43] S. P. Thampi, R. Golestanian, and J. M. Yeomans, Instabilities and topological defects in active nematics, *Europhys. Lett.* **105**, 18001 (2014).
- [44] N. Hasselmann and A. Sinner, Interplay of topology and geometry in frustrated two-dimensional heisenberg magnets, *Phys. Rev. B* **90**, 094404 (2014).
- [45] H. Tasaki, Hohenberg-Mermin-Wagner-Type Theorems for Equilibrium Models of Flocking, *Phys. Rev. Lett.* **125**, 220601 (2020).

- [46] See Supplemental Material at <http://link.aps.org/supplemental/10.1103/PhysRevFluids.8.063101> for simulations of the polarity field and diffuse charge density (heat plot) in contractile and extensile systems.
- [47] K. Kruse, J.-F. Joanny, F. Jülicher, J. Prost, and K. Sekimoto, Asters, Vortices, and Rotating Spirals in Active Gels of Polar Filaments, *Phys. Rev. Lett.* **92**, 078101 (2004).
- [48] B. I. Halperin, in *Physics of Defects*, edited by R. Balian, M. Kléman, and J.-P. Poirier, Proceedings of the Les Houches Summer School of Theoretical Physics, XXXV, 1981 (North Holland, Amsterdam, 1981).
- [49] G. F. Mazenko, Vortex Velocities in the  $O(n)$  Symmetric Time-Dependent Ginzburg-Landau Model, *Phys. Rev. Lett.* **78**, 401 (1997).
- [50] V. Skogvoll, J. Rønning, M. Salvalaglio, and L. Angheluta, A unified field theory of topological defects and non-linear local excitations, [arXiv:2302.03035](https://arxiv.org/abs/2302.03035).
- [51] M. L. Blow, S. P. Thampi, and J. M. Yeomans, Biphasic, Lyotropic, Active Nematics, *Phys. Rev. Lett.* **113**, 248303 (2014).
- [52] A. Doostmohammadi, S. P. Thampi, and J. M. Yeomans, Defect-Mediated Morphologies in Growing Cell Colonies, *Phys. Rev. Lett.* **117**, 048102 (2016).
- [53] T. B. Saw, A. Doostmohammadi, V. Nier, L. Kocgozlu, S. Thampi, Y. Toyama, P. Marcq, C. T. Lim, J. M. Yeomans, and B. Ladoux, Topological defects in epithelia govern cell death and extrusion, *Nature (London)* **544**, 212 (2017).
- [54] K. Kawaguchi, R. Kageyama, and M. Sano, Topological defects control collective dynamics in neural progenitor cell cultures, *Nature (London)* **545**, 327 (2017).
- [55] K. Copenhagen, R. Alert, N. S. Wingreen, and J. W. Shaevitz, Topological defects promote layer formation in *Myxococcus xanthus* colonies, *Nat. Phys.* **17**, 211 (2021).
- [56] J. Roostalu, J. Rickman, C. Thomas, F. Nédélec, and T. Surrey, Determinants of polar versus nematic organization in networks of dynamic microtubules and mitotic motors, *Cell* **175**, 796 (2018).
- [57] E. Makhija, Y. Zheng, J. Wang, H. R. Leong, R. B. Othman, E. X. Ng, E. H. Lee, L. Tucker-Kellogg, Y. H. Lee, H. Yu *et al.*, Topological defects govern mesenchymal condensations, offering a morphology-based tool to predict cartilage differentiation, [bioRxiv 2022.05.30.493944](https://doi.org/10.1101/2022.05.30.493944), doi:10.1101/2022.05.30.493944.
- [58] A. Baskaran and M. C. Marchetti, Nonequilibrium statistical mechanics of self-propelled hard rods, *J. Stat. Mech.* (2010) P04019.
- [59] A. Patelli, I. Djafer-Cherif, I. S. Aranson, E. Bertin, and H. Chaté, Understanding Dense Active Nematics from Microscopic Models, *Phys. Rev. Lett.* **123**, 258001 (2019).



# Chapter 3

## Spatiotemporal transition in active nematic fluids

The foundation of this chapter rests entirely on [1] and seeks to investigate the presence of transitions or crossovers in active nematic fluids, extending beyond the well-established hydrodynamic instability of the ordered state [2, 3]. To facilitate this, an information-theoretic measure of spatiotemporal ordering of topological defects is utilized, grounded in the recently introduced concept of *computable information density* [4]. Understanding the evolution of active systems with varying levels of activity is of fundamental importance in a wide range of biological systems. The dynamics of topological defects are particularly important, as they are closely linked to the emergent flows in living materials [5, 6], and have been demonstrated to carry biochemical information on the membrane of living cells [7, 8] and enhance the topological mixing in filament-motor protein mixtures [9].

### 3.1 Nematohydrodynamic model

The continuum description of suspended active nematogens provides an effective coarse-grained representation, extending the Beris-Edwards equations [10] for passive nematic liquid crystal hydrodynamics. The governing equations for active nematohydrodynamic are extensively documented [11–13]. Relevant variables include the density  $\rho$ , the velocity field  $u_i$ , and the two-dimensional, traceless, and symmetric nematic order parameter  $Q_{ij} = 2S(n_i n_j - \delta_{ij}/2)$ . This second-rank tensor represents orientational order, with scalar order parameter  $S$  and director  $n_i$  denoting its largest eigenvalue and corresponding eigenvector, encoding magnitude and direction of nematic ordering, respectively. The governing dynamics consist of three coupled continuum equations describing incompressibility, momentum balance, and advection-diffusion of the nematic order-parameter field,

respectively:

$$\partial_i u_i = 0, \quad (3.1)$$

$$\rho(\partial_t + u_j \partial_j) u_i = \partial_j \Pi_{ij}, \quad (3.2)$$

$$(\partial_t + u_k \partial_k) Q_{ij} - S_{ij} = \Gamma H_{ij}. \quad (3.3)$$

The generalized advection term

$$\begin{aligned} S_{ij} = (\lambda E_{ik} + \Omega_{ik}) \left( Q_{kj} + \frac{1}{2} \delta_{kj} \right) + \left( Q_{ik} + \frac{1}{2} \delta_{ik} \right) (\lambda E_{kj} - \Omega_{kj}) \\ - 2\lambda \left( Q_{ij} + \frac{1}{2} \delta_{ij} \right) (Q_{kl} \partial_k u_l) \end{aligned} \quad (3.4)$$

is a co-rotational term, expressing the response of the nematic ordering to flow gradients (i.e. any shear flow will either turn or tumble the nematogens) described by the strain rate tensor  $E_{ij} = (\partial_i u_j + \partial_j u_i)/2$  and the vorticity tensor  $\Omega_{ij} = (\partial_i u_j - \partial_j u_i)/2$ . The alignment parameter  $\lambda$  determines whether strain or vorticity dominates the nematogens collective response to shear flow, with positive and negative values corresponding to rod-like and disk-like shapes, respectively. The molecular field

$$H_{ij} = -\frac{\delta F}{\delta Q_{ij}} + \frac{1}{2} \delta_{ij} \text{Tr} \left( \frac{\delta F}{\delta Q_{kl}} \right) \quad (3.5)$$

ensures diffuse relaxation of the nematic ordering to the free energy minimum

$$F = \int \left\{ K (\partial_k Q_{ij})^2 + \frac{\mathcal{A}}{2} (1 - Q_{ij} Q_{ji})^2 \right\} d^2 \mathbf{x} \quad (3.6)$$

on a timescale set by the rotational diffusive constant  $\Gamma$ ; with  $K$  being the Frank elastic constant and  $\mathcal{A}$  the energy constant associated with the Landau-de Gennes free energy. The stress tensor  $\Pi_{ij}$  consist of three parts; viscous stress  $\Pi_{ij}^{\text{viscous}} = 2\mu E_{ij}$ , elastic stress

$$\begin{aligned} \Pi_{ij}^{\text{elastic}} = -P \delta_{ij} + 2\lambda \left( Q_{ij} + \frac{1}{2} \delta_{ij} \right) Q_{kl} H_{lk} - \lambda H_{ik} \left( Q_{kj} + \frac{1}{2} \delta_{kj} \right) \\ - \lambda \left( Q_{ik} + \frac{1}{2} \delta_{ik} \right) H_{kj} - \partial_i Q_{kl} \frac{\delta F}{\delta \partial_j Q_{lk}} + Q_{ik} H_{kj} - H_{ik} Q_{kj}, \end{aligned} \quad (3.7)$$

and active stress  $\Pi_{ij}^{\text{active}} = -\zeta Q_{ij}$ . Here,  $P$  represents pressure, and  $\zeta$  dictates the strength and nature of activity, with positive and negative values characterizing extensile- and a contractile- nematogens, respectively. The elastic stress introduces back-flow, while the active stress implies that any gradients in the nematic ordering generate flows, rendering the nematic state unstable and ultimately leading to active turbulence [13–16].



### 3.1.1 Simulations and parameters

The governing equations (3.1 - 3) constitutes a coupled system, and are numerically integrated using a hybrid lattice-Boltzmann method [13, 17]. This approach combines the finite-difference method for the evolution of the nematic order parameter (3.3) with the lattice-Boltzmann method for solving the incompressible Navier-Stokes equations (3.2). Simulations were initiated with a quiescent velocity field and slightly perturbed nematic alignment close to the uniform nematic state with the nematic director aligned along the  $x$ -axis, on a periodic quadratic domain of linear dimension  $L = 1024$ . The system is evolved until a statistical steady state is reached. The lattice spacing and time step is taken as unity and the additional parameters are chosen so the resulting flow patterns reproduce that observed in flow-aligning and low Reynolds number experiments on microtubule–motor protein mixtures [11]

| rotational diffusion $\Gamma$ | elasticity $K$ | viscosity $\mu$ | density $\rho$ | alignment $\lambda$ | activity $\zeta$ |
|-------------------------------|----------------|-----------------|----------------|---------------------|------------------|
| 0.05                          | 0.05           | 1.0             | 40             | 1.0                 | 0.1              |

and the parameter  $\mathcal{A}$  in the Landau-de Gennes bulk free energy expansion are taken above the nematic-isotropic transition, so that any potential local nematic ordering solely is induced by the activity. All of the model parameters are reported in lattice units.

## 3.2 Spatiotemporal defect disorder

To quantify the chaotic dynamics following from the continuous proliferation and annihilation of defects in the steady state, we employ the recently introduced information-theoretic extensive measure of order for systems both in and out of equilibrium [4, 18]. This measure relies on a universal — does not necessitate prior knowledge of the system dynamics — lossless compression algorithm, specifically the Lempel-Ziv 77 (LZ77) compression algorithm [19]. In addition to being universal, the LZ77 algorithm has the advantage of being asymptotically optimal, in that the total binary code length  $\mathcal{L}(s)$  of the losslessly compressed data sequence  $s$  converges to the entropy in the thermodynamic limit for a stationary ergodic process [20]. This does not only make  $\mathcal{L}$  a good approximation for the equilibrium entropy when it is defined but also a suitable proxy thereof when undefinable, as in the case of systems far from equilibrium. The central idea behind this naïve quantitative measure is simple: data with a high-level of correlations, and thus order, are more compressible than data with either low- or no- level of correlations. Thus making  $\mathcal{L}$  a satisfying measure of what most intuitively would perceive as

complexity.  $\mathcal{L}$  has been demonstrated to reveal first and second order phase transitions in equilibrium as well as nonequilibrium systems; along with the position of the critical point, the exponent for the critical slowing down, and the correlation length [4, 21].

### 3.2.1 Lempel-Ziv 77 complexity

The LZ77 algorithm is relatively straightforward yet powerful. It achieves lossless compression by replacing repeated substrings with references to their occurrences elsewhere in the input data. This is best illustrated with an example. Consider the data string  $s = 010110011100111001$ . Reading left to right, the first character is 0. The string now becomes  $0 \cdot 10110011100111001$ , where the added dot signifies that 0 is the longest substring not previously encountered. The second character, 1, is also encountered for the first time, thus forming a substring not previously encountered. Consequently, the string now reads  $0 \cdot 1 \cdot 0110011100111001$ . The longest substring not yet encountered after the second character is 011, resulting in the string reading  $0 \cdot 1 \cdot 011 \cdot 0011100111001$ . By continuing this procedure, we derive the final sequence of steps:  $0 \cdot 1 \cdot 011 \cdot 00 \cdot 11100111001 \rightarrow 0 \cdot 1 \cdot 011 \cdot 00 \cdot 111 \cdot 00111001$ . The count of longest substrings not previously encountered is the LZ77 complexity of the data string  $s$ , which in this case is 6. Figure 3.1 depicts the flowchart of the program utilized for computing the LZ77 complexity in this study.

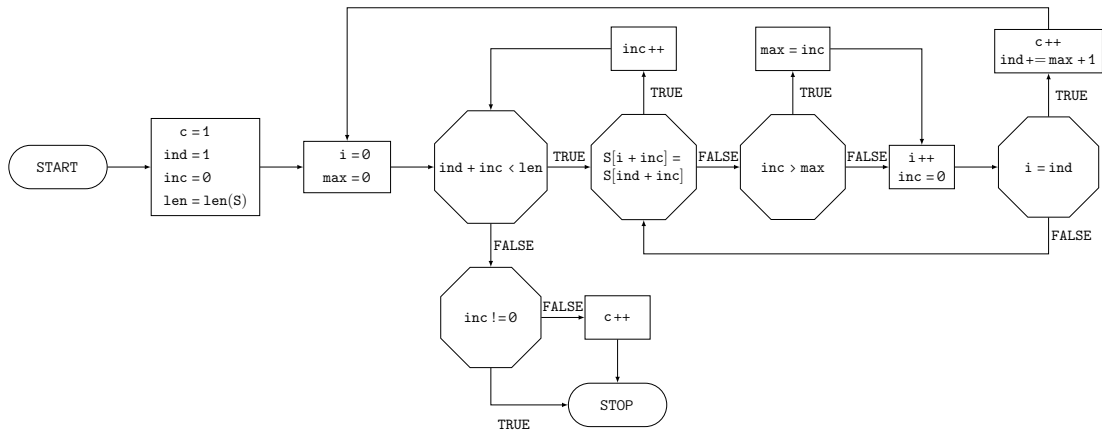


Figure 3.1: Flowchart depicting the program employed to compute the Lempel-Ziv 77 complexity  $c$  of a data string with a length of  $len$ .

### 3.2.2 Procedure for scanning three-dimensional spatiotemporal data

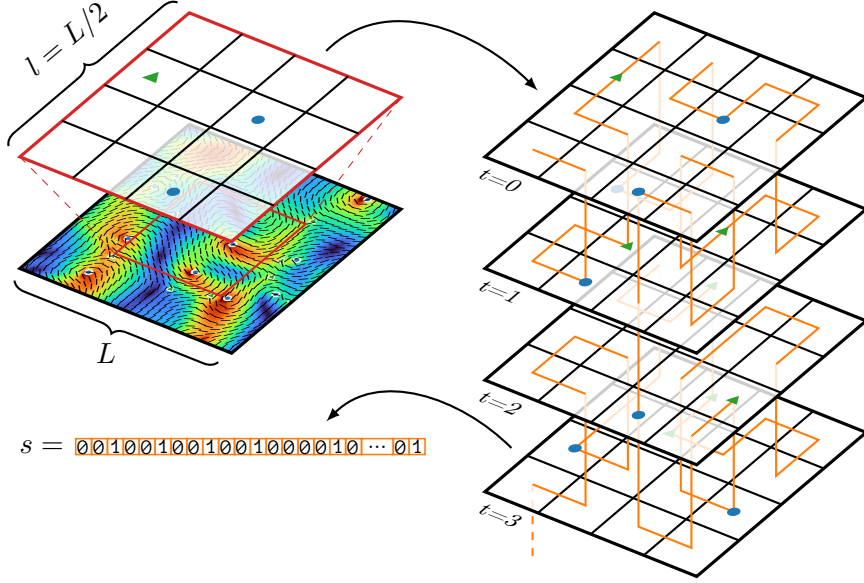


Figure 3.2: Procedure for constructing and flattening/scanning three-dimensional spatiotemporal defect position data.

Operating on one-dimensional strings of characters, the LZ77 compression scheme requires us to flatten our three-dimensional spatiotemporal data array to accommodate its application. Various procedures exist for imposing a partial linear ordering on higher-dimensional datasets, each method distinguished by its specific properties. This study uses a three-dimensional Peano-Hilbert ordering due to its locality-preserving behaviour [22, 23]; meaning that points that originally are spatiotemporally close remains relatively near to each other in the flattened array. There are a total of eight possible and distinct Peano-Hilbert orderings for our three-dimensional spatiotemporal data. This redundancy will come into play latter. The procedure unfolds as follows: Defect positions are extracted from the director field at every time-step and stacked chronologically to form a three-dimensional data grid, as shown in Fig. 3.2. In the depiction Fig. 3.2, blue circles depict  $+1/2$  defect and green triangles depict  $-1/2$  defect. Each grid point is labeled using a binary dictionary, where the presence of a defect is denoted by 1 and its absence by 0. We do not differentiate between  $\pm 1/2$  defects. The three-dimensional grid is flattened by imposing a linear partial ordering, here facilitated by the space filling Hilbert curve; depicted as the orange curve in Fig. 3.2. This Peano-Hilbert ordering  $s$  systematically covers the three-dimensional grid in

a self-similar manner while maintaining spatiotemporal locality. To mitigate the issue posed by defects situated close to each other in the vicinity of the periodic boundary, from becoming substantially separated in the one-dimensional Hilbert ordering  $s$ , a centered and quadratic observation window of linear size  $l = L/2$  is chosen. Only defects falling within this window are considered. This window is depicted by the red square in Fig. 3.2.

### 3.3 Results

Examining how defect density  $\eta$  varies with active stress  $\zeta$ . Topological defects begin to emerge above a specific activity threshold, indicated by (I) in figure 3.3. Below this threshold, elastic energy accumulates along system spanning kink lines (Fig. 3.3a), created by the hydrodynamic instability [2]. The director field experiences significant bending deformations, generating active stresses as a result. These stresses, however, are initially too weak to exacerbate the bend instabilities, thus maintaining the dynamic stability of the kink lines and preventing the formation of topological defects. As active stress increases, it eventually causes the kink lines to break up, leading to the formation of topological defects (Fig. 3.3b-c). This breakup is followed by a rapid rise in defect density as activity levels continue to increase.

#### 3.3.1 Divergence measure

To quantify the information excess present in the measured spatiotemporal distribution of defects relative to a random uniform distribution of the same defects, a *divergence* measure is introduced [24]. This measure serves as a mathematical tool to gauge the deviation from randomness and provides insights into the underlying patterns or structures within the distribution.

$$\mathcal{D}(s) = \left\langle 1 - \frac{\mathcal{L}(s)}{\mathbb{E}[\mathcal{L}(s_{\text{sh}})]} \right\rangle, \quad (3.8)$$

where  $\mathcal{L}(s_{\text{sh}})$  is the  $\mathcal{L}$ -measure of a random shuffle of the data sequence  $s$ , and  $\mathbb{E}[\mathcal{L}(s_{\text{sh}})]$  is the sample average over several such shuffles. To ensure robustness in our analysis and mitigate unintentional biases stemming from the choice of the Peano-Hilbert ordering, an average  $\langle \cdot \rangle$  across all eight such possible orderings is computed.

#### Defect proliferation threshold

Examining figure 3.3d reveals that the threshold activity for defect proliferation is accurately captured by the abrupt change and subsequent rapid increase in the

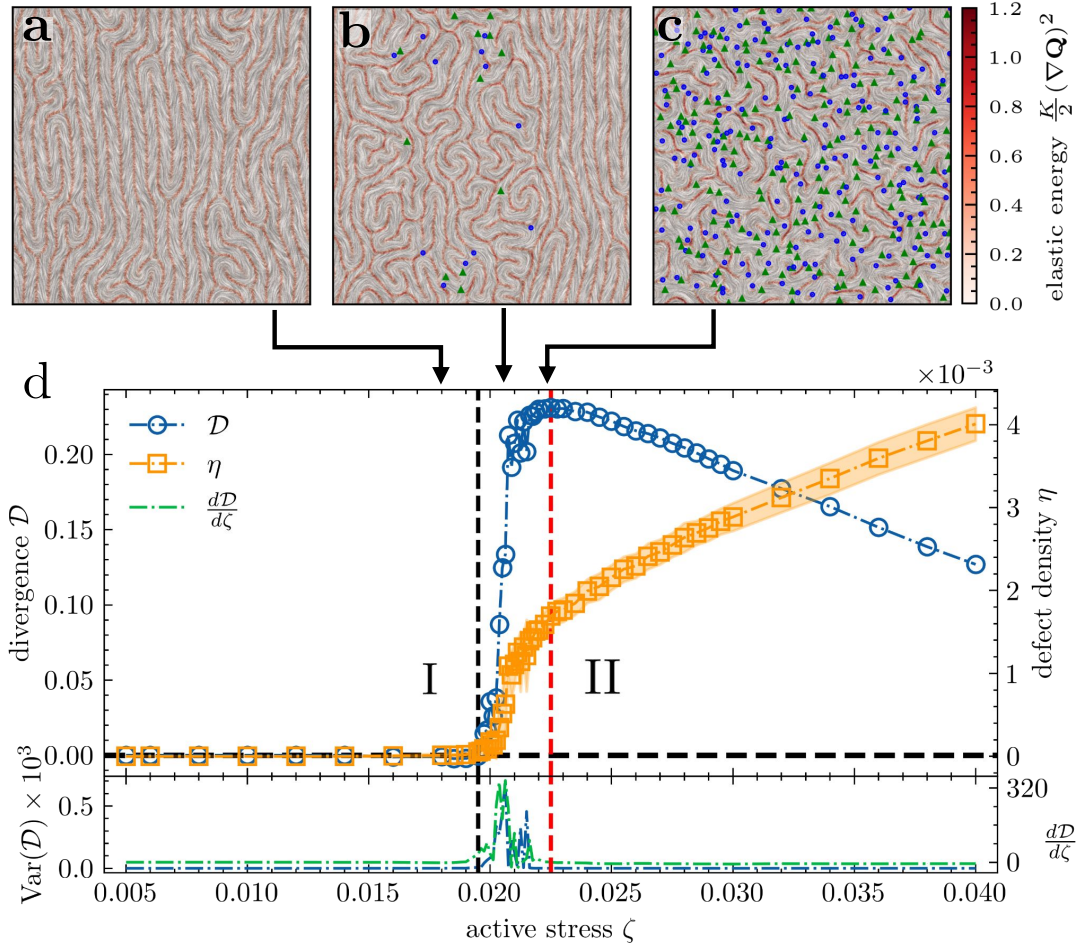


Figure 3.3: (a-c) Snapshots showing the director field and elastic energy at three stages: before, at, and after the defect nucleation threshold. The corresponding active stresses are (a)  $\zeta = 0.018$ , (b)  $\zeta = 0.0205$ , and (c)  $\zeta = 0.022$ . Topological defects are indicated by blue circles (+1/2 defect) and green triangles (-1/2 defect). (d) Divergence measure and defect density plotted against the active stress. Both ordinates are aligned at zero, as highlighted by the horizontal dashed black line. The vertical dashed black line (I) indicates the onset of defect proliferation, while the vertical dashed red line (II) marks the maximum in the divergence measure. The lower panel displays the peaks in both the variance and gradient of the divergence as functions of active stress.

$\mathcal{D}$ -measure (3.8), before reaching its maximum. In this range defined by the activity threshold (indicated by I) and the maximum (indicated by II) the system undergoes a transient state from defect-absent to defect-laden active turbulence,

dominated by rare events. Indeed, figure 3.3b reveals that within this activity range defects tend to form and congregate in the vicinity of other defects. This clustering behavior suggests a strong correlation between defect activity and their spatiotemporal distribution, highlighting the critical nature of the threshold in transitioning the system to a state characterized by active turbulence. This transient state is further elucidated by examining the gradient  $d\mathcal{D}/d\zeta$  (bottom panel in Fig. 3.3d). Remarkable, the fluctuations in  $\mathcal{D}$  and its peak coalesce with the gradient, indicative of an approximate proportionality between  $d\mathcal{D}/d\zeta$  and  $\text{Var}(\mathcal{D})$ . This relationship mirrors an analog of the fluctuation–dissipation theorem from equilibrium statistical mechanics. The coherence between  $\mathcal{D}$ 's fluctuations and its gradient suggests a dynamic balance akin to that seen in equilibrium systems, where fluctuations and dissipation are intimately linked. This finding underscores the intricate interplay between system dynamics and the emergence of defects, shedding light on the underlying mechanisms driving the transition to defect-laden active turbulence.

### 3.3.2 Director decorrelation time

Topological defects represent spatial locations where the nematic order breaks down, identified by the minima in the largest eigenvalue  $S$  of the nematic order parameter  $Q_{ij}$ . Upon examining figure 3.4a, it is evident that the excess order in the scalar order parameter  $S$  spikes at the activity level where a peak in the fluctuations of the divergence measure was previously observed. This correlation indicates a significant change in the director dynamics coinciding with defect nucleation. The spike in  $S$  suggests that the system's order parameter becomes highly responsive at the threshold of defect proliferation, further emphasizing the critical nature of this activity level in the transition to defect-laden active turbulence.

To shed further light on the temporal features of the director dynamics during defect nucleation events, the decorrelation time in the order parameter  $S$  was calculated by fitting an exponential decay to the temporal autocorrelation of the fluctuations in  $S$  and subsequently averaging this space. This analysis aims to provide deeper insights into how quickly the system's order parameter responds and evolves during the critical phase of defect proliferation, offering a more detailed understanding of the dynamic processes underpinning the transition to defect-laden active turbulence. Figure 3.4b reveals a significant slowing in the director fluctuations prior to the onset of defect proliferation. The introduction of defects swiftly alters the characteristic timescale for fluctuations, as evidenced by a sharp decrease in the decorrelation time by more than an order of magnitude within the previously defined transition range, consistent with the observations in figure 3.3d. However, at higher levels of activity, the decorrelation time shows only a moderate decrease with increasing activity.

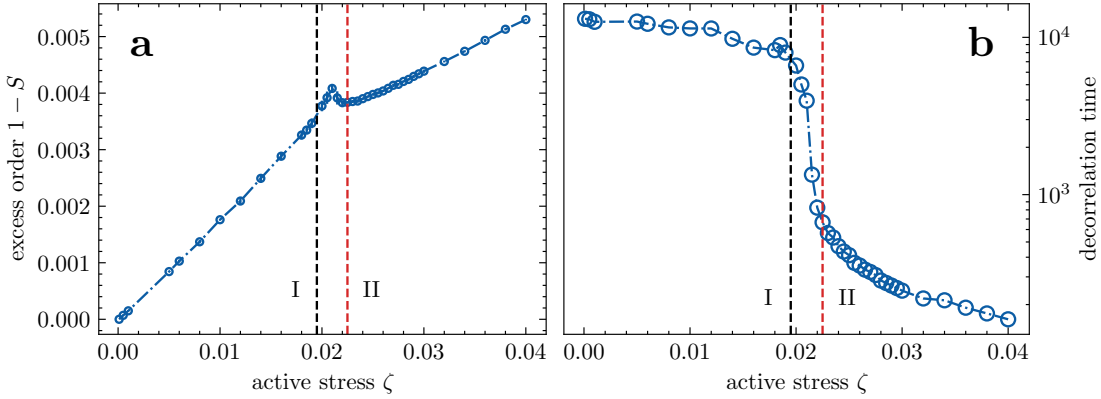


Figure 3.4: (a) Excess order as function of activity. The spike coalesce with the peak in the  $\mathcal{D}$ -measure fluctuations. (b) Director decorrelation time vs. active stress. The abrupt drop of the director decorrelation time, a space-averaged and temporal measure, only picks up the first transition. The transition points labeled (I) and (II) correspond to those in figure 3.3d.

### 3.3.3 Defect pathlength

The defect pathlength measures the average distance defects travel over time, normalized by the average distance between defects. The first transition point (I) in figure 3.5 corresponds to the onset of defect nucleation, where non-linearities in defect dynamics become apparent. At this stage, defects begin to form and proliferate due to increased active stress, leading to a noticeable change in the system's behavior. However, it is the second transition point (II) that reveals more intricate dynamics. Here, the defect pathlength reaches its peak, indicating an optimal state for defect motion and organization. This peak represents the maximum pathlength before the system transitions into a state dominated by strong interactions, characterized by more frequent annihilation events among defects, and shorter individual defect paths despite the increasing defect density.

## 3.4 Conclusion

The findings reveal a sequence of transitions in the evolution of collective self-organization patterns with increasing activity of the material. Beyond the known hydrodynamic instability of the ordered state [3, 14], a first activity threshold was identified, initiating the nucleation of topological defects. At this threshold, the director decorrelation time drops sharply, indicating a rapid increase in temporal fluctuations. Further investigation uncovered a hidden dynamic transition beyond this threshold, characterized by optimal spatial and temporal organization

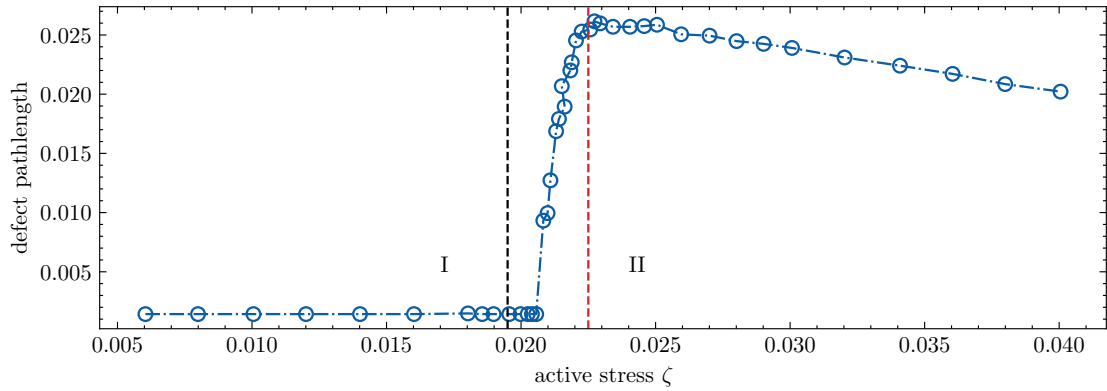


Figure 3.5: Defect pathlength, normalized by the average defect separation distance. Transition points labeled (I) and (II) correspond to those in figure 3.3d.

of topological defects. This spatiotemporal transition is not apparent through purely spatial or temporal analyses alone. The existence of such a threshold for spatiotemporal organization could have significant implications for the evolution of self-organization patterns in living materials [25–27]. This research highlights the need to explore order parameters that evolve in both space and time to uncover phase transitions in non-equilibrium systems.



## Bibliography

- [1] Robin V. Bølsterli, Benjamin H. Andersen, and Amin Doostmohammadi. Fully developed active turbulence: Emergence of hidden spatiotemporal transition in active nematic fluids. 2024.
- [2] R. Aditi Simha and Sriram Ramaswamy. Hydrodynamic fluctuations and instabilities in ordered suspensions of self-propelled particles. *Phys. Rev. Lett.*, 89:058101, Jul 2002.
- [3] Berta Martínez-Prat, Jordi Ignés-Mullol, Jaume Casademunt, and Francesc Sagués. Selection mechanism at the onset of active turbulence. *Nature physics*, 15(4):362–366, 2019.
- [4] Stefano Martiniani, Paul M. Chaikin, and Dov Levine. Quantifying hidden order out of equilibrium. *Phys. Rev. X*, 9:011031, Feb 2019.
- [5] Sumesh P Thampi, Ramin Golestanian, and Julia M Yeomans. Velocity correlations in an active nematic. *Physical review letters*, 111(11):118101, 2013.
- [6] Luca Giomi, Mark J Bowick, Xu Ma, and M Cristina Marchetti. Defect annihilation and proliferation in active nematics. *Physical Review Letters*, 110(22):228101, 2013.
- [7] Tzer Han Tan, Jinghui Liu, Pearson W Miller, Melis Tekant, Jörn Dunkel, and Nikta Fakhri. Topological turbulence in the membrane of a living cell. *Nature Physics*, 16(6):657–662, 2020.
- [8] Jinghui Liu, Jan F Tetz, Pearson W Miller, Alasdair D Hastewell, Yu-Chen Chao, Jörn Dunkel, and Nikta Fakhri. Topological braiding and virtual particles on the cell membrane. *Proceedings of the National Academy of Sciences*, 118(34):e2104191118, 2021.
- [9] Amanda J Tan, Eric Roberts, Spencer A Smith, Ulyses Alvarado Olvera, Jorge Arteaga, Sam Fortini, Kevin A Mitchell, and Linda S Hirst. Topological chaos in active nematics. *Nature Physics*, 15(10):1033–1039, 2019.
- [10] Antony N. Beris and Brian J. Edwards. *Thermodynamics of flowing systems: with internal microstructure*. Number 36. Oxford University Press, USA, 1994.
- [11] Amin Doostmohammadi, Jordi Ignés-Mullol, Julia M Yeomans, and Francesc Sagués. Active nematics. *Nature communications*, 9(1):3246, 2018.

- [12] Thuan Beng Saw, Amin Doostmohammadi, Vincent Nier, Leyla Kocgozlu, Sumesh Thampi, Yusuke Toyama, Philippe Marcq, Chwee Teck Lim, Julia M Yeomans, and Benoit Ladoux. Topological defects in epithelia govern cell death and extrusion. *Nature*, 544(7649):212–216, 2017.
- [13] Sumesh P Thampi, Ramin Golestanian, and Julia M Yeomans. Vorticity, defects and correlations in active turbulence. *Philosophical Transactions of the Royal Society A: Mathematical, Physical and Engineering Sciences*, 372(2029):20130366, 2014.
- [14] R. Aditi Simha and Sriram Ramaswamy. Hydrodynamic fluctuations and instabilities in ordered suspensions of self-propelled particles. *Physical Review Letters*, 89:058101, Jul 2002.
- [15] Sriram Ramaswamy. The mechanics and statistics of active matter. *Annual Review Condensed Matter Physics*, 1(1):323–345, 2010.
- [16] M. C. Marchetti, J. F. Joanny, S. Ramaswamy, T. B. Liverpool, J. Prost, Madan Rao, and R. Aditi Simha. Hydrodynamics of soft active matter. *Rev. Mod. Phys.*, 85:1143–1189, Jul 2013.
- [17] D Marenduzzo, Enzo Orlandini, ME Cates, and JM Yeomans. Steady-state hydrodynamic instabilities of active liquid crystals: Hybrid lattice boltzmann simulations. *Physical Review E*, 76(3):031921, 2007.
- [18] Milan Rajković and Zoran Mihailović. Quantifying complexity in the minority game. *Physica A: Statistical Mechanics and its Applications*, 325(1-2):40–47, 2003.
- [19] Jacob Ziv and Abraham Lempel. A universal algorithm for sequential data compression. *IEEE Transactions on information theory*, 23(3):337–343, 1977.
- [20] Thomas M. Cover. *Elements of information theory*. John Wiley & Sons, 1999.
- [21] Stefano Martiniani, Yuval Lemberg, Paul M. Chaikin, and Dov Levine. Correlation lengths in the language of computable information. *Phys. Rev. Lett.*, 125:170601, Oct 2020.
- [22] Michael S Warren and John K Salmon. A parallel hashed oct-tree n-body algorithm. pages 12–21, 1993.
- [23] Michael Bader. *Space-filling curves: an introduction with applications in scientific computing*, volume 9. Springer Science & Business Media, 2012.

- [24] A. Cavagna, P. M. Chaikin, D. Levine, S. Martiniani, A. Puglisi, and M. Viale. Vicsek model by time-interlaced compression: A dynamical computable information density. *Phys. Rev. E*, 103:062141, Jun 2021.
- [25] Henning Reinken, Sabine H. L. Klapp, and Michael Wilczek. Optimal turbulent transport in microswimmer suspensions. *Physical Review Fluids*, 7(8), August 2022.
- [26] Fereshteh L Memarian, Derek Hammar, Md Mainul Hasan Sabbir, Mark Elias, Kevin A Mitchell, and Linda Hirst. Controlling chaos: Periodic defect braiding in active nematics confined to a cardioid. *arXiv preprint arXiv:2401.04363*, 2024.
- [27] Rainer Backofen, Abdelrahman YA Altawil, Marco Salvalaglio, and Axel Voigt. Nonequilibrium hyperuniform states in active turbulence. *arXiv preprint arXiv:2311.14959*, 2023.

## Manuscript

TITLE: Fully developed active turbulence: Emergence of hidden spatiotemporal transition in active nematic fluids

AUTHORS: Robin V. Bølsterli<sup>†</sup>, Benjamin H. Andersen<sup>†</sup>, and Amin Doostmohammadi

Niels Bohr Institute, University of Copenhagen, Blegdamsvej 17, Copenhagen, Denmark.

<sup>†</sup> These authors contributed equally to this work.

MY CONTRIBUTION: Assisted in the development of the computational framework, conducting simulations, generating figures, and drafting the manuscript.

PUBLICATION STATUS: In preparation for submission.

# Fully developed active turbulence: Emergence of hidden spatiotemporal transition in active nematic fluids

Robin V. Bølsterli<sup>†</sup>, Benjamin H. Andersen<sup>†</sup>, and Amin Doostmohammadi<sup>\*</sup>  
*Niels Bohr Institute, University of Copenhagen, Blegdamsvej 17, Copenhagen, Denmark*  
(Dated: May 28, 2024)

In living materials, collective motion often manifests as flow vortices and jets, forming what is known as active turbulence. Using a continuum theory of active nematics and employing an information-theoretic *divergence* measure, we report on the existence of a nonlinear transition in active nematic fluid with increasing activity levels. Specifically, beyond the threshold activity for topological defects nucleation, we find a second activity threshold for a hidden dynamic transition to a state we term *fully-developed active turbulence*, and show that this transition is of spatiotemporal nature – remains concealed to purely spatial or purely temporal order parameters. We further show that the transition point marks the maximum pathlength for active topological defects and saturation of the scaled flow mixing rate. The results offer new insights into characterizing non-equilibrium phase transitions and the optimal evolution of active materials across varying activity levels.

Topological defects mark singularities in the order parameter, where the order breaks down, and are ubiquitous in a wide range of systems, from vortex and antivortex pairs in quantum fluids [1] to disclination lines in liquid crystals [2]. Since they are topologically-protected, such defects are robust to structural changes and are fundamental to structural properties of the material [3, 4]. In addition to their classical characterization in inanimate condensed matter systems [5, 6], there is now a growing list of biological processes in which topological defects are identified as the center of organization and hotspots for the localization of biochemical and mechanical information [7]. Striking examples are topological defects in the phase field of bioelectrical signaling in the heart and brain that are linked to arrhythmia [8, 9], topological defects in subcellular filaments as organization centers of morphogenesis in the Hydra genus [10], and topological defects in bacterial biofilm and tissue alignment fields as hotspots for bacteria and cell accumulation [11, 12], escape to the third dimension [12–14], and cell death and extrusion [15]. The common feature of all these biological implications is that, unlike their inanimate counterparts, topological defects in living materials are continuously created and annihilated in pairs due to the continuous injection of energy by the constituent elements of matter [16, 17]. This activity of living materials is shown to result in the self-propulsion of certain topological defects in filament-motor protein mixtures [18–20], in bacterial suspensions [11, 13], and in cellular tissues [12, 15], systems that are characterized as realizations of active liquid crystals [21–23].

The motion of active topological defects is shown to be closely interlinked with the emergent flows in living materials [24–27], and topological defects organization is often interleaved with fluid flow vortices and jets, forming a state called mesoscale- or active-turbulence [28–

30]. The active turbulent state arises due to an inherent hydrodynamic instability of the active nematic fluid [31, 32]: active stresses induce deformations in the orientational arrangement of the particles, which manifests as the formation of bend-splay walls. The walls then get unzipped by topological defects, initiating a cascade of fluid stirring that culminates in the emergence of seemingly chaotic flow vortices and jets in active turbulence [19, 33]. While the hydrodynamic instability that leads to the initiation of deformations is well-established, and in unbound systems is expected to occur for any finite activity level, the existence of additional phase transitions or nonlinear cross-overs at higher activity levels remains obscure.

In this Letter, we uncover a hidden transition in active nematics by employing the recently introduced information-theoretic divergence measure of spatiotemporal ordering based on the concept of *computable information density* (CID) [34–37]. The divergence measure quantifies organizational order in the turbulent regime of active nematics, a chaotic, highly non-equilibrium process. Remarkably, we show that not only the hidden transition marks the optimal defect pathlength, but also coincides with a change of scaling in the mixing rate, and therefore describes a change in the global flow features of the system. Importantly, we show that the hidden transition is of spatiotemporal nature, and as such will remain hidden to purely spatial or purely temporal characterizations of the system. Furthermore, we show that this hidden transition is distinct from, and occurs at higher activity levels well beyond the activity threshold for defect nucleation. Our findings uncover a new, hitherto hidden, spatiotemporal phase transition in active nematics, which could be of potential relevance to a range of dense active systems which manifest active turbulence.

We employ a two-dimensional continuum nematohydrodynamic model [38, 39] as a coarse-grained description of ordered suspension of active particles [24, 40–42]. This continuum description extends the Beris-Edwards equations [43] originally formulated for passive liquid

---

\* Correspondence email address: doostmohammadi@nbi.ku.dk

<sup>†</sup> These authors contributed equally to this work.

crystal hydrodynamics. The dynamics of the nematic order parameter  $\mathbf{Q}$  and velocity field  $\mathbf{u}$  evolve according to

$$\partial_t \mathbf{Q} + (\mathbf{u} \cdot \nabla) \mathbf{Q} - \mathbf{S} = \Gamma \mathbf{H}, \quad (1a)$$

$$\partial_t \mathbf{u} + (\mathbf{u} \cdot \nabla) \mathbf{u} = \frac{1}{\rho} \nabla \cdot \mathbf{\Pi}, \quad (1b)$$

along with the incompressibility condition  $\nabla \cdot \mathbf{u} = 0$ . The molecular field  $\mathbf{H} = -\frac{\delta F}{\delta \mathbf{Q}} + \frac{1}{2} \text{Tr} \left( \frac{\delta F}{\delta \mathbf{Q}} \right)$  governs the diffusive relaxation of nematic ordering towards the minimum of the free energy  $F = \int \mathcal{A} \left( 1 - \frac{1}{2} \mathbf{Q}^2 \right)^2 + \frac{K}{2} (\nabla \mathbf{Q})^2 d^2 \mathbf{x}$ , operating on a timescale dictated by the diffusive constant  $\Gamma$ . Here,  $\mathcal{A}$  represents the constant associated with the Landau-de Gennes free energy, and  $K$  is the orientational elasticity, assuming a single Frank elastic constant. The co-rotational term  $\mathbf{S} = (\lambda \mathbf{E} + \mathbf{\Omega}) \cdot (\mathbf{Q} + \frac{1}{2}) + (\mathbf{Q} + \frac{1}{2}) \cdot (\lambda \mathbf{E} - \mathbf{\Omega}) - 2\lambda (\mathbf{Q} + \frac{1}{2}) (\mathbf{Q} : \nabla \mathbf{u})$  in (1a) describes the response of the nematic ordering to gradients in the flow field, which include the strain rate  $\mathbf{E}$  and vorticity  $\mathbf{\Omega}$  tensors representing the symmetric and antisymmetric part of the flow gradient  $\nabla \mathbf{u}$ , respectively. Their comparative influence in affecting the alignment of nematogens with flow is characterized by the tumbling parameter  $\lambda$ . The stress tensor  $\mathbf{\Pi}$  in (1b) comprises three parts; viscous stress  $\mathbf{\Pi}^{\text{viscous}} = 2\mu \mathbf{E}$ , elastic stress  $\mathbf{\Pi}^{\text{elastic}} = -P \mathbf{I} + 2\lambda (\mathbf{Q} + \frac{1}{2}) (\mathbf{Q} : \mathbf{H}) - \lambda \mathbf{H} \cdot (\mathbf{Q} + \frac{1}{2}) - \lambda (\mathbf{Q} + \frac{1}{2}) \cdot \mathbf{H} - \nabla \mathbf{Q} \left( \frac{\delta F}{\delta \nabla \mathbf{Q}} \right) + \mathbf{Q} \cdot \mathbf{H} - \mathbf{H} \cdot \mathbf{Q}$ , and active stress  $\mathbf{\Pi}^{\text{active}} = -\zeta \mathbf{Q}$ . Here,  $P$  is the pressure field and  $\zeta$  is setting the strength of the activity. The active stress  $\zeta$  is reported in units of the Landau-de Gennes free energy constant  $\mathcal{A}$ , namely the non-dimensionalized active stress  $\tilde{\zeta}$ . Elastic stress induces backflow, and has been numerically and experimentally shown to be relevant to  $\pm 1/2$  defect annihilation dynamics in passive nematics [25, 44, 45]. Meanwhile, active stress causes gradients in nematic ordering to generate flows, destabilizing the nematic state and ultimately leading to active turbulence [16, 21, 31, 33]. We ensure to choose appropriate simulation parameters such that we are in the flow-aligning regime and at low Reynolds number,  $\text{Re} \ll 1$  (see SI for the details of the simulations and parameters).

We begin with examining the defect density  $\eta$  as a function of activity (Fig. 1). Above an activity threshold, topological defects emerge. This is then followed by a steep increase in defect density with increasing activity levels. A close inspection of the temporal evolution of the system [46] indicates a significant change in the director dynamics upon defect nucleation. To characterize this temporal feature, we calculate the director decorrelation time  $\tau_d$ , determined by fitting an exponential decay to the temporal autocorrelation of the fluctuations in the scalar order parameter  $S$  and subsequently averaging over space. We scale the director decorrelation time by the active timescale  $\tau_a = \frac{\mu}{\zeta}$  to obtain the scaled decorrelation time  $\tilde{\tau}_d$ . This quantity clearly shows the

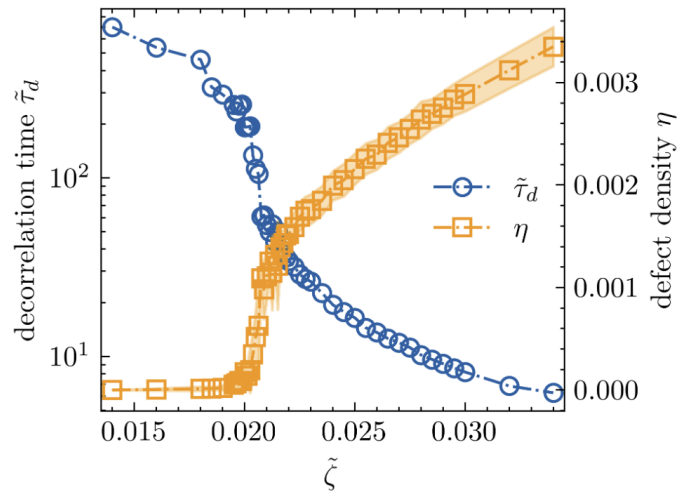


Figure 1. **Director decorrelation time and defect density.** Director decorrelation time  $\tilde{\tau}_d$  as a function of active stress  $\tilde{\zeta}$ . The abrupt drop of the director decorrelation time, a space-averaged and temporal measure, picks up the defect nucleation threshold.

reorganization of the director configuration upon defect nucleation, in time, opposed to the usually considered spatial correlations. Interestingly, we find a sharp drop in the decorrelation time  $\tilde{\tau}_d$  of the director field exactly at the activity threshold for defect nucleation. As such, across a narrow range of activities, the fluctuations in the director field rapidly increase.

To delve deeper into the crossover from a defect-free to a defect-laden state, we proceed to quantify the divergence measure, which is a recently introduced information-theoretic measure of order for systems both in and out of equilibrium [34]. This measure rests on the Lempel-Ziv 77 (LZ77) compression algorithm [47]. In addition to being universal, the LZ77 algorithm has the advantage of being asymptotically optimal, in that the total binary code length  $\mathcal{L}(s)$  of the losslessly compressed data sequence  $s$  converges to the entropy in the thermodynamic limit for a stationary ergodic process [48]. This does not only make  $\mathcal{L}$  a good approximation for the equilibrium entropy when it is defined, but also a suitable proxy thereof when undefinable, as in the case of systems far from equilibrium. The central idea behind this quantitative measure is simple: data with a high-level of correlations, and thus order, are more compressible than data with either low- or no- level of correlations. Thus making  $\mathcal{L}$  a satisfying measure of what most intuitively would perceive as complexity.

The LZ77 compression scheme, operating on one-dimensional strings of characters, requires us to flatten our three-dimensional spatiotemporal data array to accommodate its application. We employ a three-dimensional Peano-Hilbert ordering (depicted as the orange curve in Fig. 2) due to its locality-preserving behavior [49]; this means that in the flattened array, points

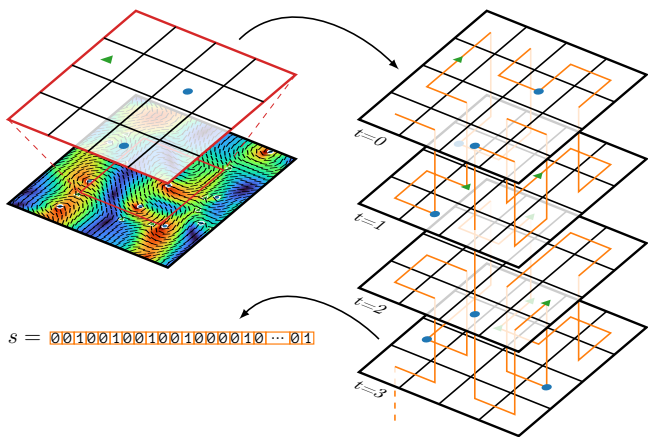


Figure 2. **Procedure for flattening three-dimensional spatiotemporal data.** Defect positions are extracted from the director field and stacked chronologically to form a three-dimensional data grid. Blue circles depict  $+1/2$  defects and green triangles depict  $-1/2$  defects. A grid point is labeled using a binary dictionary; here we have used 1 to label the presence of a defect and 0 for the absence thereof. The three-dimensional grid is flattened/scanned by imposing a linear partial ordering, here provided by the space-filling Hilbert curve (orange curve). This Peano-Hilbert ordering  $s$  covers the three-dimensional grid in a self-similar fashion while preserving locality.

that were originally close together in terms of space and time will still be positioned relatively close to each other.

Defect positions are extracted from the director field at each time step and stacked chronologically to form a three-dimensional array (representing two-dimensional space plus one dimension for time), as shown in Fig. 2. In this array, the entries are designated with a value of 1 to indicate the presence of a defect, while the entries labeled 0 denote the absence of a defect. Finally, to quantify the information excess in the observed spatiotemporal distribution of defects relative to that of a random uniform distribution of the same defects, we introduce the *divergence* measure defined by [36]

$$\mathcal{D}(s) = \left\langle 1 - \frac{\mathcal{L}(s)}{\mathbb{E}[\mathcal{L}(s_{\text{sh}})]} \right\rangle, \quad (2)$$

where  $\mathcal{L}(s_{\text{sh}})$  is the  $\mathcal{L}$ -measure of a random shuffle of the data sequence  $s$ , and  $\mathbb{E}[\mathcal{L}(s_{\text{sh}})]$  is the sample average over several such shuffles. This divergence measure has been demonstrated to reveal first and second order phase transitions in equilibrium as well as non-equilibrium systems, such as in the Vicsek model and in motility-induced phase separation, along with the position of the critical point, the exponent of the critical slowing down, and the correlation length [34–36].

The threshold activity for defect proliferation is accurately captured by the abrupt increase in the  $\mathcal{D}$ -measure (Fig. 3). This rapid variation in  $\mathcal{D}$  in the vicinity of the threshold activity is made more explicit by studying

the gradient  $d\mathcal{D}/d\zeta$ . In particular, the threshold activity and the corresponding local maximum define a range at  $\zeta = 0.0195$  and at  $\zeta = 0.0225$  in Fig. 3), in which the system undergoes a transient state from defect-less active turbulence to defect-laden active turbulence and is dominated by rare events. Indeed, within this activity range defects tend to form and congregate in the vicinity of other defects (see Supplementary Videos [46]). We note in passing that the fluctuations in the divergence measure  $\mathcal{D}$  and its peak coalesce with the gradient, i.e.  $d\mathcal{D}/d\zeta \approx \text{Var}(\mathcal{D})$ , thereby mirroring an analog of the fluctuation–dissipation theorem from equilibrium statistical mechanics.

Beyond the activity threshold for defect nucleation, which additionally marks the abrupt drop of the director decorrelation, the divergence measure reveals the existence of a spatiotemporal transition. This transition is marked by a peak in the divergence measure, and occurs at a higher activity compared to the defect nucleation threshold. The peak in the divergence measure indicates that this second activity threshold characterizes the emergence of states where the defects have self-organized into a spatiotemporal ordered state relative to the uniformly random state at higher activity levels. Importantly, this peak disappears when repeating the divergence measure with purely spatial (time-averaged) or purely temporal (space-averaged) defect positions, indicating that this second activity threshold is related to a change in a truly spatiotemporal feature of the system. Thus, the divergence measure (Eq. 2) signals a dynamic transition at finite activity levels. However, the divergence measure does not provide insights into the relevant order parameter undergoing the transition. Therefore, our focus shifts to examining spatiotemporal features of the system around the activity level that is picked up by the maximum of the divergence measure.

Qualitatively observing the defect dynamics after the transition point, defects start to increasingly interact with each other, leading to more annihilation events and thereby shortening of the pathlength for an increasing number of defects in the system [46]. Interestingly, the measured defect pathlength  $l_d$  (scaled with the average distance between the defects, Fig. 4) peaks at the transition point. Despite ever increasing defect density, the pathlengths of individual defects become shorter beyond the observed spatiotemporal transition.

The stirring of topological defects, especially due to the self-propelled  $+1/2$  defects, is linked closely to a very efficient mixing protocol [26, 50, 51]. Therefore, we hypothesize a clear signature in the flow mixing rate at the transition point, together with the observed optimal defect pathlength. To quantify the mixing exerted by the flow, we introduce a scalar tracer field, which evolves with the advection-diffusion equation. The degree of mixing as a function of time is then quantified according to the

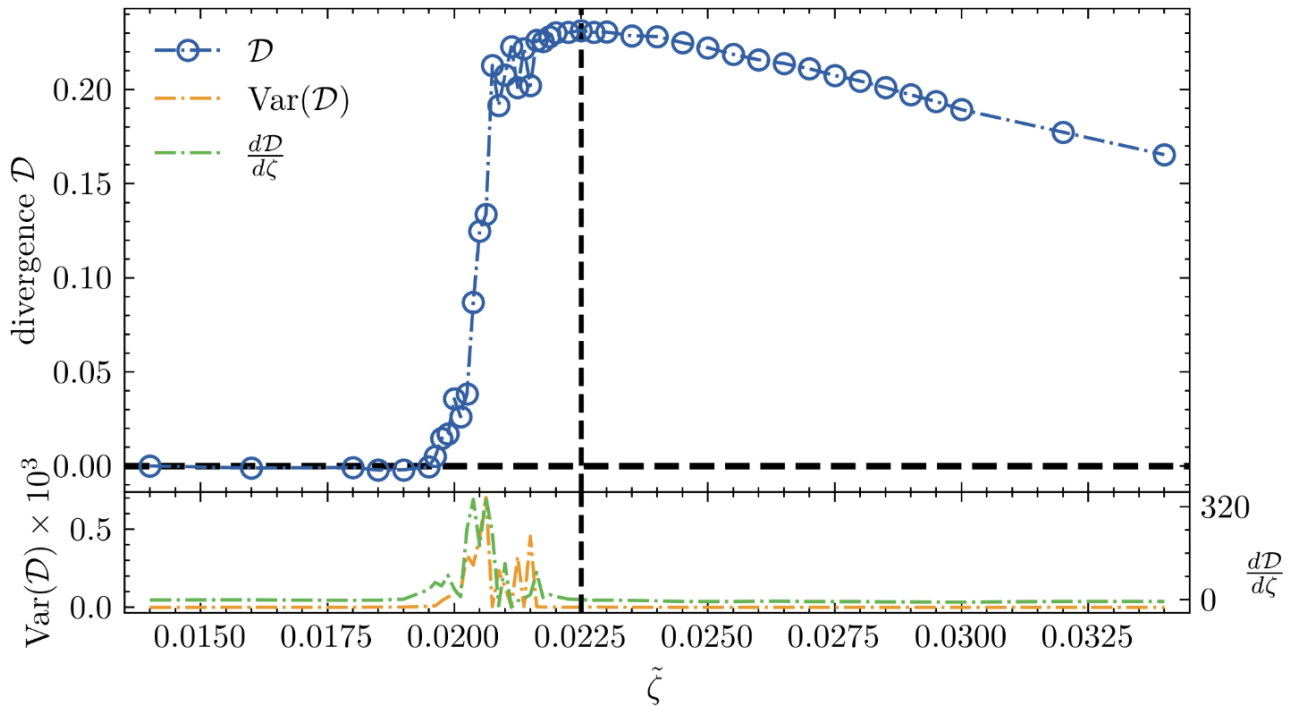


Figure 3. **Spatiotemporal defect disorder.** The dependence of the divergence measure on the dimensionless active stress  $\tilde{\zeta}$ . Both ordinates are aligned at zero as highlighted by the horizontal dashed black line. The vertical dashed black line marks the maximum in the divergence measure. The lower panel shows the peak in both variance and gradient of divergence vs. active stress.

$H^{-1}$  mixing norm [52],

$$\|(c(\cdot, t))\|_{H^{-1}}^2 = \sum_{\mathbf{k} \neq 0} \frac{|c_{\mathbf{k}}|^2}{|\mathbf{k}|^2} \quad (3)$$

where the  $c_{\mathbf{k}}$  are the coefficients of the Fourier-transformed tracer field. The mixing norm is normalized to the value in the initial configuration and fitted to an exponential function  $\sim \exp^{-\nu t}$  to determine the mixing rate  $\nu$  [26].

Interestingly, despite no qualitative change in the flow structure is observed before or after the transition (Fig. 4a, b), the mixing rate shows a clear signature of the transition (Fig. 4c). This is best demonstrated by scaling the mixing rate with the active timescale  $\tau_a = \frac{\mu}{\zeta}$ , obtaining the scaled mixing rate  $\tilde{\nu}$ . At the defect nucleation threshold, non-linearities in the dependence from the active stress appear. Remarkably, these non-linearities then disappear exactly at the transition point. This observation is noteworthy because, unlike the divergence measure and the defect pathlength, which characterize only topological defects dynamics, the mixing rate is a global feature of the system, which characterizes the spatiotemporal features of the fluid flow. As such, there exists an activity threshold beyond which the scaled mixing rate saturates. We term the flow states that emerge after this transition point as *fully developed active turbulence*, in which not only the organization of topological defects becomes more uniform and the system crosses over from a

maximal defect pathlength, the scaled mixing rate of the active flows no longer increases with increasing activity.

Understanding the evolution of active systems with varying levels of activity is of fundamental importance in a wide range of biological systems, where the living units can adapt their activity in response to various chemical and mechanical stimuli [53, 54]. Our findings reveal a succession of transitions in the evolution of collective patterns of self-organization with increasing activity of the material. Beyond the well-established hydrodynamic instability of the ordered state [31, 32], we show that there exists a first activity threshold, above which nucleation of topological defects gets initiated. We further find that precisely at this activity threshold the director decorrelation time abruptly drops, signifying a rapid enhancement of temporal fluctuations in the director field. Moving beyond this activity threshold for defect nucleation, we uncover, a hitherto, hidden dynamic transition. This second transition is inherently spatiotemporal and thus hidden to purely spatial (time-averaged) and purely temporal (space-averaged) characterizations. At this second activity threshold, the organization of topological defects in space and time becomes optimally ordered relative to uniformly random organization at higher activities, defect pathlength normalized by the average distance between the defects peaks, and the scaled mixing rate of the activity-induced flows saturates.

The existence of such an activity threshold for



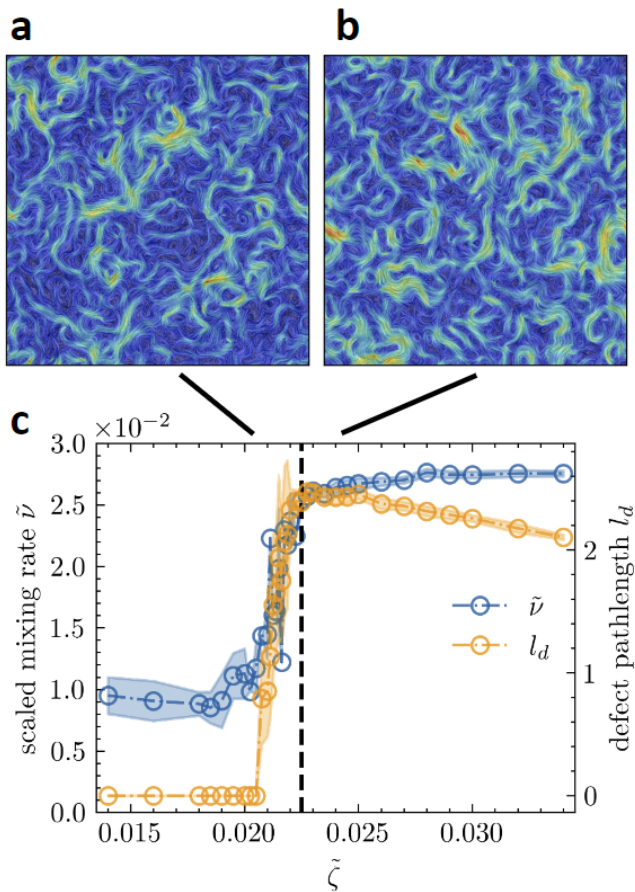


Figure 4. **Mixing rate and defect pathlength.** (a), (b): Snapshot of flow velocity magnitude overlaid with the line integral convolution of the velocity field at  $\tilde{\zeta} = 0.0205$ , resp.  $\tilde{\zeta} = 0.024$ . (c): Mixing rate  $\tilde{\nu}$  (scaled with the active timescale  $\mu/\zeta$ ) and defect pathlength  $l_d$  (scaled with the average distance between the defects) as a function of active stress  $\tilde{\zeta}$ . The transition point is marked by a vertical dashed black line.

spatiotemporal organization of topological defects and collective flows of active particles could have implications for the optimal evolution of the self-organization patterns in living materials [55–57]. Recent studies have shown that within the active turbulence state, the movement of topological defects can carry biochemical information on the membrane of living cells [58, 59] and enhance the topological mixing in filament-motor protein mixtures. Interestingly, it was found that the non-dimensional topological entropy remains constant across a range of activities in the fully turbulent regime [60]. It would be interesting to explore the connections between the spatiotemporal transition found in this work, to topological entropy in living materials. Finally, as the identification of suitable order parameters for non-equilibrium phase transitions remains a challenging task, the spatiotemporal nature of the transition highlights the importance of exploring order parameters that evolve both in space and in time for uncovering phase transitions in non-equilibrium systems, both experimentally and in the models of active materials.

**Acknowledgments** A. D. acknowledges funding from the Novo Nordisk Foundation (grant No. NNF18SA0035142 and NERD grant No. NNF21OC0068687), Villum Fonden (Grant no. 29476), and the European Union (ERC, PhysCoMeT, 101041418). Views and opinions expressed are however those of the authors only and do not necessarily reflect those of the European Union or the European Research Council. Neither the European Union nor the granting authority can be held responsible for them.

- [1] J. M. Kosterlitz, Reports on Progress in Physics **79**, 026001 (2016).
- [2] P. Poulin, H. Stark, T. Lubensky, and D. Weitz, Science **275**, 1770 (1997).
- [3] P. M. Chaikin and T. C. Lubensky, “Frontmatter,” in *Principles of Condensed Matter Physics* (Cambridge University Press, 1995) pp. i–vi.
- [4] P.-G. De Gennes and J. Prost, *The physics of liquid crystals*, Vol. 83 (Oxford university press, 1993).
- [5] L. Michel, Reviews of Modern Physics **52**, 617 (1980).
- [6] M. J. Bowick and L. Giomi, Advances in Physics **58**, 449 (2009).
- [7] A. Doostmohammadi and B. Ladoux, Trends in Cell Biology (2021).
- [8] J. Christoph, M. Chebbok, C. Richter, J. Schröder-Schetelig, P. Bittihn, S. Stein, I. Uzelac, F. H. Fenton, G. Hasenfuß, R. Gilmour Jr, *et al.*, Nature **555**, 667 (2018).
- [9] X. Huang, W. Xu, J. Liang, K. Takagaki, X. Gao, and J.-y. Wu, Neuron **68**, 978 (2010).
- [10] Y. Maroudas-Sacks, L. Garion, L. Shani-Zerbib, A. Livshits, E. Braun, and K. Keren, Nature Physics **17**, 251 (2020).
- [11] K. Copenhagen, R. Alert, N. S. Wingreen, and J. W. Shaevitz, Nature Physics **17**, 211 (2020).
- [12] K. Kawaguchi, R. Kageyama, and M. Sano, Nature **545**, 327 (2017).
- [13] O. J. Meacock, A. Doostmohammadi, K. R. Foster, J. M. Yeomans, and W. M. Durham, Nature Physics **17**, 205 (2020).
- [14] P. Guillamat, C. Blanch-Mercader, G. Pernollet, K. Kruse, and A. Roux, Nature materials **21**, 588 (2022).
- [15] T. B. Saw, A. Doostmohammadi, V. Nier, L. Kocgozlu, S. Thampi, Y. Toyama, P. Marcq, C. T. Lim, J. M. Yeomans, and B. Ladoux, Nature **544**, 212 (2017).
- [16] M. C. Marchetti, J. F. Joanny, S. Ramaswamy, T. B.

- Liverpool, J. Prost, M. Rao, and R. A. Simha, *Reviews of Modern Physics* **85**, 1143 (2013).
- [17] A. Doostmohammadi, J. Ignés-Mullol, J. M. Yeomans, and F. Sagués, *Nature Communications* **9**, 3246 (2018).
- [18] T. Sanchez, D. T. N. Chen, S. J. DeCamp, M. Heymann, and Z. Dogic, *Nature* **491**, 431 (2012).
- [19] L. Giomi, M. J. Bowick, X. Ma, and M. C. Marchetti, *Phys. Rev. Lett.* **110**, 228101 (2013).
- [20] N. Kumar, R. Zhang, J. J. de Pablo, and M. L. Gardel, *Science Advances* **4** (2018), 10.1126/sciadv.aat7779.
- [21] S. Ramaswamy, *Annual Review Condensed Matter Physics* **1**, 323 (2010).
- [22] M. C. Marchetti, J. F. Joanny, S. Ramaswamy, T. B. Liverpool, J. Prost, M. Rao, and R. A. Simha, *Rev. Mod. Phys.* **85**, 1143 (2013).
- [23] J. Prost, F. Jülicher, and J.-F. Joanny, *Nature Physics* **11**, 111 (2015).
- [24] L. Giomi, M. J. Bowick, X. Ma, and M. C. Marchetti, *Physical Review Letters* **110**, 228101 (2013).
- [25] L. Bonn, A. Ardaševa, R. Mueller, T. N. Shendruk, and A. Doostmohammadi, *Physical Review E* **106**, 044706 (2022).
- [26] M. Serra, L. Lemma, L. Giomi, Z. Dogic, and L. Mahadevan, *Nature Physics* **19**, 1355–1361 (2023).
- [27] L. C. Head, C. Doré, R. R. Keogh, L. Bonn, G. Negro, D. Marenduzzo, A. Doostmohammadi, K. Thijssen, T. López-León, and T. N. Shendruk, *Nature Physics*, 1 (2024).
- [28] H. Wensink, J. Dunkel, S. Heidenreich, K. Drescher, R. E. Goldstein, H. Löwen, and J. M. Yeomans, *PNAS* **109**, 14308 (2012).
- [29] J. Urzay, A. Doostmohammadi, and J. Yeomans, *Journal of Fluid Mechanics* **822**, 762–773 (2017).
- [30] A. Doostmohammadi, T. N. Shendruk, K. Thijssen, and J. M. Yeomans, *Nature communications* **8**, 1 (2017).
- [31] R. Aditi Simha and S. Ramaswamy, *Phys. Rev. Lett.* **89**, 058101 (2002).
- [32] B. Martínez-Prat, J. Ignés-Mullol, J. Casademunt, and F. Sagués, *Nature physics* **15**, 362 (2019).
- [33] S. P. Thampi, R. Golestanian, and J. M. Yeomans, *EPL (Europhysics Letters)* **105**, 18001 (2014).
- [34] S. Martiniani, P. M. Chaikin, and D. Levine, *Phys. Rev. X* **9**, 011031 (2019).
- [35] S. Martiniani, Y. Lemberg, P. M. Chaikin, and D. Levine, *Phys. Rev. Lett.* **125**, 170601 (2020).
- [36] A. Cavagna, P. M. Chaikin, D. Levine, S. Martiniani, A. Puglisi, and M. Viale, *Phys. Rev. E* **103**, 062141 (2021).
- [37] A. Ziepeke, I. Maryshev, I. S. Aranson, and E. Frey, *Nature Communications* **13** (2022), 10.1038/s41467-022-34484-2.
- [38] A. Doostmohammadi, J. Ignés-Mullol, J. M. Yeomans, and F. Sagués, *Nature communications* **9**, 1 (2018).
- [39] S. P. Thampi and J. M. Yeomans, *The European Physical Journal Special Topics* **225**, 651 (2016).
- [40] R. Voituriez, J.-F. Joanny, and J. Prost, *EPL (Europhysics Letters)* **70**, 404 (2005).
- [41] S. Ramaswamy and M. Rao, *New Journal of Physics* **9**, 423 (2007).
- [42] D. Marenduzzo, E. Orlandini, M. E. Cates, and J. M. Yeomans, *Physical Review E* **76**, 031921 (2007).
- [43] A. N. Beris and B. J. Edwards, *Thermodynamics of Flowing Systems* (Oxford University Press, 1994).
- [44] G. Tóth, C. Denniston, and J. M. Yeomans, *Physical review letters* **88**, 105504 (2002).
- [45] C. Blanc, D. Svenešek, S. Žumer, and M. Nobili, *Physical review letters* **95**, 097802 (2005).
- [46] See Supplemental Material at <https://sid.erda.dk/sharelink/FXYg9PFak0> for movies of the director field and defects (Supplementary Movies 01-04).
- [47] J. Ziv and A. Lempel, *IEEE Transactions on information theory* **23**, 337 (1977).
- [48] T. M. Cover, *Elements of information theory* (John Wiley & Sons, 1999).
- [49] M. S. Warren and J. K. Salmon, *Proceedings of the 1993 ACM/IEEE conference on Supercomputing*, .
- [50] A. J. Tan, E. Roberts, S. A. Smith, U. A. Olvera, J. Arteaga, S. Fortini, K. A. Mitchell, and L. S. Hirst, *Nature Physics* **15**, 1033–1039 (2019).
- [51] K. A. Mitchell, M. M. H. Sabbir, K. Geumhan, S. A. Smith, B. Klein, and D. A. Beller, *Phys. Rev. E* **109**, 014606 (2024).
- [52] J.-L. Thiffeault, *Nonlinearity* **25**, R1 (2012).
- [53] N. Wadhwa and H. C. Berg, *Nature Reviews Microbiology* **20**, 161 (2022).
- [54] X. Trepast and E. Sahai, *Nature Physics* **14**, 671 (2018).
- [55] H. Reinken, S. H. L. Klapp, and M. Wilczek, *Physical Review Fluids* **7** (2022), 10.1103/physrevfluids.7.084501.
- [56] M. M. H. S. M. E. K. A. M. F. L. Memarian, D. Hammar and L. Hirst, (2024), 10.48550/ARXIV.2401.04363.
- [57] M. S. R. Backofen, A. Y. A. Altawil and A. Voigt, (2023), 10.48550/ARXIV.2311.14959.
- [58] T. H. Tan, J. Liu, P. W. Miller, M. Tekant, J. Dunkel, and N. Fakhri, *Nature Physics* **16**, 657 (2020).
- [59] J. Liu, J. F. Tetz, P. W. Miller, A. D. Hastewell, Y.-C. Chao, J. Dunkel, and N. Fakhri, *Proceedings of the National Academy of Sciences* **118** (2021).
- [60] A. J. Tan, E. Roberts, S. A. Smith, U. A. Olvera, J. Arteaga, S. Fortini, K. A. Mitchell, and L. S. Hirst, *Nature Physics* **15**, 1033 (2019).

## Chapter 4

# Conformal invariance in biological matter

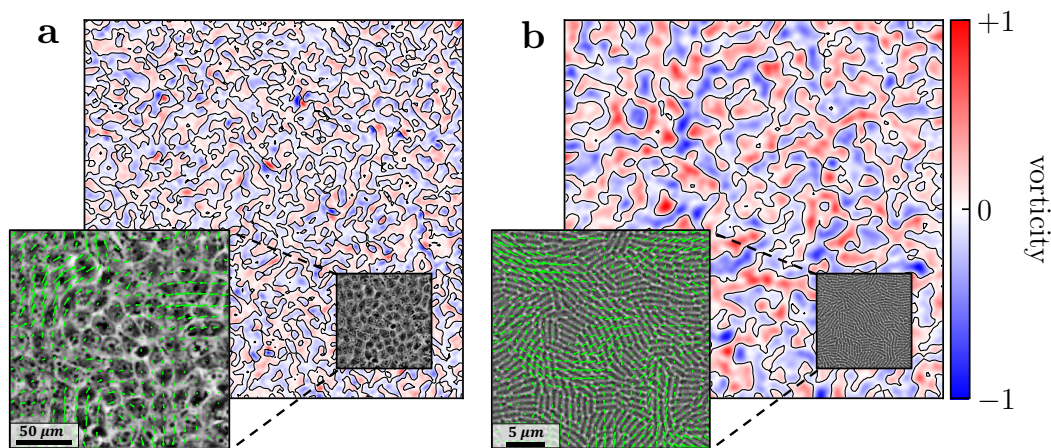


Figure 4.1: High-resolution analysis of coherent flows generated by groups of eukaryotic and prokaryotic cells. Shown are representative velocity and vorticity patterns observed in monolayers of (a) Madin-Derby Canine Kidney (MDCK) eukaryotic cells, and (b) wild-type *Pseudomonas aeruginosa* prokaryotic cells. The colormap indicates local vorticity, with zero-vorticity isolines depicted by black lines. Vorticity values are normalized to their maximum. Insets highlight a subset of cells within a single field of view, overlaid with green arrows representing local velocity. Movement was quantified using single-cell particle tracking velocimetry (PTV).

This study is entirely grounded in [1] and its objective is to investigate whether the observed scale invariance in the energy and enstrophy spectra of bacterial [2]

and active turbulence [3] can be extended to conformal invariance of zero-vorticity isolines. This will be achieved through a comprehensive statistical analysis of large-scale vortical flow phenomena in biological matter. By exploring the statistical properties of vortical flow at different length scales and employing various analytical techniques, such as Schramm-Loewner evolution (SLE) processes, the study aims to elucidate the potential presence of conformal symmetry in turbulent biological flows. Understanding the extent to which conformal invariance governs the dynamics of vortical flow in biological systems could provide valuable insights into the underlying principles shaping the behavior of active matter and contribute to the development of predictive models for complex biological phenomena.

## 4.1 Methods

### 4.1.1 Experimental data

High-resolution measurements, employing single-cell tracking, were conducted on monolayers composed of four distinct cellular genotypes, encompassing both eukaryotic and prokaryotic organisms. Within the eukaryotic group, this study included the widely studied Madin-Darby Canine Kidney (MDCK) cells and aggressive human breast cancer cells (MCF-7). As for prokaryotic cells, the opportunistic pathogen *Pseudomonas aeruginosa* was studied, renowned for its utilization of small appendages known as pili to navigate solid surfaces, a behavior commonly referred to as twitching motility. Two strains of *Pseudomonas aeruginosa* were investigated: the wild type (WT) and the hyperpiliated  $\Delta pilH$  mutant, which exhibited heightened motility and formed elongated cells compared to the parental WT strain. Both strains were previously published and characterized in [4, 5]. Each of these four cellular genotypes forms confluent monolayers, culminating in the emergence of two-dimensional patterns of collective motion, a hallmark of disordered flows observed across a wide array of systems. Notably, vortical flow structures, a hallmark of disordered flows observed across a wide array of systems, are evident in all four cellular genotypes investigated in this study (Fig. 4.1). Each vortex within these flows demonstrates either clockwise or counterclockwise rotation, with the zero-vorticity isolines delineating the boundary between regions of opposing rotational directions.

### 4.1.2 Numerical model

While various physical models of active matter have been proposed to approximate specific types of cells and their unique processes, this study focuses exclusively on the nematohydrodynamic model detailed in section 3.1. This model represents a

continuum framework that captures the collective behavior of active matter by coupling a nematic order parameter, which describes cell orientation, with an incompressible velocity field. The decision to utilize this specific model stems from its ability to capture essential features of cellular dynamics observed in experimental settings. The simulations were conducted a periodic quadratic domain of linear dimension  $L = 2048$ , all other parameters remained identical to those reported in section 3.1.1. By maintaining consistency with the parameters outlined in the previous section, a direct comparison between numerical predictions and experimental observations is facilitated.

### 4.1.3 Contour tracing

In fluid dynamics, analyzing contours of zero vorticity plays a pivotal role in understanding flow patterns and identifying regions of uniform or stagnant flow. To accomplish this, the vorticity field  $\omega$  is derived from the velocity field data  $(u_x, u_y)^T$ , using  $\omega = \partial_x u_y - \partial_y u_x$ . Both of the spatial derivatives are computed numerically using a 5-point stencil at every grid point. To locate the positions of zero-vorticity contours, we generate a binary field from the vorticity field using the ternary expression; 1 if  $w > 0$  else 0. Subsequently, contours of zero-vorticity are traced using the marching squares algorithm, a powerful tool that traces these contours by employing linear interpolation across grid cells. Additionally, to ensure accuracy and resolve potential ambiguities, foreground pixels are considered as *four*-connected at saddle points. This method preserves the orientation of contours by positioning sites of positive vorticity consistently to the right (Fig. 4.4b). Through the precise delineation of these contours, we gain valuable insights into the intricate dynamics of fluid flow phenomena.

## 4.2 Cluster geometry and scale invariance

Vorticity clusters are expected to possess a fractal nature, not unlike that of critical percolation. And as such, we expect both its complete- and accessible external-perimeter to be scale invariant. Clusters are identified and labelled using the two-pass binary connected-component labelling algorithm of Hoshen and Kopelman [6]. The complete perimeter (solid red curve in Fig. 4.2) is identified by tracing the contour of a cluster according to the above contour tracing algorithm (Sec. 4.1.3). The associated accessible external boundary (dashed green curve in Fig. 4.2) is constructed by dilating the boundary morphology [7,8] of the binary representation of the cluster, and its perimeter is then measured once more using the contour tracing algorithm.

The fractal dimension is measured by comparing the perimeter  $l$  to its radius of

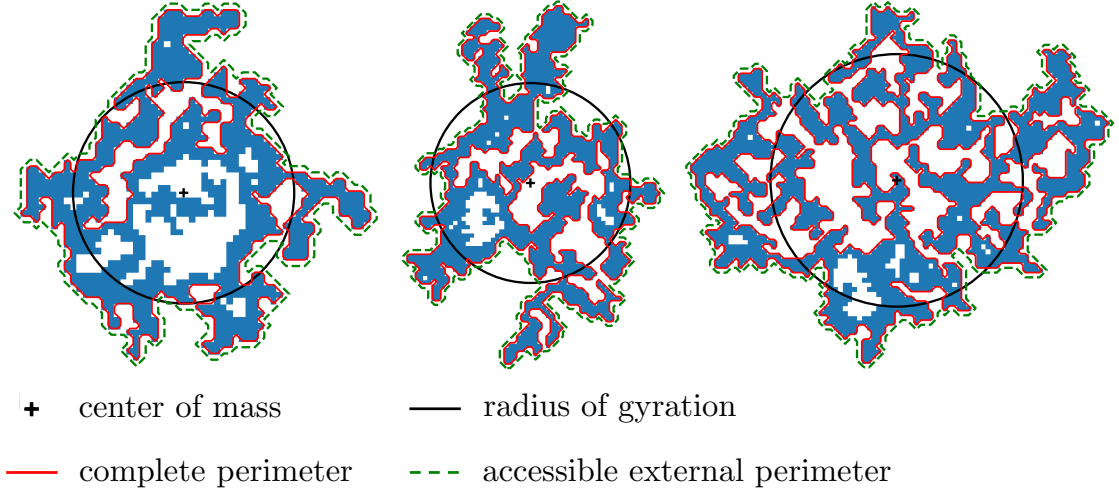


Figure 4.2: Three distinct clusters of positive vorticity identified in monolayer of wild-type *Pseudomonas aeruginosa* bacteria using PTV, accompanied by their complete perimeter (shown as a solid red curve), accessible external perimeter (displayed as a dashed green curve), and radius of gyration (depicted black circle).

gyration  $R_g$  (solid black curve in Fig. 4.2), for a large sample of vorticity clusters. The radius of gyration is computed as the positional mean squared displacement from its center of mass:

$$R_i^2 = \frac{1}{|s_i|} \sum_{n,m \in s_i} (r_n - r_m)^2 \quad \text{and} \quad R_g^2 = \frac{1}{N} \sum_{i=1}^N R_i^2, \quad (4.1)$$

where  $s_i$  denotes the set of lattice sites belonging to the  $i$ 'th cluster and  $|s_i|$  its cardinality. Remarkably, after rescaling the perimeter and radius of gyration of each system by the corresponding radius of gyration of the largest vorticity cluster (as shown in table 4.1), the results for all four distinct experiments and the model collapse onto the same line, indicative of a universal power-law behavior (Fig. 4.3). The fractal dimension for both the complete- and external-perimeter is found to agree with  $D = 7/4$  and  $D_* = 4/3$ , respectively. Measured values for each of the five datasets are obtained through fitting, and the resulting fractal dimensions are reported in table 4.2.

| WT bacteria       | $\Delta pilH$ bacteria | MDCK               | MCF7               | Model               |
|-------------------|------------------------|--------------------|--------------------|---------------------|
| 193 $\mu\text{m}$ | 200 $\mu\text{m}$      | 1150 $\mu\text{m}$ | 1130 $\mu\text{m}$ | $828\sqrt{K/\zeta}$ |

Table 4.1: Radius of gyration of the largest vorticity cluster. The model is reported in units of the active length scale  $\sqrt{K/\zeta}$ .

The fractal dimension of  $SLE_\kappa$  curves are known to be [9, 10]  $D_\kappa = 1 + \kappa/8$  for  $\kappa < 8$ . Additionally, it is conjectured [11] that the accessible external perimeter locally resembles  $SLE_{\kappa_*}$  curve with diffusivity parameter  $\kappa_* = 16/\kappa < 4$ . This implies the fulfillment of the duality relation  $4(D_\kappa - 1)(D_{\kappa_*} - 1) = 1$ , indicative of a conformal field theory with zero central charge. Consequently, the system maintains scale invariance on both manifolds with and without boundary, even with non-zero Euler characteristic. These observations align with the notion that these biological flow structures, besides being scale invariant, could exhibit much richer conformal symmetries [12].

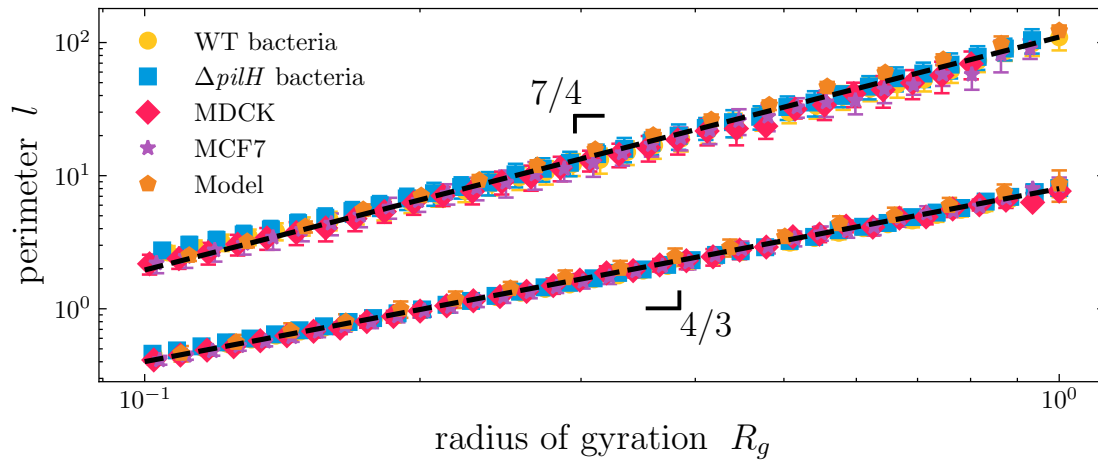


Figure 4.3: Complete- and accessible external-perimeter of vorticity clusters as a function of their radius of gyration. The complete perimeter collapse onto the top line with a slope of  $7/4$ , while the accessible external perimeter collapse onto the bottom line of slope  $4/3$ . Dashed lines are included as visual aids.

### 4.3 Vorticity contours and conformal invariance

Candidate  $SLE_\kappa$  traces are identified as follows (Fig. 4.4):

- 1) Draw a horizontal line representing the real axis across the binary vorticity field.
- 2) Label the intersection of a zero-vorticity contour and the real axis as the origin.
- 3) An explorer starting from the origin moves along the zero-vorticity contour according to the contour tracing algorithm (Sec. 4.1.3).

- 4) If returning to the real axis, tread on it while preserving orientation, until the explorer can re-enter the upper-half plane.

This procedure is guaranteed to faithfully reproduce the statistics of  $\text{SLE}_\kappa$  in the scaling limit if and only if this exploration process satisfy the locality property of  $\text{SLE}_6$  [13], which dictates that it does not interact with the boundary until it reaches it. As our observations confirm  $\kappa = 6$ , this procedure demonstrates self-consistency. A comparable technique was utilized in [14] for examining zero-vorticity isolines in two-dimensional turbulence.

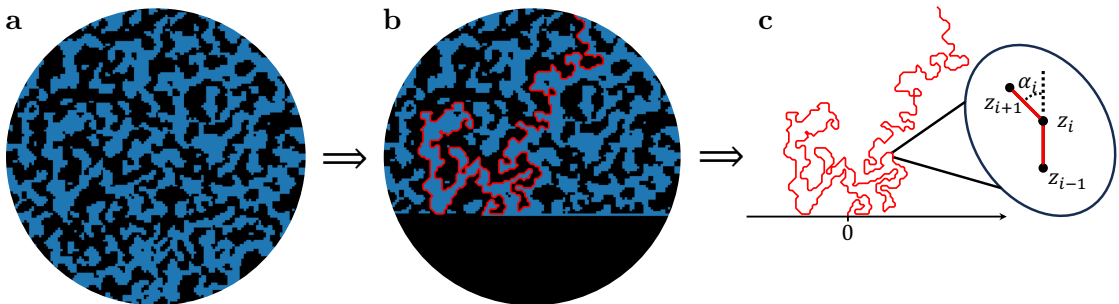


Figure 4.4: Schematic depiction of the procedure for generating candidate  $\text{SLE}_\kappa$  traces. (a) A binary vorticity field derived from monolayer of wild-type *Pseudomonas aeruginosa* bacteria using PTV, with black/blue sites denoting negative/positive vorticity. (b) A zero-vorticity contour crossing a horizontal line representing the real axis. (c) The labeled zero-vorticity contour is mapped to the upper half-plane and a schematic depiction of the turning angle  $\alpha_i$ , defined as angle between the two consecutive line segments  $[z_{i-1}, z_i]$  and  $[z_i, z_{i+1}]$ .

### 4.3.1 Winding angle

In the realm of stochastic processes, particularly within the framework of Schramm-Loewner evolution, the study of winding angles unveils fascinating insights. One notable feature facilitated by the elegant properties of SLE's is the precise prediction of winding angle behavior. The winding angle  $\theta_j$  of a curve sampled at the points  $\{z_j\}_{j=0}^N$  is defined as the cumulative sum  $\theta_j = \sum_{i=1}^j \alpha_i$  of the local turning angles  $\alpha_i$ . The turning angle  $\alpha_i$  is given by the angle between the two consecutive line segments  $[z_{i-1}, z_i]$  and  $[z_i, z_{i+1}]$ , as depicted in figure 4.4c. SLE theory enables exact predictions regarding the distribution of winding angles in the scaling limit. Specifically, it has been proven that these winding angles follow a Gaussian distribution, with a variance that exhibits logarithmic growth [15–18] with the distance



along the curve (arc length  $s$ ), consistent with the following relationship:

$$\text{Var}(\theta) = a + \alpha \log(s), \quad \text{with} \quad \alpha = \frac{2\kappa}{8 + \kappa}. \quad (4.2)$$

Figure 4.5b shows the rescaled probability distribution function (PDF) of the winding angle  $\theta$  at two distinct distances, agreeing with the standardized Gaussian distribution represented by the dashed black curve. Complementing this, figure 4.5a depicts the variance of the winding angle as function of the arc length  $s$ . The diffusivity parameter  $\kappa$  is estimated through fitting in accordance with equation (4.2) for each of the five datasets. The resulting parameters are then compiled and presented in table 4.2 for reference.

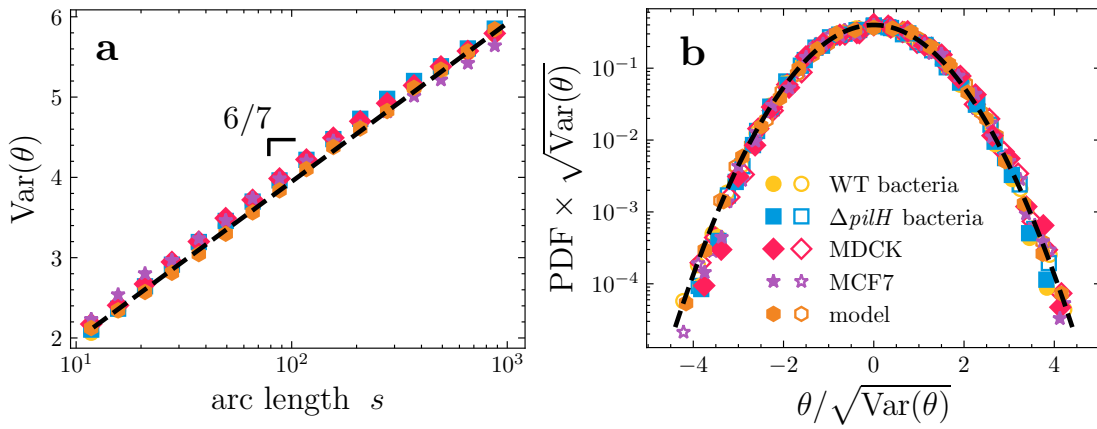


Figure 4.5: Winding angle statistics. (a) The variance of the winding angle as function of the distance along the curve (arch length  $s$ ) reveals a notable pattern; the data collapses onto the dashed line, which serves as a visual reference, with a slope of  $6/7$ . (b) The rescaled probability distribution of the winding angle is depicted for two distinct arc lengths: 64 (indicated by filled marks) and 512 (represented by open marks). A dashed black curve, representing the standardized Gaussian distribution, is included to aid visualization.

### 4.3.2 Left-passage probability

A renowned result from the SLE theory states that the probability  $P_\kappa$  of a chordal  $\text{SLE}_\kappa$  curve, where  $\kappa \in [0, 8)$ , passes to the left of a designated point  $z = \rho e^{i\phi}$  in the upper-half plane solely relies on its argument  $\phi$ . This probability is precisely given by Schramm's formula [19]:

$$P_\kappa(\phi) = \frac{1}{2} + \frac{\Gamma(4/\kappa)}{\sqrt{\pi}\Gamma(\frac{8-\kappa}{2\kappa})} \cot(\phi) {}_2F_1 \left[ \frac{1}{2}, \frac{4}{\kappa}, \frac{3}{2}, -\cot^2(\phi) \right], \quad (4.3)$$

where  $\Gamma$  is Euler's gamma function and  ${}_2F_1$  is Gauss' hypergeometric function.

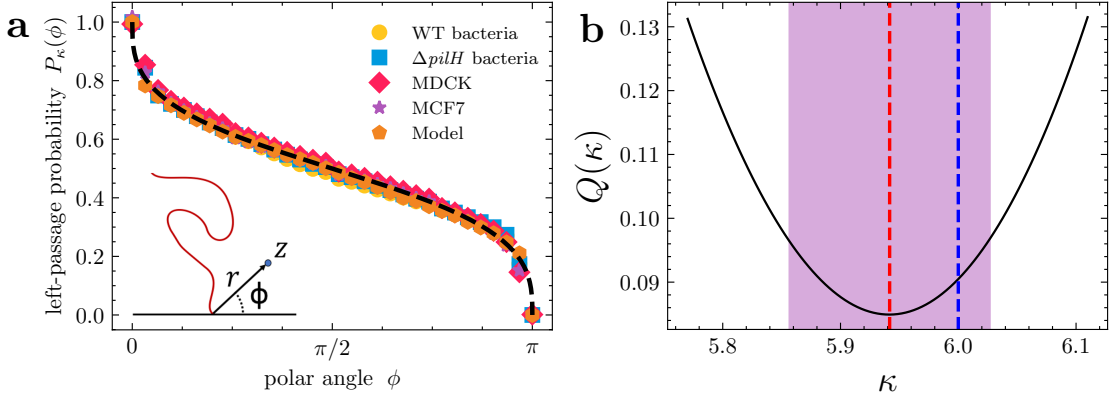


Figure 4.6: (a) The left-passage probability of putative SLE traces for each of the four cellular genotypes and the numerical model closely align with Schramm's formula (4.3) for  $\kappa = 6$ , depicted by the dashed black line. (b) The weighted mean square deviation  $Q(\kappa)$  as function of the diffusivity  $\kappa$  for the wild-type *Pseudomonas aeruginosa* bacteria is illustrated using PTV data. A blue vertical dashed line serves as a visual guide at  $\kappa = 6$ . The minimum value of the mean square deviation is identified at  $\kappa = 5.94 \pm 0.08$ , represented by the red vertical dashed line. The shaded magenta region delineates the error bar associated with the measured minimum value.

The left-passage probability is assessed by fixing a finite set  $\mathcal{S}$  comprising 512 points, regularly distributed within a semi-annulus centered at the origin. Subsequently, the probability  $P(z)$  is calculated, denoting the probability of a putative SLE trace passing to the left of the points in  $\mathcal{S}$ . Figure 4.6a shows the result of averaging the distribution  $P(z)$  along radial directions for each angular value  $\phi$ . In accordance with [20], the diffusivity parameter  $\kappa$  is determined by minimizing the weighted mean square deviation:

$$Q(\kappa) = \frac{N-1}{|\mathcal{S}|} \sum_{z \in \mathcal{S}} \frac{[P(z) - P_\kappa(\arg z)]^2}{P(z)[1 - P(z)]}, \quad (4.4)$$

where  $N$  is the number of samples and  $|\mathcal{S}|$  denotes the cardinality of the set  $\mathcal{S}$ .

### 4.3.3 Driving function

The stochastic driving function  $U_t : [0, T] \rightarrow \mathbb{R}$  encoding the information of a chordal  $\text{SLE}_\kappa$  curve is measured by numerically integrating the forward chordal

Loewner equation [21]:

$$\partial_t g_t(z) = \frac{2}{g_t(z) - U_t}, \quad (4.5)$$

with initial condition  $g_0(z) = z$ . The numerical integration scheme is simple; introduce a partition  $0 = t_0 < t_1 < \dots < t_n = T$  of the time interval  $[0, T]$  and approximate the driving function  $U_{t_k} = \delta_k$  as constant on each short time interval  $\Delta_k = t_k - t_{k-1}$ . Then the uniformizing conformal map  $g_{t_k}(z)$  is obtained by explicitly solving the Loewner equation (4.5). There are many such solutions [22] and this study uses the perhaps simplest of them all, the vertical slit-map [23]:

$$g_{t_k}(z) = \sqrt{(z - \delta_k)^2 + 4\Delta_k} + \delta_k, \quad (4.6)$$

which merely sends the vertical slit extending from  $\delta_k$  to  $\delta_k + 2i\sqrt{\Delta_k}$  onto the real axis (Fig. 4.7a-b). Presume we have a putative chordal  $\text{SLE}_\kappa$  trace sampled at the points  $\{z_0^0 = 0, z_1^0, \dots, z_l^0\}$ , the Loewner times  $t_k$  and driving function  $U_{t_k}$  are computed iteratively by successive application of the vertical slit-map (4.6). At each iteration step, the points  $\{z_k^{k-1}, z_{k+1}^{k-1}, \dots, z_l^{k-1}\}$  gets mapped to the reduced sequence of points  $\{z_{k+1}^k = g_{t_k}(z_{k+1}^{k-1}), \dots, z_l^k = g_{t_k}(z_l^{k-1})\}$ , as depicted in figure 4.7c.

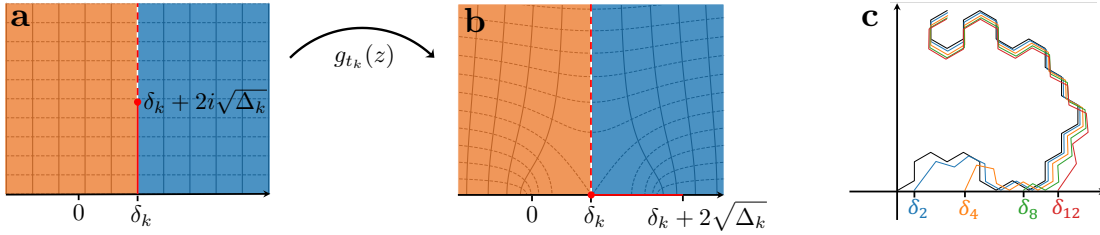


Figure 4.7: (a-b) Schematic illustrating the vertical slit-map (equation 4.6). (c) Visualization of the vertical zipper algorithm: the initial path (black) undergoes successive conformal mappings onto the real axis through an iterative process.

In figure 4.8a, the variance of the driving function is displayed for each of the four cellular genotypes alongside the numerical model. This involves linearly interpolating each instance of the driving function to ensure that all instances are defined for a uniform and equally spaced time sequence. In order to assert that zero-vorticity curves are genuinely SLE curves, possessing both conformal invariance and adhering to the domain Markov property, the extracted driving function  $U_{t_k}$  must be a one-dimensional Brownian process. Specifically, its variance should scale linearly with Loewner time according to  $\text{Var}(U_t) = \kappa t$ , and it should be Gaussian distributed at every time instance as well, as observed in figure 4.8b. Nonetheless, as demonstrated by [24] these criteria alone are not sufficient tests,

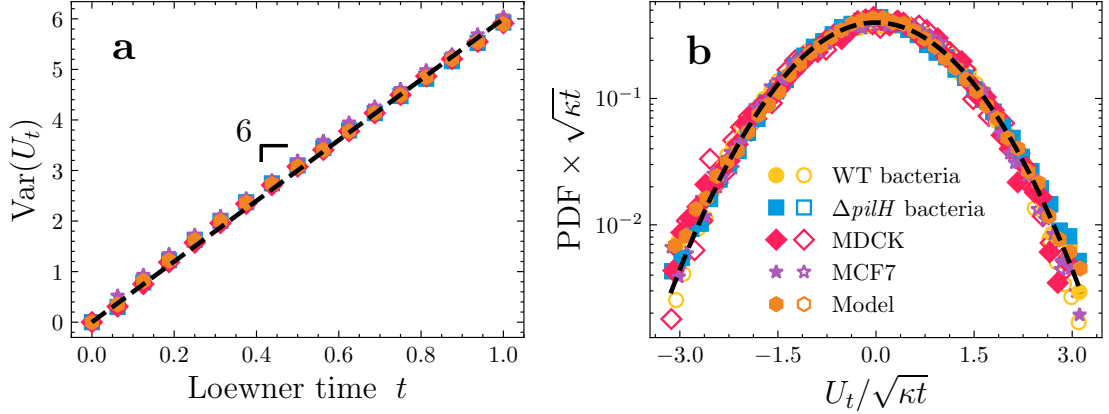


Figure 4.8: Driving function statistics. (a) The variance of the driving function  $U_t$  as function of the Loewner time  $t$  closely matches the prediction of it being a one-dimensional Brownian process with  $\kappa = 6$  (shown by the dashed black line). (b) The rescaled probability distribution of the driving function is depicted for two separate Loewner times: 0.25 (indicated by filled marks) and 0.75 (represented by open marks). Additionally, a dashed black curve, which represents the standardized Gaussian distribution, is included as a guide to the eye.

as they are also satisfied by non-SLE $_{\kappa}$  processes. Following [20], an examination of the correlation function

$$C(t; \tau) = \frac{\text{Cov}(\delta U_{t+\tau}, \delta U_t)}{\sqrt{\text{Var}(\delta U_{t+\tau})\text{Var}(\delta U_t)}} \quad (4.7)$$

of the driving function increments  $\delta U_t$  can determine whether the driving function indeed behaves as a Markovian process. The autocorrelation function, as depicted in figure 4.9, exhibits a rapid decay with lag time. This observation is consistent with the Markov property anticipated for Schramm-Loewner evolution contours in the scaling limit.

## 4.4 Conclusion

The analysis of various metrics such as the fractal dimension of zero-vorticity clusters, winding angle, left-passage probability, and driving function of zero-vorticity contours (table 4.2) strongly suggests that the statistical behavior of zero-vorticity isolines across the four cellular genotypes alongside the numerical model are described by a SLE $_6$  process within experimental accuracy and consequently fall into universality class of critical percolation, the simplest universality of critical phenomena. This discovery is remarkable because, despite the collective cellular

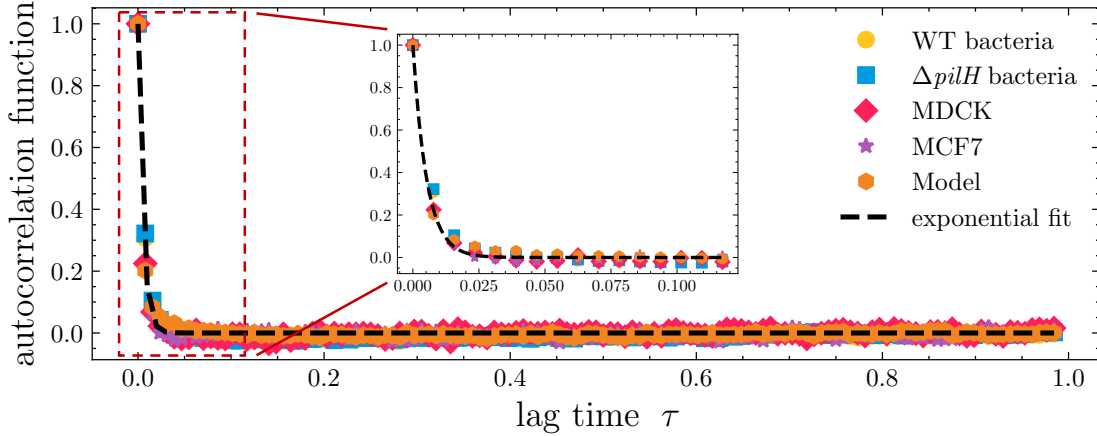


Figure 4.9: Autocorrelation function of the driving function (4.7) plotted against lag time  $\tau$ . The initial decay is attributed to the finite lattice spacing, which introduces short-range correlations. The exponential fit reveals a half-life of 0.0036, in Loewner time units. The inset provides a magnified view of the initial decay.

motility generating flow patterns with significantly larger length scales than those of individual cells (see figure 4.1), the resulting zero-vorticity contours exhibit the locality property inherent to  $\text{SLE}_6$  processes. Furthermore, considering the non-local constraint imposed by the flow incompressibility condition in the numerical model (in contrast to the experimental data), it is surprising that the contours exhibit this locality property. Further exploration is needed to determine the extent to which these discoveries signify that the universal nature of percolation extends to biological matter, particularly active turbulence. Additionally, it is crucial to investigate whether and how conformal invariance is broken in the statistics of non-zero vorticity isolines.

|                           |                          | continuum model | experimental data |                 |                  |                 | percolation universality class |                     |
|---------------------------|--------------------------|-----------------|-------------------|-----------------|------------------|-----------------|--------------------------------|---------------------|
|                           |                          |                 | bacterial cells   |                 | eukaryotic cells |                 |                                |                     |
|                           |                          |                 | WT                | $\Delta pilH$   | MDCK             | MCF7            |                                |                     |
| scale invariance          | complete perimeter       | $D$             | $1.75 \pm 0.01$   | $1.72 \pm 0.02$ | $1.72 \pm 0.04$  | $1.74 \pm 0.02$ | $1.74 \pm 0.03$                | $7/4 = 1.75$        |
|                           | external perimeter       | $D_*$           | $1.345 \pm 0.003$ | $1.27 \pm 0.01$ | $1.30 \pm 0.02$  | $1.29 \pm 0.02$ | $1.27 \pm 0.01$                | $4/3 \approx 1.33$  |
| conformal invariance      | winding angle            | $\alpha$        | $0.853 \pm 0.005$ | $0.86 \pm 0.01$ | $0.87 \pm 0.01$  | $0.85 \pm 0.01$ | $0.87 \pm 0.02$                | $6/7 \approx 0.857$ |
| Schramm-Loewner Evolution | left-passage probability | $\kappa$        | $6.02 \pm 0.02$   | $5.97 \pm 0.05$ | $5.96 \pm 0.05$  | $5.95 \pm 0.03$ | $5.95 \pm 0.06$                | 6                   |
|                           | driving function         | $\kappa$        | $5.96 \pm 0.05$   | $6.03 \pm 0.06$ | $5.96 \pm 0.06$  | $5.98 \pm 0.04$ | $5.93 \pm 0.04$                | 6                   |

Table 4.2: Critical exponents and parameters measured from the velocity fields derived from each of the four cellular genotypes using single-cell particle tracking velocimetry (PTV), in conjunction with the numerical model. Errors represent standard deviation about the mean.

## Bibliography

- [1] Benjamin H. Andersen, Francisco M. R. Safara, Valeriia Grudtsyna, Oliver J. Meacock, Simon G. Andersen, William M. Durham, Nuno A. M. Araujo, and Amin Doostmohammadi. Evidence of robust, universal conformal invariance in living biological matter. *arXiv preprint arXiv:2403.08466*, 2024.
- [2] Henricus H Wensink, Jörn Dunkel, Sebastian Heidenreich, Knut Drescher, Raymond E Goldstein, Hartmut Löwen, and Julia M Yeomans. Meso-scale turbulence in living fluids. *Proceedings of the national academy of sciences*, 109(36):14308–14313, 2012.
- [3] Ricard Alert, Jean-François Joanny, and Jaume Casademunt. Universal scaling of active nematic turbulence. *Nature Physics*, 16(6):682–688, 2020.
- [4] Jacob J Bertrand, Joyce T West, and Joanne N Engel. Genetic analysis of the regulation of type iv pilus function by the chp chemosensory system of *pseudomonas aeruginosa*. *Journal of bacteriology*, 192(4):994–1010, 2010.
- [5] Oliver J Meacock, Amin Doostmohammadi, Kevin R Foster, Julia M Yeomans, and William M Durham. Bacteria solve the problem of crowding by moving slowly. *Nature Physics*, 17(2):205–210, 2021.
- [6] Joseph Hoshen and Raoul Kopelman. Percolation and cluster distribution. I. cluster multiple labeling technique and critical concentration algorithm. *Physical Review B*, 14(8):3438, 1976.
- [7] Jean Serra. *Image analysis and mathematical morphology*. Academic Press, Inc., 1983.
- [8] Robert M Haralick, Stanley R Sternberg, and Xinhua Zhuang. Image analysis using mathematical morphology. *IEEE transactions on pattern analysis and machine intelligence*, (4):532–550, 1987.
- [9] Hubert Saleur and Bertrand Duplantier. Exact determination of the percolation hull exponent in two dimensions. *Physical review letters*, 58(22):2325, 1987.
- [10] Vincent Beffara. The dimension of the sle curves. 2008.
- [11] Bertrand Duplantier. Conformally invariant fractals and potential theory. *Physical Review Letters*, 84(7):1363, 2000.
- [12] Bertrand Duplantier. Higher conformal multifractality. *Journal of statistical physics*, 110:691–738, 2003.

- [13] Gregory Lawler, Oded Schramm, and Wendelin Werner. Conformal restriction: The chordal case. *Journal of the American Mathematical Society*, 16(4):917–955, 2003.
- [14] D. Bernard, G. Boffetta, A. Celani, and G. Falkovich. Conformal invariance in two-dimensional turbulence. *Nature Physics*, 2:124–128, 2006.
- [15] Bertrand Duplantier and Hubert Saleur. Winding-angle distributions of two-dimensional self-avoiding walks from conformal invariance. *Physical review letters*, 60(23):2343, 1988.
- [16] Benjamin Wieland and David B Wilson. Winding angle variance of fortuin-kasteleyn contours. *Physical Review E*, 68(5):056101, 2003.
- [17] Guido Boffetta, A Celani, D Dezzani, and A Seminara. How winding is the coast of britain? conformal invariance of rocky shorelines. *Geophysical research letters*, 35(3), 2008.
- [18] A. A. Saberi and S. Rouhani. Scaling of clusters and winding-angle statistics of isoheight lines in two-dimensional kardar-parisi-zhang surfaces. *Physical Review E*, 79(3):036102, 2009.
- [19] O. Schramm. A percolation formula. *Electronic Communications in Probability*, 6:115 – 120, 2001.
- [20] Nicolas Posé, K Julian Schrenk, Nuno AM Araújo, and Hans J Herrmann. Shortest path and schramm-loewner evolution. *Scientific reports*, 4(1):5495, 2014.
- [21] Karl Löwner. Untersuchungen über schlichte konforme abbildungen des einheitskreises. i. *Mathematische Annalen*, 89(1-2):103–121, 1923.
- [22] Donald E Marshall and Steffen Rohde. Convergence of a variant of the zipper algorithm for conformal mapping. *SIAM journal on numerical analysis*, 45(6):2577–2609, 2007.
- [23] Tom Kennedy. Numerical computations for the schramm-loewner evolution. *Journal of Statistical Physics*, 137:839–856, 2009.
- [24] Tom Kennedy. Computing the loewner driving process of random curves in the half plane. *Journal of Statistical Physics*, 131:803–819, 2008.

## Manuscript

TITLE: Evidence of robust, universal conformal invariance in living biological matter

AUTHORS: Benjamin H. Andersen<sup>1†</sup>, Francisco M. R. Safara<sup>2,3†</sup>, Valeriia Grudtsyna<sup>1</sup>, Oliver J. Meacock<sup>4,5</sup>, Simon G. Andersen<sup>1</sup>, William M. Durham<sup>5</sup>, Nuno A. M. Araujo<sup>2,3</sup>, and Amin Doostmohammadi<sup>1</sup>

<sup>1</sup>Niels Bohr Institute, University of Copenhagen, Copenhagen, Denmark.

<sup>2</sup>Departamento de Física, Faculdade de Ciências, Universidade de Lisboa, Lisboa, Portugal.

<sup>3</sup>Centro de Física Teórica e Computacional, Faculdade de Ciências, Universidade de Lisboa, Lisboa, Portugal.

<sup>4</sup>Department of Fundamental Microbiology, University of Lausanne, Lausanne, Switzerland

<sup>5</sup>Department of Physics and Astronomy, University of Sheffield, Sheffield, United Kingdom

† These authors contributed equally to this work.

MY CONTRIBUTION: Developed the computational framework, conducted simulations, created figures, and contributed to the writing of the supplementary materials and methods.

PUBLICATION STATUS: Available as a preprint on *arXiv*, Submitted March 13th, 2024.

HYPERLINK: <https://doi.org/10.48550/arXiv.2403.08466>



# Evidence of robust, universal conformal invariance in living biological matter

Benjamin H. Andersen<sup>1</sup>, Francisco M. R. Safara<sup>2,3</sup>,  
Valeriia Grudtsyna<sup>1</sup>, Oliver J. Meacock<sup>4,5</sup>,  
Simon G. Andersen<sup>3</sup>, William M. Durham<sup>5\*</sup>, Nuno A. M. Araujo<sup>2,3\*</sup>  
Amin Doostmohammadi<sup>1\*</sup>

<sup>1</sup>Niels Bohr Institute, University of Copenhagen, Copenhagen, Denmark

<sup>2</sup>Departamento de Física, Faculdade de Ciências, Universidade de Lisboa, Lisboa, Portugal

<sup>3</sup>Centro de Física Teórica e Computacional, Faculdade de Ciências,  
Universidade de Lisboa, Lisboa, Portugal

<sup>4</sup>Department of Fundamental Microbiology, University of Lausanne, Lausanne, Switzerland

<sup>5</sup>Department of Physics and Astronomy, University of Sheffield, Sheffield, United Kingdom

\*To whom correspondence should be addressed:

[w.m.durham@sheffield.ac.uk](mailto:w.m.durham@sheffield.ac.uk), [nmaraujo@fc.ul.pt](mailto:nmaraujo@fc.ul.pt), [doostmohammadi@nbi.ku.dk](mailto:doostmohammadi@nbi.ku.dk)

## Abstract

Collective cellular movement plays a crucial role in many processes fundamental to health, including development, reproduction, infection, wound healing, and cancer. The emergent dynamics that arise in these systems are typically thought to depend on how cells interact with one another and the mechanisms used to drive motility, both of which exhibit remarkable diversity across different biological systems. Here, we report experimental evidence of a universal feature in the patterns of flow that spontaneously emerges in groups of collectively moving cells. Specifically, we demonstrate that the flows generated by collectively moving dog kidney cells, human breast cancer cells, and by two different strains of pathogenic bacteria, all exhibit conformal invariance. Remarkably, not only do our results show that all of these very different systems display robust conformal invariance, but we also discovered that the precise form of the invariance in all four systems is described by the Schramm-Loewner Evolution (SLE), and belongs to the percolation universality class. A continuum model of active matter can recapitulate both the observed conformal invariance and SLE form found in experiments. The presence of universal conformal invariance reveals that the macroscopic features of living biological matter exhibit universal translational, rotational, and scale symmetries that are independent of the microscopic properties of its constituents. Our results show that the patterns of flows generated by diverse cellular systems are highly conserved and that biological systems can unexpectedly be used to experimentally test predictions from the theories for conformally invariant structures.

Understanding the collective movement of large populations, and how it arises from its constituents, is a central problem in biology, ecology, material science and physics [1, 2, 3, 4]. In these living systems, work is produced at the level of an individual constituent, and this ‘activity’ is translated into patterns of collective motion at larger length scales through interactions between them [5, 1]. However, many of the processes involved in collective movement, including the mechanisms that individual constituents use to propel themselves, the processes that give rise to interactions, and the behavioural responses to stimuli, are incredibly diverse in different biological systems and are often difficult to decode [6, 7]. While many different models have been proposed to reproduce the specific pattern of collective movement made by particular organisms, we lack a general unifying theory or set of principles that unite the collective movement observed across distinct biological systems.

In contrast, the study of the complex interactions between the components that make up certain inanimate materials, like metals and alloys, has led to the discovery of universal behavior near the so-called critical regimes. In these conditions, the global macroscopic properties no longer depend on the specific properties of the individual constituents, but rather exhibit “universal” behavior [8]. The principles that give rise to this universality in inanimate materials have been described using the framework of conformal field theory [9, 10], which predicts how shapes and angles of structures will be locally conserved across different systems, but not necessarily their length scales or curvatures. While the techniques used to describe conformally invariant structures have long been used to make theoretical predictions in statistical mechanics and condensed matter physics [9, 10] and to establish the universality of critical phenomena (for example, using numerical studies of turbulence [11, 12, 13] and rigidity percolation [14, 15]), direct experimental observation of conformal invariance and robust universal critical behavior in living matter remains elusive.

In this paper, we experimentally demonstrate that the patterns of collective movement observed in different types of living matter exhibit universal characteristics that transcend the particular properties of the cells from which they are composed. We show that vastly different systems, including colonies of pathogenic bacteria, groups of collectively moving dog kidney cells, and human breast cancer cells, all spontaneously generate flows that exhibit a universal conformal invariance that can be described by the percolation universality class. This finding suggests that collective cellular movement, which plays an important role in many biological systems [3, 16, 17], could potentially serve as a fundamental test bed for theories that are based on conformal symmetry.

We made high-resolution measurements of monolayers composed of four different cellular genotypes, including both prokaryotes and eukaryotes, to resolve whether we could identify common features in their collective motility. For prokaryotes, we studied the opportunistic pathogen *Pseudomonas aeruginosa*, which uses tiny grappling hooks called pili to pull themselves along solid surfaces, a process known as twitching motility [18]. We considered two different strains of this rod-shaped bacteria - wild type (WT) PAO1 and a deletion mutant  $\Delta pilH$  lacking one of the response regulators in the Pil-Chp system, which causes it to become hyper-piliated, move faster, and form longer cells than its parental WT [18, 19, 20]. For the eukaryotic cells, we considered the commonly studied Madine-Darby-Canine-Kidney (MDCK) cells [21], and aggressive human breast cancer cells (MCF-7) [22]. Each of these genotypes forms monolayers through in-situ growth and exhibits two-dimensional collective patterns of motion when they reach confluence. Vortical flow structures, a characteristic feature of the disordered flows

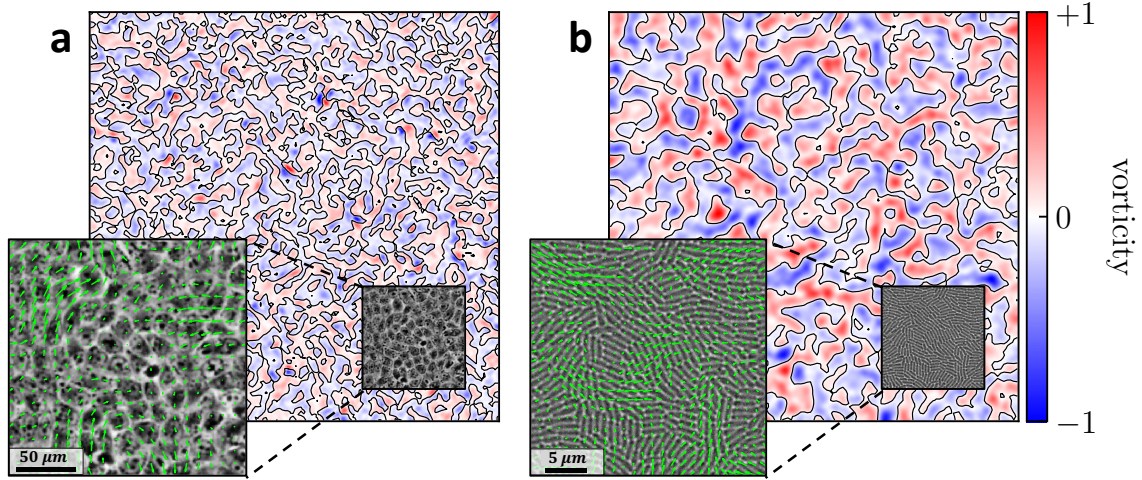
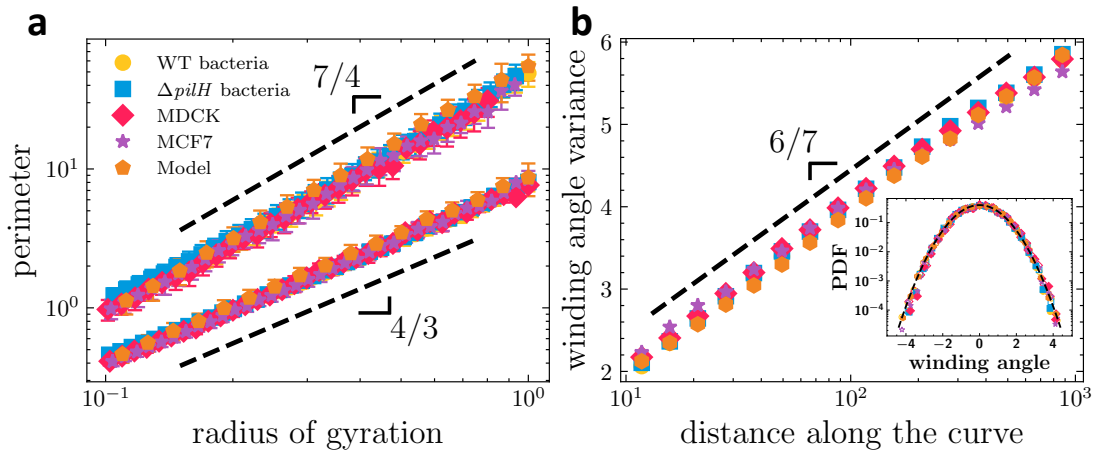


Figure 1: **High-resolution measurements of the coherent flows from collectives of eukaryotic and prokaryotic cells.** Representative velocity and vorticity fields observed in monolayers of (a) eukaryotic Madin-Derby Canine Kidney (MDCK) cells, and (b) prokaryotic wild-type *Pseudomonas aeruginosa* cells. The colormap shows the local vorticity and zero-vorticity contours are marked with black lines. The vorticity is normalised by its maximum value. Insets show a subset of the cells within a single field of view, which have been overlaid with green arrows showing the local velocity. Here we have quantified movement using single cell tracking (PTV), but we have also verified our results using particle image velocity (PIV) (*Materials and Methods*).

observed in wide diversity of different systems [23], are observed in all four of the cellular genotypes investigated here (e.g. see Fig. 1). Each vortex either exhibits clockwise or anti-clockwise rotation and the line that sits at the boundary between flows that rotate in opposite directions, the zero-vorticity contour, provides a measure of the underlying structure of the flow.

To compare how the flow structure varies across the four different experimental systems, we first measure the fractal dimension of the vorticity contours by plotting the perimeter of closed contours as a function of their radius of gyration. Surprisingly, without any fitting, special scaling, or free parameters, the results for all four different experiments collapse on the same line and exhibit the same power-law behavior (Fig. 2a). This provides concrete evidence of scale invariance and indicates that the flows generated by these diverse cellular systems share the same generic features. Interestingly, the slope of the perimeter-gyration radius plot, or fractal dimension, is  $D = 7/4$  for the complete perimeter and  $D_* = 4/3$  for the accessible external perimeter (Fig. S2) and satisfies the duality relation  $4(D - 1)(D_* - 1) = 1$ , conjectured for conformally invariant curves [24]. This finding suggests that these biological flow structures, in addition to being scale invariant, could exhibit much richer conformal symmetries [25].

To test whether our experimental data exhibits conformal invariance, we calculated the winding angle of the vorticity contours across the four different experimental systems. The winding angle is defined as the angle between two points on a contour that are separated by a



**Figure 2: Vorticity contours from four distinct cellular systems exhibit the same patterns of scale and conformal invariance, which is recapitulated using a continuum model of active fluids.** (a) The perimeter of contours as a function of their radius of gyration for two prokaryotic and two eukaryotic genotypes, including wild-type *P. aeruginosa* bacteria (yellow circles) and a hyperpilated  $\Delta pilH$  *P. aeruginosa* mutant (blue squares) that individually move faster, Madine-Darby Canine Kidney cells (red diamonds), and MCF-7 human breast cancer cells (purple stars). Here we separately analysed the complete perimeter and accessible external perimeter of the contours (SI Fig. S2) - we found that the experimental data for all four genotypes collapsed onto lines with slopes of approximately  $7/4$  and  $4/3$  respectively for the two different perimeter measurements. The flow fields produced by a numerical model of active fluids (*Materials and Methods*) generated vorticity contours with a power-law dependency in close agreement with that observed in experiments. The radius of gyration is normalised by the maximum system size (*Materials and Methods*). (b) The variance in the distribution of the winding angle, plotted here as a function of distance along the curve for the four experimental systems and numerical model, all exhibit the same logarithmic scaling with a slope of  $6/7$  (dashed line). (b; inset) In addition, the distribution of winding angles for a fixed distance along the contour is closely approximated by a Gaussian (dashed line). Both findings are consistent with that predicted for conformally invariant curves, which exhibit the same fractal dimension that we obtained for our data in Fig. 2a. The dashed lines correspond to the slope  $6/7$  and a standard Gaussian distribution, respectively. In (b; inset) the winding angles are obtained for segments of contours of length 64 (filled symbols) and 512 (empty symbols) and measured relative to the average angle of the contour. Results are averages over different samples and error bars represent the standard deviation (see *Materials and Methods*).

given distance measured along the contour (*Materials and Methods*). For conformally invariant curves (i) the winding angles are Gaussian distributed and (ii) the variance in the distribution of winding angles increases logarithmically with the length of the curve [26]. Our experimental data is in close agreement with both predictions for conformal invariance – with both metrics collapsing the data from the vorticity contours of the four cellular systems onto the same line (Fig. 2b and Fig. S4). Moreover, the rate at which the variance of the winding angle increases with the logarithm of the length is predicted to scale as  $\alpha = 6/7 = 2(D - 1)/D$  for conformally

invariant curves [26]. Thus, for the fractal dimension of  $D = 7/4$  we measured in Fig. 2a, we would predict that  $\alpha = 6/7$ , which is supported by our direct measurements of the variance (Fig. 2b).

Our results strongly suggest that the flows spontaneously generated by diverse cellular genotypes exhibit robust conformal invariance. We next sought to ascertain we could resolve which universality class these biological flows belong to. One of the central mathematical breakthroughs of the last few decades was to demonstrate that certain systems with conformal invariance and domain Markov property, can be described, in the scaling limit of interfaces, by a family of planar curves defined by a single parameter  $\kappa$ . This formalism is known as the Schramm-Loewner Evolution (SLE) [27, 28] and the value of the  $\kappa$  distinguishes different fundamental statistical mechanics models at criticality and thus resolves the universality class that a system belongs to [29, 30, 31]. To determine if the vorticity contours in the cellular systems are SLE curves, we extracted the  $\kappa$  parameter from the four experimental systems. We used two distinct and independent methods [32]: (i) directly calculating the driving function [33], and (ii) measuring the left-passage probability, comparing both to analytic predictions for the SLE [34] (*Materials and Methods*). Both methods consistently yielded  $\kappa = 6$ , for all four cellular genotypes (Fig. 3). The value of  $\kappa = 6$  is also consistent with the estimated fractal dimension, ( $D$ , Fig. 2a), which for SLE is related to  $\kappa$ , as  $D = 1 + \kappa/8$  [35]. This particular value of  $\kappa$  has an important physical meaning, as it has been uniquely proven for  $\kappa = 6$  that SLE curves correspond to the contours of critical percolation clusters and have the locality property (such that the properties only depend on the immediate neighborhood) [30, 36]. As such, our analyses reveal that the vorticity contours found in the four different cellular systems are not only conformally invariant, but they also all fall into the universality class of percolation.

Our experimental results indicate that diverse cellular types collectively generate flows with remarkably similar patterns of scale and conformal invariance, implying that the physical mechanisms that underlie the flow structures are highly conserved. While many different physical models of active matter have been developed to approximate specific types of cells and the processes unique to them [5, 2, 37], we tested whether a generic model could recapitulate our experimental observations. We used a simple continuum model in which a nematic order parameter (corresponding to cell orientation) was coupled to an incompressible velocity field (*see Materials and Methods* for further details). The two main parameters are the activity  $\zeta$ , represented by active stress generation in the velocity equation, and elasticity, represented by the elastic constant  $K$  that penalizes deformations. Dimensional analysis of the governing equations yields a characteristic length scale of  $K/\zeta$ , which defines the fundamental length scale of the flow. We find that the vorticity contours of this minimal model recapitulate each of the measurements observed in our experimental systems, including the fractal dimension  $D = 7/4$  (Fig. 2a), winding angle scaling  $\alpha = 6/7$  (Fig. 2b), and the scaling of the driving function and left-passage probability  $\kappa = 6$  (Fig. 3 and Table 1). While differences in cell morphology, intercellular adhesion, mechanotransduction, and the mechanisms that give rise to local alignment can all affect patterns of collective motility [38, 39, 7], the results of our continuum model imply that such idiosyncratic characteristics do not materially influence scale and conformally invariant flow patterns, but rather they are a generic feature of collective cellular flows.

The observed scaling of the vorticity contours from both experiments and model are compatible with the Schramm-Loewner evolution (SLE) with  $\kappa = 6$ , for more than two decades in range and this was confirmed using two independent methods (Fig. 3 and Table 1). Remarkably,

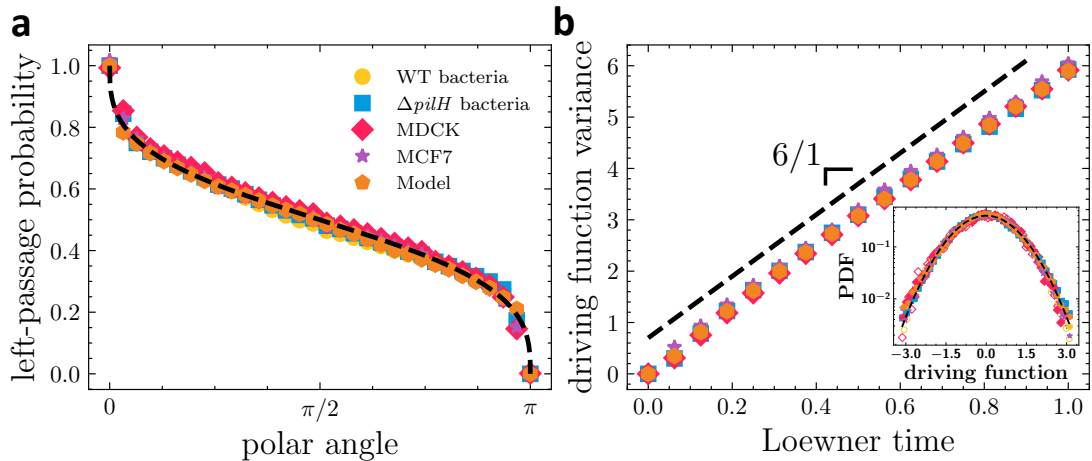


Figure 3: **Resolving the underlying universality class of vorticity contours using two independent methods.** (a) The left-passage probability is defined as the probability that a point in space is on the right-hand side of the contour for a given polar angle. Data from all four cellular genotypes and the results from the numerical model are in close agreement with Schramm's formula for  $\kappa = 6$  (dashed black line, [34]). (b) Time-dependence of the variance of driving function obtained from a unique conformal slit map [33]. The dashed black line shows the result for one-dimensional Brownian motion with  $\kappa = 6$ . (b, inset) Probability distribution of the driving function, rescaled by  $\kappa t$ , where  $t$  is the Loewner time. Here the data at two different times  $t = 0.25$  and  $t = 0.75$  is shown, which collapses onto the same curve. For further details see *Materials and Methods*.

this finding demonstrates that, although the collective cellular motility spontaneously generates patterns of flow with lengthscales much larger than that of individual cells (Fig. 1) [38, 3], the associated vorticity contours are local and fall into the same universality class as those from random percolation [30]. Moreover, the collective cellular motion we studied here is driven far from equilibrium by the motility of individual cells that continuously inject energy into the system at small scales. The observation of conformal invariance in collective cellular flows that are continuously driven far from thermodynamic equilibrium presents both challenges and new opportunities for the development of non-equilibrium conformal field theories [40].

|                           |                          | continuum model |                   | experimental data |                 |                  |                 |                     | percolation universality class |
|---------------------------|--------------------------|-----------------|-------------------|-------------------|-----------------|------------------|-----------------|---------------------|--------------------------------|
|                           |                          |                 |                   | bacterial cells   |                 | eukaryotic cells |                 |                     |                                |
|                           |                          |                 |                   | WT                | $\Delta pilH$   | MDCK             | MCF7            |                     |                                |
| scale invariance          | fractal dimension        | $D$             | $1.75 \pm 0.01$   | $1.72 \pm 0.02$   | $1.72 \pm 0.04$ | $1.74 \pm 0.02$  | $1.74 \pm 0.03$ | $7/4 = 1.75$        |                                |
| conformal invariance      | winding angle            | $\alpha$        | $0.853 \pm 0.005$ | $0.86 \pm 0.01$   | $0.87 \pm 0.01$ | $0.85 \pm 0.01$  | $0.87 \pm 0.02$ | $6/7 \approx 0.857$ |                                |
| Schramm-Loewner Evolution | left-passage probability | $\kappa$        | $6.02 \pm 0.02$   | $5.97 \pm 0.05$   | $5.96 \pm 0.05$ | $5.95 \pm 0.03$  | $5.95 \pm 0.06$ | 6                   |                                |
|                           | driving function         | $\kappa$        | $5.96 \pm 0.05$   | $6.03 \pm 0.06$   | $5.96 \pm 0.06$ | $5.98 \pm 0.04$  | $5.93 \pm 0.04$ | 6                   |                                |

Table 1: **Measurements of the fractal dimension, winding angle, left-passage probability, and driving function of the four different cellular genotypes and numerical simulations.** The values are calculated from the velocity fields obtained from single cell tracking (*Materials and Methods*) and the errors represent standard deviation about the mean.

These results suggest that the theories used to describe conformally invariant structures

might have a much broader range of applications than previously anticipated. While collective movement is observed in diverse biological systems, that observed in microscopic cellular systems is particularly amenable to experimental analysis because in-situ cell division rapidly gives rise to large genetically identical populations, two-dimensional movement of monolayers of cells can be readily imaged, and the environmental conditions can be carefully controlled. Similar to the collective cellular motility studied here, many different kinds of living systems are formed of strongly interacting components driven far from thermal equilibrium and exhibit complex vortical patterns, including subcellular flows [41] [42], synthetic active material [43] [1] [44], animal swarms [45] [46], and *in-vitro* reconstitutions of cytoskeletal transport systems [47] [48] [49]. In addition, emergent vortical structures also shape many important processes in biology including cell differentiation [16], cartilage regeneration [50], embryogenesis [51], signaling waves that propagate along cell membranes [52] and between cells [53], as well as vortical waves associated with cardiac arrhythmia [54] and spiral-like patterns of brain activity linked to cognitive processing [55]. We speculate that such biological processes might not only serve as novel test bed to validate predictions based on conformal symmetry, but this robust symmetry might also lead to the development of new analytical techniques to identify the fundamental mechanisms that give rise to both function and dysfunction in complex biological systems.

## References

- [1] C. Bechinger, R. Di Leonardo, H. Löwen, C. Reichhardt, G. Volpe, and G. Volpe, “Active Particles in Complex and Crowded Environments,” Reviews of Modern Physics, vol. 88, p. 045006, Nov. 2016.
- [2] F. Jülicher, S. W. Grill, and G. Salbreux, “Hydrodynamic theory of active matter,” Reports on Progress in Physics, vol. 81, p. 076601, June 2018.
- [3] P. Friedl and D. Gilmour, “Collective cell migration in morphogenesis, regeneration and cancer,” Nature reviews Molecular cell biology, vol. 10, no. 7, pp. 445–457, 2009.
- [4] R. Zhang, A. Mozaffari, and J. J. de Pablo, “Autonomous materials systems from active liquid crystals,” Nature Reviews Materials, vol. 6, no. 5, pp. 437–453, 2021.
- [5] M. C. Marchetti, J. F. Joanny, S. Ramaswamy, T. B. Liverpool, J. Prost, M. Rao, and R. A. Simha, “Hydrodynamics of soft active matter,” Reviews of Modern Physics, vol. 85, no. 3, pp. 1143–1189, 2013.
- [6] N. Wadhwa and H. C. Berg, “Bacterial motility: machinery and mechanisms,” Nature reviews microbiology, vol. 20, no. 3, pp. 161–173, 2022.
- [7] X. Trepast and E. Sahai, “Mesoscale physical principles of collective cell organization,” Nature Physics, vol. 14, no. 7, pp. 671–682, 2018.
- [8] P. C. Hohenberg and B. I. Halperin, “Theory of dynamic critical phenomena,” Reviews of Modern Physics, vol. 49, pp. 435–479, July 1977.

- [9] A. A. Belavin, A. M. Polyakov, and A. B. Zamolodchikov, “Infinite conformal symmetry in two-dimensional quantum field theory,” Nuclear Physics B, vol. 241, no. 2, pp. 333–380, 1984.
- [10] J. L. Cardy, “Conformal invariance and universality in finite-size scaling,” Journal of Physics A: Mathematical and General, vol. 17, no. 7, p. L385, 1984.
- [11] D. Bernard, G. Boffetta, A. Celani, and G. Falkovich, “Conformal invariance in two-dimensional turbulence,” Nature Physics, vol. 2, pp. 124–128, 2006.
- [12] D. Bernard, G. Boffetta, A. Celani, and G. Falkovich, “Inverse turbulent cascades and conformally invariant curves,” Physical review letters, vol. 98, no. 2, p. 024501, 2007.
- [13] L. Puggioni, A. G. Kritsuk, S. Musacchio, and G. Boffetta, “Conformal invariance of weakly compressible two-dimensional turbulence,” Physical Review E, vol. 102, no. 2, p. 023107, 2020.
- [14] N. Javerzat and M. Bouzid, “Evidences of conformal invariance in 2d rigidity percolation,” Physical Review Letters, vol. 130, no. 26, p. 268201, 2023.
- [15] N. Javerzat, “Schramm-loewner evolution in 2d rigidity percolation,” Physical Review Letters, vol. 132, no. 1, p. 018201, 2024.
- [16] P. Guillamat, C. Blanch-Mercader, G. Pernollet, K. Kruse, and A. Roux, “Integer topological defects organize stresses driving tissue morphogenesis,” Nature materials, vol. 21, no. 5, pp. 588–597, 2022.
- [17] M. Prasad, C. Blanch-Mercader, J. Prost, J.-F. Rupprecht, and A. S. Utada, “*Alcanivorax borkumensis* biofilms enhance oil degradation by interfacial tubulation,” Science, pp. 748–753, 2023.
- [18] O. J. Meacock, A. Doostmohammadi, K. R. Foster, J. M. Yeomans, and W. M. Durham, “Bacteria solve the problem of crowding by moving slowly,” Nature Physics, vol. 17, pp. 205–210, Feb. 2021.
- [19] N. M. Oliveira, K. R. Foster, and W. M. Durham, “Single-cell twitching chemotaxis in developing biofilms,” Proceedings of the National Academy of Sciences, vol. 113, no. 23, pp. 6532–6537, 2016.
- [20] J. J. Bertrand, J. T. West, and J. N. Engel, “Genetic analysis of the regulation of type iv pilus function by the chp chemosensory system of *pseudomonas aeruginosa*,” Journal of bacteriology, vol. 192, no. 4, pp. 994–1010, 2010.
- [21] T. B. Saw, A. Doostmohammadi, V. Nier, L. Kocgozlu, S. Thampi, Y. Toyama, P. Marcq, C. T. Lim, J. M. Yeomans, and B. Ladoux, “Topological defects in epithelia govern cell death and extrusion,” Nature, vol. 544, no. 7649, pp. 212–216, 2017.



- [22] L. Balasubramaniam, A. Doostmohammadi, T. B. Saw, G. H. N. S. Narayana, R. Mueller, T. Dang, M. Thomas, S. Gupta, S. Sonam, A. S. Yap, Y. Toyama, R.-M. Mège, J. M. Yeomans, and B. Ladoux, “Investigating the nature of active forces in tissues reveals how contractile cells can form extensile monolayers,” Nature Materials, vol. 20, p. 1156–1166, Feb. 2021.
- [23] L. M. Pismen, Vortices in nonlinear fields: from liquid crystals to superfluids, from non-equilibrium patterns to cosmic strings, vol. 100. Oxford University Press, 1999.
- [24] B. Duplantier, “Conformally invariant fractals and potential theory,” Physical Review Letters, vol. 84, no. 7, p. 1363, 2000.
- [25] B. Duplantier, “Higher conformal multifractality,” Journal of statistical physics, vol. 110, pp. 691–738, 2003.
- [26] B. Duplantier and H. Saleur, “Winding-angle distributions of two-dimensional self-avoiding walks from conformal invariance,” Physical review letters, vol. 60, no. 23, p. 2343, 1988.
- [27] O. Schramm, “Scaling limits of loop-erased random walks and uniform spanning trees,” Israel Journal of Mathematics, vol. 118, p. 221–288, 2000.
- [28] J. Cardy, “Sle for theoretical physicists,” Annals of Physics, vol. 318, no. 1, pp. 81–118, 2005.
- [29] T. Kennedy, “Monte carlo tests of stochastic loewner evolution predictions for the 2d self-avoiding walk,” Physical Review Letters, vol. 88, mar 2002.
- [30] S. Smirnov, “Critical percolation in the plane: conformal invariance, cardy’s formula, scaling limits,” Comptes Rendus de l’Académie des Sciences - Series I - Mathematics, vol. 333, pp. 239–244, 2001.
- [31] D. Bernard, P. Le Doussal, and A. A. Middleton, “Possible description of domain walls in two-dimensional spin glasses by stochastic loewner evolutions,” Phys. Rev. B, vol. 76, p. 020403, 2007.
- [32] E. Daryaei, N. A. M. Araújo, K. J. Schrenk, S. Rouhani, and H. J. Herrmann, “Watersheds are schramm-loewner evolution curves,” Physical Review Letters, vol. 109, no. 21, p. 218701, 2012.
- [33] T. Kennedy, “Numerical computations for the schramm-loewner evolution,” Journal of Statistical Physics, vol. 137, pp. 839–856, 2009.
- [34] O. Schramm, “A percolation formula,” Electronic Communications in Probability, vol. 6, pp. 115 – 120, 2001.
- [35] V. Beffara, “The dimension of the SLE curves,” The Annals of Probability, vol. 36, pp. 1421 – 1452, 2008.

- [36] G. F. Lawler, O. Schramm, and W. Werner, “Values of brownian intersection exponents, ii: Plane exponents,” in Selected Works of Oded Schramm, pp. 897–930, Springer, 2011.
- [37] M. R. Shaebani, A. Wysocki, R. G. Winkler, G. Gompper, and H. Rieger, “Computational models for active matter,” Nature Reviews Physics, vol. 2, pp. 181–199, Apr. 2020.
- [38] H. H. Wensink, J. Dunkel, K. Drescher, R. E. Goldstein, H. Löwen, and J. M. Yeomans, “Meso-scale turbulence in living fluids,” Proceedings of the National Academy of Sciences, vol. 109, no. 36, pp. 14308–14313, 2012.
- [39] B. Ladoux and R.-M. Mège, “Mechanobiology of collective cell behaviours,” Nature Reviews Molecular Cell Biology, vol. 18, pp. 743–757, Dec. 2017. Number: 12 Publisher: Nature Publishing Group.
- [40] D. Bernard and B. Doyon, “Conformal field theory out of equilibrium: a review,” Journal of Statistical Mechanics: Theory and Experiment, vol. 2016, no. 6, p. 064005, 2016.
- [41] R. E. Goldstein and J.-W. van de Meent, “A physical perspective on cytoplasmic streaming,” Interface focus, vol. 5, no. 4, p. 20150030, 2015.
- [42] D. B. Stein, G. De Canio, E. Lauga, M. J. Shelley, and R. E. Goldstein, “Swirling instability of the microtubule cytoskeleton,” Physical review letters, vol. 126, no. 2, p. 028103, 2021.
- [43] J. Palacci, S. Sacanna, A. P. Steinberg, D. J. Pine, and P. M. Chaikin, “Living crystals of light-activated colloidal surfers,” Science, vol. 339, no. 6122, pp. 936–940, 2013.
- [44] K. Han, G. Kokot, A. Glatz, I. S. Aranson, and A. Snezhko, “Emergence of self-organized multivortex states in flocks of active rollers,” Proceedings of the National Academy of Sciences, vol. 117, no. 18, pp. 9706–9711, 2020.
- [45] A. Cavagna and I. Giardina, “Bird Flocks as Condensed Matter,” Annual Review of Condensed Matter Physics, vol. 5, pp. 183–207, Mar. 2014.
- [46] J. Delcourt, N. W. Bode, and M. Denoël, “Collective vortex behaviors: Diversity, proximate, and ultimate causes of circular animal group movements,” The Quarterly review of biology, vol. 91, no. 1, pp. 1–24, 2016.
- [47] V. Schaller, C. Weber, C. Semmrich, E. Frey, and A. R. Bausch, “Polar patterns of driven filaments,” Nature, vol. 467, no. 7311, pp. 73–77, 2010.
- [48] T. Sanchez, D. T. N. Chen, S. J. DeCamp, M. Heymann, and Z. Dogic, “Spontaneous motion in hierarchically assembled active matter,” Nature, vol. 491, pp. 431–434, Nov. 2012.
- [49] Y. Sumino, K. H. Nagai, D. Tanaka, H. Chaté, and K. Oiwa, “Large-scale vortex lattice emerging from collectively moving microtubules,” Nature, vol. 483, no. 7390, pp. 448–452, 2012.

- [50] E. Makhija, Y. Zheng, J. Wang, H. R. Leong, R. B. Othman, E. X. Ng, E. H. Lee, L. Tucker Kellogg, Y. H. Lee, H. Yu, et al., “Topological defects govern mesenchymal condensations, offering a morphology-based tool to predict cartilage differentiation,” *bioRxiv*, p. 2022.05.30.493944, 2022.
- [51] D. J. Smith, T. D. Montenegro-Johnson, and S. S. Lopes, “Symmetry-breaking cilia-driven flow in embryogenesis,” *Annual Review of Fluid Mechanics*, vol. 51, no. 1, pp. 105–128, 2019.
- [52] T. H. Tan, J. Liu, M. Tekant, J. Dunkel, and N. Fakhri, “Topological turbulence in the membrane of a living cell,” *Nature Physics*, vol. 16, no. 6, pp. 657–662, 2020.
- [53] A. J. Mathijssen, J. Culver, M. S. Bhamla, and M. Prakash, “Collective intercellular communication through ultra-fast hydrodynamic trigger waves,” *Nature*, vol. 571, no. 7766, pp. 560–564, 2019.
- [54] J. Christoph, M. Chebbok, C. Richter, J. Schröder-Schetelig, P. Bittihn, S. Stein, I. Uzelac, F. H. Fenton, G. Hasenfuß, R. Gilmour Jr, et al., “Electromechanical vortex filaments during cardiac fibrillation,” *Nature*, vol. 555, no. 7698, pp. 667–672, 2018.
- [55] Y. Xu, X. Long, J. Feng, and P. Gong, “Interacting spiral wave patterns underlie complex brain dynamics and are related to cognitive processing,” *Nature Human Behaviour*, pp. 1–20, 2023.

## Acknowledgments

We thank Guido Boffetta for comments on a previous version of this manuscript and Ramin Golestanian for helpful discussions.

## Funding

This work was supported by the Novo Nordisk Foundation (grant no. NNF18SA0035142 and NERD grant no. NNF21OC0068687) (to AD), Villum Fonden Grant no. 29476 (to AD), the European Union via the ERC-Starting Grant PhysCoMeT, grant no. 101041418 (to AD), the Portuguese Foundation for Science and Technology (FCT) under Contracts no. EXPL/FIS-MAC/0406/2021, UIDB/00618/2020, and UIDP/00618/2020 (to NA), a Biotechnology and Biological Sciences Research Council (BBSRC) New Investigator grant (grant no. BB/R018383/1) (to WMD), and a Human Frontier Science Program grant (grant no. RGY0080/2021) (to WMD).

## Authors contributions

A.D. and N.A.M.A. designed the project. B.H.A. and F.S. performed analyses of scale and conformal invariance as well as SLE measurements on the experimental data. B.H.A. implemented the model, analysed data and prepared figures. V.G. performed the experiments and conducted

particle image velocimetry measurements on MDCK and MCF-7 cells. S.G.A. performed single cell tracking analyses for MDCK and MCF-7 monolayers. O.J.M. performed the experiments on bacterial cells and conducted particle image velocimetry and single cell tracking analyses on bacterial monolayers. W.M.D., N.A.M.A. and A.D. all contributed to the design of experiments and models, as well as to the interpretation of results. A.D. prepared the first draft. A.D. and W.M.D. wrote the paper with input from N.A.M.A. This collaborative effort was led by A.D.

# Appendices



# Appendix A

## The Dirac $\delta$ -distribution of a composite argument

Let  $T : \Omega \subseteq \mathbb{R}^n \rightarrow \mathbb{R}^n$  be a sufficiently well behaved function with a countable number zeros  $\{\mathbf{x}_k\}$ . Its composition with the Dirac  $\delta$ -distribution results in a new *Schwartz distribution*, specifically

$$(\delta \circ T)(\mathbf{x}) = \frac{1}{|D(\mathbf{x})|} \sum_k \delta(\mathbf{x} - \mathbf{x}_k), \quad (\text{A.1})$$

where  $D = \det(\nabla T)$  is the familiar *Jacobian* of  $T$ .

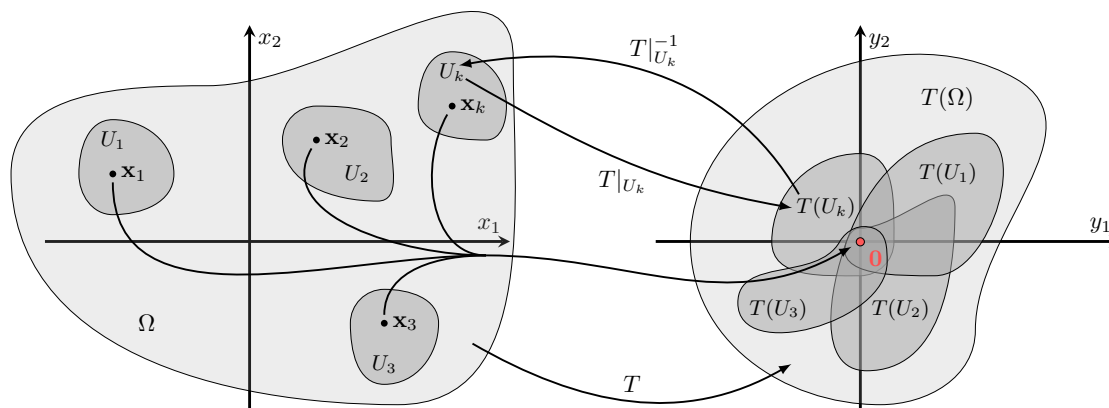


Figure A.1: Schematic illustration of the “*well-behaved*” nature and characteristics of the function  $T : \Omega \subseteq \mathbb{R}^n \rightarrow \mathbb{R}^n$ , which possesses a countable number zeros  $\{\mathbf{x}_k\}$ .

## A.1 A heuristic *and not fully rigorous* derivation

The support of the Dirac  $\delta$ -distribution consist of the single point  $\mathbf{0}$ , implying that

$$\text{supp}(\delta \circ T) = \{\mathbf{x}_1, \mathbf{x}_2, \mathbf{x}_3, \dots, \mathbf{x}_k, \dots\}. \quad (\text{A.2})$$

Consequently,  $T$  only needs to be well-behaved in the vicinity of its zeros. Therefore let  $U_k \subseteq \Omega$  be a neighbourhood of the zero  $\mathbf{x}_k$  such that the bijective restriction  $T|_{U_k} : U_k \rightarrow \mathbb{R}^n$  defines a diffeomorphism. Now, let  $\varphi : \Omega \rightarrow \mathbb{R}^n$  be some sufficiently smooth test function and consider

$$\langle \delta \circ T, \varphi \rangle \doteq \int_{\Omega} (\delta \circ T)(\mathbf{x}) \varphi(\mathbf{x}) d^n \mathbf{x} \quad (\text{A.3})$$

$$= \sum_k \int_{U_k} (\delta \circ T)(\mathbf{x}) \varphi(\mathbf{x}) d^n \mathbf{x} \quad (\text{A.4})$$

$$= \sum_k \int_{U_k} (\delta \circ T|_{U_k})(\mathbf{x}) \varphi(\mathbf{x}) d^n \mathbf{x}. \quad (\text{A.5})$$

The diffeomorphism  $T|_{U_k}$  defines a transformation  $\mathbf{x} \mapsto \mathbf{y} = T|_{U_k}(\mathbf{x})$  with an associated Jacobian  $J : U_k \rightarrow \mathbb{R}$ . According to *the inverse function theorem*, this Jacobian is given by the reciprocal of  $(D \circ T|_{U_k}^{-1})$ , hence

$$= \sum_k \int_{T(U_k)} \delta(\mathbf{y}) (\varphi \circ T|_{U_k}^{-1})(\mathbf{y}) \frac{d^n \mathbf{y}}{|(D \circ T|_{U_k}^{-1})(\mathbf{y})|} \quad (\text{A.6})$$

$$= \sum_k \frac{(\varphi \circ T|_{U_k}^{-1})(\mathbf{0})}{|(D \circ T|_{U_k}^{-1})(\mathbf{0})|} \quad (\text{A.7})$$

$$= \sum_k \frac{\varphi(\mathbf{x}_k)}{|D(\mathbf{x}_k)|} \quad (\text{A.8})$$

and using the *sifting* property of the  $\delta$ -distribution

$$= \sum_k \int_{U_k} \frac{\delta(\mathbf{x} - \mathbf{x}_k)}{|D(\mathbf{x})|} \varphi(\mathbf{x}) d^n \mathbf{x} \quad (\text{A.9})$$

and from the linearity of Schwartz distributions

$$= \int_{\Omega} \sum_k \frac{\delta(\mathbf{x} - \mathbf{x}_k)}{|D(\mathbf{x})|} \varphi(\mathbf{x}) d^n \mathbf{x} \quad (\text{A.10})$$

$$= \left\langle \sum_k \frac{\delta(\mathbf{x} - \mathbf{x}_k)}{|D(\mathbf{x})|}, \varphi \right\rangle. \quad (\text{A.11})$$

Thereby concluding that (A.1) or equivalently that

$$(\delta \circ T)(\mathbf{x}) = \sum_k \frac{\delta(\mathbf{x} - \mathbf{x}_k)}{|D(\mathbf{x}_k)|}. \quad (\text{A.12})$$



## A.2 The continuity equation for the Jacobian

It is instructive to consider the aforementioned function  $T$  as an  $n$ -component order parameter and its countable set of zeros  $\{\mathbf{x}_k\}$  as defect positions. In this context, equation (A.1) represents a change of variables from the defect positions  $\{\mathbf{x}_k\}$  to the order parameter  $T$ . By definition, the Jacobian determinant of this change of variables can be expressed as

$$D = \frac{1}{n!} \epsilon^{i_1 i_2 \dots i_n} \epsilon_{j_1 j_2 \dots j_n} \partial_{i_1} T^{j_1} \partial_{i_2} T^{j_2} \dots \partial_{i_n} T^{j_n}, \quad (\text{A.13})$$

where  $\epsilon^{i_1 i_2 \dots i_n}$  is the usual  $n$ -dimensional permutation symbol. Interestingly, the Jacobian has to obey the continuity equation:

$$\partial_t D = \partial_i J^i, \quad (\text{A.14})$$

where the current density

$$J^k = \frac{1}{(n-1)!} \epsilon^{k i_2 \dots i_n} \epsilon_{j_1 j_2 \dots j_n} \partial_t T^{j_1} \partial_{i_2} T^{j_2} \dots \partial_{i_n} T^{j_n} \quad (\text{A.15})$$

is determined by a yet-to-be-specified governing equation for  $T$ , such as a time-dependent Ginzburg-Landau model.

*Proof.* For simplicity, let  $T$  be a two-component order parameter with Jacobian

$$D = \frac{1}{2} \epsilon^{ij} \epsilon_{mn} \partial_i T^m \partial_j T^n. \quad (\text{A.16})$$

Now, take the temporal derivative:

$$\partial_t D = \frac{1}{2} \epsilon^{ij} \epsilon_{mn} (\partial_t \partial_i T^m \partial_j T^n + \partial_i T^m \partial_t \partial_j T^n) \quad (\text{A.17})$$

$$= \frac{1}{2} (\epsilon^{ij} \epsilon_{mn} \partial_t \partial_i T^m \partial_j T^n + \epsilon^{ji} \epsilon_{nm} \partial_j T^n \partial_t \partial_i T^m) \quad (\text{A.18})$$

$$= \epsilon^{ij} \epsilon_{mn} \partial_t \partial_i T^m \partial_j T^n \quad (\text{A.19})$$

and when applying the Leibniz product rule

$$= \epsilon^{ij} \epsilon_{mn} \{ \partial_i (\partial_t T^m \partial_j T^n) - \partial_t T^m \partial_{ij} T^n \}, \quad (\text{A.20})$$

where the last term vanishes because  $\epsilon^{ij}$  is skew-symmetric while  $\partial_{ij}$  is symmetric, assuming  $T$  is at least  $C^2$ .  $\square$